A TARGETED LIGO-VIRGO SEARCH FOR GRAVITATIONAL WAVES

ASSOCIATED WITH GAMMA-RAY BURSTS USING LOW-THRESHOLD

SWIFT GRB TRIGGERS

by

EMELIE D. HARSTAD

A DISSERTATION

Presented to the Department of Physics
and the Graduate School of the University of Oregon
in partial fulfillment of the requirements
for the degree of
Doctor of Philosophy

March 2013

DISSERTATION APPROVAL PAGE

Student: Emelie D. Harstad

Title: A Targeted LIGO-Virgo Search for Gravitational Waves Associated with Gamma-Ray Bursts Using Low-Threshold Swift GRB Triggers

This dissertation has been accepted and approved in partial fulfillment of the requirements for the Doctor of Philosophy degree in the Department of Physics by:

Dr. James Brau	Chair
Dr. Raymond Frey	Advisor
Dr. Graham Kribs	Member
Dr. Michael Raymer	Member
Dr. James Isenberg	Outside Member

and

Kimberly Andrews Espy	Vice President for Research & Innovation/ Dean of the Graduate School

Original approval signatures are on file with the University of Oregon Graduate School.

Degree awarded March 2013

DISSERTATION ABSTRACT

Emelie D. Harstad

Doctor of Philosophy

Department of Physics

March 2013

Title: A Targeted LIGO-Virgo Search for Gravitational Waves Associated with Gamma-Ray Bursts Using Low-Threshold Swift GRB Triggers

Gamma-ray bursts (GRBs) are short, intense flashes of 0.1-1 MeV electromagnetic radiation that are routinely observed by Earth orbiting satellites. The sources of GRBs are known to be extragalactic and located at cosmological distances. Due to the extremely high isotropic equivalent energies of GRBs, which are on the order of $E_{iso}{\sim}10^{54}$ erg, the γ-ray emission is believed to be collimated, making them observable only when they are directed towards Earth. The favored progenitor models of GRBs are also believed to emit gravitational waves that would be observable by the current generation of ground-based interferometric gravitational wave detectors. The LIGO (Laser Interferometer Gravitational-Wave Observatory) and Virgo instruments operated near design sensitivity and collected more than a year of triple coincident data during the S5/VSR1 science run, which spanned the two year interval between November 2005 and October 2007. During this time, GRB detections were being made by the NASA/Goddard Swift Burst Alert Telescope at a rate of approximately 0.3 per day, producing a collection of triggers that has since been used in a coincident GRB-GW burst search with data from the LIGO-Virgo interferometer network. This dissertation describes the search for gravitational waves using the times and locations of 123 *below*-threshold potential GRB triggers from Swift over the same time period.

Although most of the below-threshold triggers are likely false alarms, there is reason to believe that some are the result of actual faintly-observed GRB events. Recent GRB observations indicate that the local rate of low-luminosity GRBs is much higher than previously believed. This result, combined with the possibility of discovering a rare nearby GRB event accompanied by gravitational waves, is what motivates this search. The analysis results indicate no evidence for gravitational waves associated with any of the below-threshold triggers. A median distance lower limit of ~16 Mpc was derived for a typical neutron star-black hole coalescence progenitor assumption.

CURRICULUM VITAE

NAME OF AUTHOR: Emelie D. Harstad

GRADUATE AND UNDERGRADUATE SCHOOLS ATTENDED:
    University of Oregon, Eugene, Oregon
    University of Colorado, Boulder, Colorado
    Whitman College, Walla Walla, Washington

DEGREES AWARDED:
    Doctor of Philosophy in Physics, 2013, University of Oregon
    Master of Science in Aerospace Engineering Sciences, 2002, University of
        Colorado, Boulder
    Bachelor of Arts in Physics and Mathematics, 2001, Whitman College

AREAS OF SPECIAL INTEREST:
    Gravitational Waves, General Relativity, Gamma-Ray Bursts

PROFESSIONAL EXPERIENCE:

    Graduate Research Assistant, University of Oregon, 2004 - 2013

    Graduate Teaching Fellow, University of Oregon, 2003 - 2004

    Graduate Teaching Fellow, University of Colorado, Boulder, 2001-2002

GRANTS, AWARDS AND HONORS:

    Outstanding Summer Research Presentation Award, University of Oregon
        Department of Physics, 2003

    Graduate School Fellowship Award, University of Colorado, Boulder, 2001

    Phi Beta Kappa Society Membership, 2001

ACKNOWLEDGEMENTS

There are many people who helped make this work possible. I would first like to thank Jim Brau and my thesis advisor Ray Frey for their continued support throughout the years. I am also grateful to the other UO-LIGO group members who helped me up the steep learning curve and provided much-needed guidance when I first joined the group: Masahiro Ito, Robert Schofield, Rauha Rahkola, and Isabel Leonor. Thanks also to Jay Cummings, Hans Krimm, and David Palmer for all of their advice in decoding the Swift BAT data, and to Michal Was for his help running X-Pipeline and for answering all of my emails!

To my friends Debbie, Libby, and Elsa who never gave up on me, thank you for putting up with me, being weird with me, keeping me out of trouble, getting me into trouble, and letting me know that I'm not alone. And to my family - Mom, Dad, and Leslie - I love you and would not be where I am today without your support, encouragement, and unconditional love. Finally, to my Matthias, thank you from the bottom of my heart for holding me together and not just believing in me, but doing the impossible and making me believe in myself.

for Grandmother

TABLE OF CONTENTS

LIST OF FIGURES

LIST OF TABLES

CHAPTER I

INTRODUCTION

Albert Einstein proposed the Theory of General Relativity (GR) nearly 100 years ago [1]. It is a theory in which the force we commonly know as gravity is actually the manifestation of the curvature of spacetime. This curvature is both a cause and effect of the distribution and energetics of mass in space. And, as with any good physical theory, it is a scientist's job to test it.

Newton's theory of gravity is only a non-relativistic approximation to GR and is easily testable, as we all experience it in our daily lives. However, testing the effects of GR (or rather the difference between the two theories) is extremely difficult and requires nearby stellar-size masses moving at close to relativistic speeds. This is due to the fact that spacetime is a very stiff 'material', requiring a huge amount of energy to bend it.

One way physicists hope to verify GR is through the detection of gravitational waves (GWs), which are a consequence of Einstein's theory. In GR, the force of gravity is not carried across space from one mass to another instantly, but travels at the speed of light. And if that change in force is in the form of an oscillation (caused by a large second time derivative of the mass quadrupole moment), the propagation of the changing spacetime curvature can be thought of as a wave, which manifests itself as length changes perpendicular to the direction of propagation. Measuring such length changes, would provide direct evidence for the validity of GR.

Some of the astrophysical systems capable of producing length changes detectable on Earth are discussed in Section 2.3 (a classic example is two neutron stars or black holes locked in circular orbit around one another just before their final coalescence).

However, even with a large km-length detector, the most promising sources of GWs would require the ability to measure length changes on the order of 10^{-16} cm [2]. Amazingly, current interferometric gravitational wave detectors have already achieved this sensitivity (see Chapter III). But detecting a gravitational wave also requires the chance occurrence of a rare nearby event, and at the writing of this thesis, no direct detection has yet been confirmed.

Even though gravitational waves have not been detected, evidence for GR does exist in several well-studied phenomena which include gravitational redshift, gravitation lensing, GR's accurate prediction of the perihelion precession of the planet Mercury, and the rate of energy lost by a binary pulsar system. In this last example, two bodies (pulsars) orbit one another radiating energy in the form of gravitation waves. Energy conservation requires the orbital energy to decrease at the same rate, shrinking the radius of the orbit, and increasing the orbital period. In 1979, Taylor et al. observed the increasing orbital period of pulsar binary PSR1913+16 (commonly known as the Hulse-Taylor pulsar), and showed that the rate of energy loss agrees to high precision with predictions based on general relativity [3].

One of the objectives of this work is to attempt to verify general relativity by the detection of gravitational waves. The other is to contribute to the body of knowledge concerning Gamma-Ray Bursts (GRBs), which are discussed more in Chapter II. To this end, data from the network of LIGO and Virgo gravitational wave detectors is analyzed at the time and location of possible GRB 'triggers' provided by the Swift satellite. Since the trigger provides information about where and when the GW could have originated, it effectively increases the sensitivity of the search, and lends additional validity to any resulting GW detections.

This thesis is organized as follows: Chapter I provides a theoretical introduction to General Relativity, and the production of gravitational waves, Chapter II gives an introduction to GRBs and their progenitors, GRB detection, gravitation waveforms from GRBs, and the motivation for a triggered search using low-threshold GRB detections. Chapter III describes the LIGO and Virgo detectors, antenna patterns, detector sensitivity, and noise sources. Chapter IV, the methods chapter, is divided into three main parts. The first part provides an overview of Swift and the Burst Alert Telescope. The next section describes the trigger selection process, and the estimation of the trigger false alarm rate. And the last section gives an introduction and step-by-step walkthrough of X-Pipeline, the analysis code used in this search. Finally, Chapter V presents the results of the search, and a brief summary and discussion is provided in Chapter VI.

1.1. General Relativity and Gravitational Waves

The next three sections outline the derivation of the production and effects of gravitational waves in linearized General Relativity, and follow the derivations given in [2] and [4].

In General Relativity, the curvature of spacetime is described by the metric tensor $g_{\mu\nu}$. That is, the distance element is given by

$$\mathrm{d}s^2(x) = g_{\mu\nu}(x)\mathrm{d}x^\mu \mathrm{d}x^\nu, \tag{1.1}$$

where $\mathrm{d}x^\mu$ is the infinitesimal change along the dimension x_μ. To find $g_{\mu\nu}$ and determine the motion of objects in a the presence of the symmetric stress-energy

3

tensor $T_{\mu\nu}$, one must solve the Einstein equation:

$$G_{\mu\nu} = R_{\mu\nu} - \frac{1}{2}g_{\mu\nu}R = \frac{8\pi G}{c^4}T_{\mu\nu}, \qquad (1.2)$$

where $G_{\mu\nu}$ is known as the *Einstein tensor*, G is the gravitational constant, and c is the speed of light in vacuum. $T_{\mu\nu}$ describes the distribution and evolution of energy and momentum density in spacetime. The T_{00} and T_{i0} components correspond to *mass density* and *momentum density*, respectively, while T_{ii} and T_{ij} correspond to *pressure* and *shear stress*. $T_{\mu\nu} = 0$ in vacuum. Eq. 1.2 is actually a non-linear second order differential equation for $g_{\mu\nu}$, which is written quite compactly here by making use of the *Ricci tensor* $R_{\mu\nu}$, and the *Ricci scalar* $R \equiv g^{\mu\nu}R_{\mu\nu}$ (where we sum over similar upper and lower indices). The Ricci tensor is defined as

$$R_{\mu\nu} \equiv R^{\alpha}_{\mu\alpha\nu}. \qquad (1.3)$$

The right-hand side of Eq. 1.3 is a summation of terms in the *Riemann tensor*, which is given by

$$R^{\rho}_{\mu\sigma\nu} \equiv \partial_{\sigma}\Gamma^{\rho}_{\mu\nu} - \partial_{\nu}\Gamma^{\rho}_{\mu\sigma} + \Gamma^{\rho}_{\alpha\sigma}\Gamma^{\alpha}_{\mu\nu} - \Gamma^{\rho}_{\alpha\nu}\Gamma^{\alpha}_{\mu\sigma}. \qquad (1.4)$$

Here, we have also made use of the so-called *Christoffel symbols* which are defined as

$$\Gamma^{\rho}_{\mu\nu} \equiv \frac{1}{2}g^{\rho\sigma}(\partial_{\mu}g_{\sigma\nu} + \partial_{\nu}g_{\sigma\mu} - \partial_{\sigma}g_{\mu\nu}). \qquad (1.5)$$

The problem of solving Eq. 1.2 can be simplified by recognizing that we are interested in solutions far from the source, where $T_{\mu\nu} = 0$. The equation can also be *linearlized* by assuming that the solutions are given by small perturbations on the

4

flat spacetime metric. That is,

$$g_{\mu\nu} = \eta_{\mu\nu} + h_{\mu\nu}, \tag{1.6}$$

where $|h_{\mu\nu}| \ll 1$, and $\eta_{\mu\nu}$ is the *Minkowski flat spacetime metric*:

$$\eta_{\mu\nu} = \begin{pmatrix} -1 & 0 & 0 & 0 \\ 0 & 1 & 0 & 0 \\ 0 & 0 & 1 & 0 \\ 0 & 0 & 0 & 1 \end{pmatrix}. \tag{1.7}$$

Then the inverse of Eq. 1.6 must satisfy the metric condition $g^{\mu\nu} g_{\nu\sigma} = \delta^\mu_\sigma$. Keeping only terms to first order in $h_{\mu\nu}$ and its derivatives gives

$$g^{\mu\nu} = \eta^{\mu\nu} - h^{\mu\nu}, \tag{1.8}$$

where the inverse of $h_{\mu\nu}$ is defined as $h^{\mu\nu} \equiv \eta^{\mu\rho} \eta^{\nu\sigma} h_{\rho\sigma}$.

Substituting Eqs. 1.6 and 1.8 into Eq. 1.5 and neglecting higher order terms in $h_{\mu\nu}$ yields the linearized Christoffel-symbols:

$$\begin{aligned} \Gamma^\rho_{\mu\nu} &= \tfrac{1}{2}(\eta^{\rho\sigma} - h^{\rho\sigma})[\partial_\mu(\eta_{\sigma\nu} + h_{\sigma\nu}) + \partial_\nu(\eta_{\sigma\mu} + h_{\sigma\mu}) - \partial_\sigma(\eta_{\mu\nu} + h_{\mu\nu})] \\ &= \tfrac{1}{2}(\eta^{\rho\sigma} - h^{\rho\sigma})[\partial_\mu h_{\sigma\nu} + \partial_\nu h_{\sigma\mu} - \partial_\sigma h_{\mu\nu}] \\ &= \tfrac{1}{2}(\partial_\mu h^\rho_\nu + \partial_\nu h^\rho_\mu - \partial^\rho h_{\mu\nu}) + \mathcal{O}(h^2). \end{aligned} \tag{1.9}$$

Substituting this into Eqs. 1.4 and 1.3 gives the first order approximation of the Ricci tensor

$$
\begin{aligned}
R_{\mu\nu} &= \tfrac{1}{2}\partial_\rho(\partial_\mu h_\nu^\rho + \partial_\nu h_\mu^\rho - \partial^\rho h_{\mu\nu}) - \tfrac{1}{2}\partial_\nu(\partial_\mu h_\rho^\rho + \partial_\rho h_\mu^\rho - \partial^\rho h_{\mu\rho}) + \mathcal{O}(h^2) \\
&= \tfrac{1}{2}[\partial_\rho\partial_\mu h_\nu^\rho + \partial_\rho\partial_\nu h_\mu^\rho - \partial_\rho\partial^\rho h_{\mu\nu} - \partial_\nu\partial_\mu h_\rho^\rho - \partial_\nu\partial_\rho h_\mu^\rho + \partial_\nu\partial^\rho h_{\mu\rho}] + \mathcal{O}(h^2) \\
&= \tfrac{1}{2}[\partial_\nu\partial^\rho h_{\mu\rho} + \partial_\mu\partial^\rho h_{\nu\rho} - \partial_\rho\partial^\rho h_{\mu\nu} - \partial_\mu\partial_\nu h] + \mathcal{O}(h^2),
\end{aligned}
$$
$$(1.10)$$

where $h \equiv h_\rho^\rho$. Then the Ricci scalar becomes

$$
\begin{aligned}
R &= g^{\mu\nu} R_{\mu\nu} \\
&= \tfrac{1}{2}(\eta^{\mu\nu} - h^{\mu\nu})(\partial_\nu\partial^\rho h_{\mu\rho} + \partial_\mu\partial^\rho h_{\nu\rho} - \partial_\rho\partial^\rho h_{\mu\nu} - \partial_\mu\partial_\nu h) + \mathcal{O}(h^2) \\
&= \tfrac{1}{2}(\eta^{\mu\nu}\partial_\nu\partial^\rho h_{\mu\rho} + \eta^{\mu\nu}\partial_\mu\partial^\rho h_{\nu\rho} - \eta^{\mu\nu}\partial_\rho\partial^\rho h_{\mu\nu} - \eta^{\mu\nu}\partial_\mu\partial_\nu h) + \mathcal{O}(h^2) \\
&= \tfrac{1}{2}(\partial^\mu\partial^\rho h_{\mu\rho} + \partial^\nu\partial^\rho h_{\nu\rho} - 2\partial_\rho\partial^\rho h) + \mathcal{O}(h^2) \\
&= \partial^\mu\partial^\rho h_{\mu\rho} - \Box h + \mathcal{O}(h^2),
\end{aligned}
$$
$$(1.11)$$

where we have implemented the d'Alembertian operator which is defined as follows:

$$
\Box \equiv \partial_\rho\partial^\rho = \frac{-\partial_t^2}{c^2} + \partial_x^2 + \partial_y^2 + \partial_z^2. \tag{1.12}
$$

We drop the higher order notation $\mathcal{O}(h^2)$ for the remainder of the derivation and assume a first order only approximation. In order to obtain the linearized form of the Einstein equation in vacuum, Eqs. 1.10 and 1.11 are substituted into Eq. 1.2 which gives

$$
\begin{aligned}
G_{\mu\nu} &= \tfrac{1}{2}(\partial_\nu\partial^\rho h_{\mu\rho} + \partial_\mu\partial^\rho h_{\nu\rho} - \Box h_{\mu\nu} - \partial_\mu\partial_\nu h) - \tfrac{1}{2}(\eta_{\mu\nu} + h_{\mu\nu})(\partial^\alpha\partial^\gamma h_{\alpha\gamma} - \Box h) \\
&= \tfrac{1}{2}(\partial_\nu\partial^\rho h_{\mu\rho} + \partial_\mu\partial^\rho h_{\nu\rho} - \Box(h_{\mu\nu} - \eta_{\mu\nu}h) - \partial_\mu\partial_\nu h - \eta_{\mu\nu}\partial^\alpha\partial^\gamma h_{\alpha\gamma}).
\end{aligned}
$$
$$(1.13)$$

The expression above can be simplified further by using the following substitution:

$$\overline{h}_{\mu\nu} \equiv h_{\mu\nu} - \frac{1}{2}\eta_{\mu\nu}h, \tag{1.14}$$

which can also be written

$$h_{\mu\nu} = \overline{h}_{\mu\nu} - \frac{1}{2}\eta_{\mu\nu}\overline{h}, \tag{1.15}$$

where we have used the property $h = -\overline{h}$. Inserting Eq. 1.15 into Eq. 1.13 yields

$$
\begin{aligned}
G_{\mu\nu} &= \tfrac{1}{2}[\partial_\nu\partial^\rho(\overline{h}_{\mu\rho} - \tfrac{1}{2}\eta_{\mu\rho}\overline{h}) + \partial_\mu\partial^\rho(\overline{h}_{\nu\rho} - \tfrac{1}{2}\eta_{\nu\rho}\overline{h}) \\
&\quad -\Box(\overline{h}_{\mu\nu} - \tfrac{1}{2}\eta_{\mu\nu}\overline{h} + \eta_{\mu\nu}\overline{h}) - \eta_{\mu\nu}\partial^\alpha\partial^\gamma(\overline{h}_{\alpha\gamma} - \tfrac{1}{2}\eta_{\alpha\gamma}\overline{h})] \\
&= \tfrac{1}{2}(\partial_\nu\partial^\rho\overline{h}_{\mu\rho} + \partial_\mu\partial^\rho\overline{h}_{\nu\rho} - \Box\overline{h}_{\mu\nu} - \eta_{\mu\nu}\partial^\alpha\partial^\gamma\overline{h}_{\alpha\gamma}).
\end{aligned}
\tag{1.16}
$$

Finally, we impose the following gauge condition:

$$\partial^\nu\overline{h}_{\mu\nu} = 0, \tag{1.17}$$

known as the Lorenz gauge. This allows Eq. 1.16 to be written as

$$
\begin{aligned}
\Box\overline{h}_{\mu\nu} &= -\tfrac{16\pi G}{c^4}T_{\mu\nu} \\
&= 0,
\end{aligned}
\tag{1.18}
$$

where we use the fact that we are only interested in vacuum solutions to set the right-hand side equal to zero. Eq. 1.18 is simply the three dimensional wave equation, the solutions to which are plane waves that travel at the speed of light

$$
\begin{aligned}
\overline{h}_{\mu\nu} &= A_{\mu\nu}\exp(ik_\alpha x^\alpha) \\
&= A_{\mu\nu}\exp[i(\mathbf{k}\cdot\mathbf{x} - \omega t)].
\end{aligned}
\tag{1.19}
$$

$A_{\mu\nu}$ is a constant, symmetric, spacial tensor that describes the amplitude of the wave and k_α is the wave vector with elements $(\omega/c, k_1, k_2, k_3)$. The condition $k_\alpha k^\alpha = 0$ gives the velocity of the wave as

$$\begin{aligned}
v &= \omega/|\mathbf{k}| \\
&= \omega/\sqrt{k_1^2 + k_2^2 + k_3^2} \quad\quad (1.20) \\
&= \omega/k_0 = c
\end{aligned}$$

One final gauge freedom allows us to reduce the number of independent coefficients in Eq. 1.19 from 10 to 2. This is done by transforming into the Transverse Traceless gauge $(\bar{h}_{\mu\nu} \to \bar{h}_{\mu\nu}^{TT})$, which imposes the following conditions on the solutions $\bar{h}_{\mu\nu}^{TT}$:

$$\begin{aligned}
\bar{h}_{0\nu}^{TT} &= 0 \quad\quad \text{(Spatial)} \\
\partial^\mu \bar{h}_{\mu\nu}^{TT} &= 0 \quad \text{(Transverse)} \quad\quad (1.21) \\
\eta^{\mu\nu} \bar{h}_{\mu\nu}^{TT} &= 0 \quad\quad \text{(Traceless)}
\end{aligned}$$

Furthermore, since $\bar{h}_{\mu\nu}^{TT}$ is traceless $(\bar{h}^{TT} = 0)$, it follows from Eq. 1.14 that $\bar{h}_{\mu\nu}^{TT} = h_{\mu\nu}^{TT}$, and we can revert to $h_{\mu\nu}^{TT}$ notation.

The form of the solution can be further simplified by setting the wave propagation direction to $\hat{\mathbf{z}}$. That is, $k_\alpha = (\omega/c, 0, 0, k_3)$. Keeping the real part of Eq. 1.19, what remains is an expression for the time-varying amplitude of the two polarizations of the gravitational wave perturbation as a function of z:

$$h_{ab}^{TT}(t, z) = \begin{pmatrix} h_+ & h_\times \\ h_\times & -h_+ \end{pmatrix} cos[\omega(t - z/c)], \quad\quad (1.22)$$

where $a, b = 1, 2$ are the x and y indices. Due to the symmetry of $h_{\mu\nu}^{TT}$, h_+ and $h_\times$ are the only remaining free coefficients, which give the amplitudes of the *plus* and *cross* polarizations of the wave.

1.2. Gravitational Wave Interaction with Test Masses

To demonstrate the effect of a passing gravitational wave on a set of test masses, we construct a hypothetical circle of point masses which lie in the $x - y$ plane. A gravitational wave traveling in the $\hat{\mathbf{z}}$ direction will change the proper distance between the particles by an amount ΔL which is proportional to the amplitude of the metric components. To quantify this effect, we begin with the geodesic (or distance element) given in Eq. 1.1 and insert the linearized solutions to the Einstein equation found above (Eq. 1.22). To simplify things, we consider a wave that is purely plus-polarized (that is, $h_\times = 0$), which yields the distance element

$$ds^2 = -c^2 dt^2 + [1 + h_+(t)]dx^2 + [1 - h_\times(t)]dy^2 + dz^2. \tag{1.23}$$

At time t, two points with coordinates $(t, x_1, 0, 0)$ and $(t, x_2, 0, 0)$ are separated by the *coordinate* distance $L_x = x_2 - x_1$. Then Eq. 1.23 gives the *proper* distance between the two points as:

$$
\begin{aligned}
s &= (x_2 - x_1)[1 + h_+(t)]^{\frac{1}{2}} \\
&\simeq L_x[1 + \tfrac{1}{2}h_+(t)],
\end{aligned}
\tag{1.24}
$$

where we've used the Taylor series approximation which is valid for small values of h_+. The overall *change* in length expressed as a fraction of the original length is given by

$$\frac{\Delta L_x}{L_x} = \frac{s - L_x}{L_x} \simeq \frac{L_x h_+(t)}{2}. \tag{1.25}$$

9

For an oscillating wave (t not constant), we will use ΔL_x^{max} to represent the maximum variation in L_x which is simply given by $\Delta L_x^{max} = 2\Delta L_x$. Then, the maximum variation in L_x can also be expressed as a fraction of the average distance L_x:

$$\frac{\Delta L_x^{max}}{L_x} = \frac{2\Delta L_x}{L_x} \simeq h_+. \tag{1.26}$$

The same argument can be used to calculate distance changes in the y-direction, or applied to cross-polarized gravitational waves. The resulting motion of the circular arrangement of test masses described above for both plus and cross polarizations is depicted in Figure 1.1. Plus-polarized waves alternately stretch and contract lengths in the x and y directions. For purely cross-polarized waves, this motion is rotated by $45°$ in the $x - y$ plane. Circularly polarized gravitational waves are constructed as follows:

$$\begin{aligned} h_{\circlearrowright} &= \tfrac{1}{\sqrt{2}}(h_+ + ih_\times) \\ h_{\circlearrowleft} &= \tfrac{1}{\sqrt{2}}(h_+ - ih_\times) \end{aligned} \tag{1.27}$$

where $h_{\circlearrowright}$ and $h_{\circlearrowleft}$ are the right- and left-handed circular polarizations, respectively.

1.3. Generation of Gravitational Waves

Finding the vacuum solution to the linearized Einstein equation solves the problem of determining how test masses react to gravitational waves. But in order to determine how GWs are produced, we must return to the non-vacuum form of Eq. 1.18 which we recall here:

$$\Box \bar{h}_{\mu\nu} = -\frac{16\pi G}{c^4} T_{\mu\nu}. \tag{1.28}$$
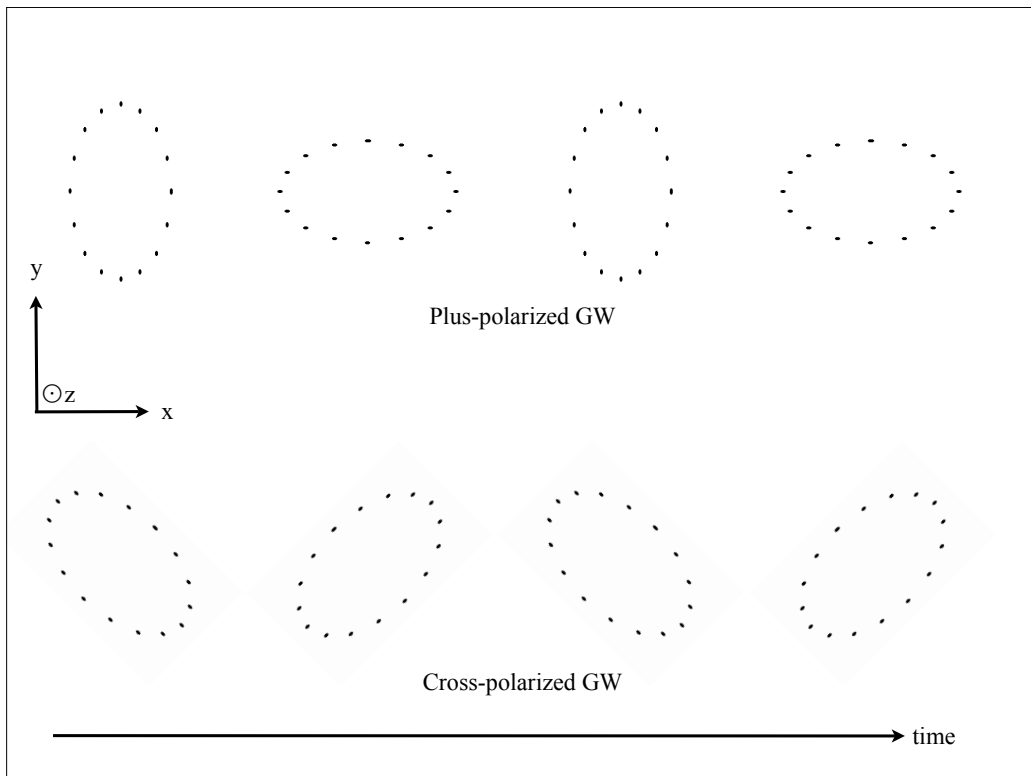
FIGURE 1.1.   The motion of test masses due to incident plus- and cross-polarized gravitational waves traveling in the $\hat{\mathbf{z}}$ direction. Distances between objects are alternately lengthened and contracted in the direction of polarization as time progresses.   The cross polarization (bottom panel) is a 45° rotation of the plus polarization (top panel).

Solutions are obtained by using the Green function which solves the wave equation given a source which is a delta function. That is,

$$\Box_x G(x^\sigma - y^\sigma) = \delta^4(x^\sigma - y^\sigma), \tag{1.29}$$

where $\Box_x$ operates with respect to the x^σ coordinates. Then, the solution to Eq. 1.28 is given by

$$\overline{h}_{\mu\nu}(x^\sigma) = -\frac{16\pi G}{c^4} \int G(x^\sigma - y^\sigma) T_{\mu\nu}(y^\sigma) d^4 y. \tag{1.30}$$

In particular, the *retarded* Green function is needed, which takes the form

$$G(x^\sigma - y^\sigma) = -\frac{1}{4\pi|\mathbf{x} - \mathbf{y}|} \delta[|\mathbf{x} - \mathbf{y}| - (x^0 - y^0)]\theta(x^0 - y^0), \tag{1.31}$$

where $\mathbf{x}$ and $\mathbf{y}$ are spatial vectors and

$$
\begin{aligned}
\theta(x^0 - y^0) &= 1 \quad x^0 > y^0 \\
&= 0 \quad x^0 \leq y^0.
\end{aligned}
\tag{1.32}
$$

Substituting Eq. 1.31 into Eq. 1.30 and integrating over the y^0 coordinate only, reduces the problem to the following three-dimensional integral:

$$\overline{h}_{\mu\nu}(x^\sigma) = -\frac{4G}{c^4} \int \frac{1}{|\mathbf{x} - \mathbf{y}|} T_{\mu\nu}\left(t - \frac{|\mathbf{x} - \mathbf{y}|}{c}, \mathbf{y}\right) d^3 y. \tag{1.33}$$

Next, we take the Fourier transform of Eq. 1.33, while making the following assumptions: the source is far away at a distance r, and the spatial size of the source is small compared to that distance, ie. $\delta r \ll r$. In addition, we assume that the source is slowly moving, such that $\delta r \ll \omega^{-1}$, where ω is the frequency of the source

emission. The result is an expression for the Fourier transformed metric perturbation:

$$\widetilde{\bar{h}}_{\mu\nu}(\omega, \mathbf{x}) = \frac{4G}{c^4} \frac{e^{i\omega r}}{r} \int d^3 y \widetilde{T}_{\mu\nu}(\omega, \mathbf{y}). \tag{1.34}$$

Integrating the right-hand side of Eq. 1.34 for the spatial components and taking the inverse Fourier transform gives

$$\bar{h}_{ij}(t, \mathbf{x}) = \frac{2G}{rc^4} \ddot{I}_{ij}(t - r/c), \tag{1.35}$$

where $I_{ij}(t)$ is the *quadrupole moment tensor* of the source's energy density T^{00}, and is defined as

$$I_{ij}(t) = \int y^i y^j T^{00}(t, \mathbf{y}) d^3 y. \tag{1.36}$$

A simple example where Eq. 1.35 can be used to calculate the GWs produced by a distant source is the circular orbit of two point masses, such as a binary star system. Two stars of mass M, separated by a distance $2R$, and orbiting one another other in the $x - y$ plane will have an orbital angular frequency of:

$$\Omega = \frac{2\pi}{T} = \left(\frac{GM}{4R^3} \right)^{1/2}, \tag{1.37}$$

where T is the period of the orbit, and we have simply used the Newtonian approximation for the oribit. The x and y positions of the two stars (denoted a and b) are given by:

$$
\begin{aligned}
x_a &= R\cos\Omega t, & y_a &= R\sin\Omega t \\
x_b &= -R\cos\Omega t, & y_b &= -R\sin\Omega t.
\end{aligned} \tag{1.38}
$$

The energy density function for point sources uses the delta function:

$$T^{00}(t, \mathbf{x}) = M\delta(x^3)[\delta(x - R\cos\Omega t)\delta(y - R\sin\Omega t)$$
$$+\delta(x + R\cos\Omega t)\delta(y + R\sin\Omega t)]. \tag{1.39}$$

Substituting Eq. 1.39 into Eq. 1.36, performing the integration, and inserting the resulting I_{ij} into Eq. 1.35, gives the following form of the metric perturbation as a function of t and observer position x:

$$\bar{h}_{ij}(t, \mathbf{x}) = \frac{8GM}{rc^4}\Omega^2 R^2 \begin{pmatrix} -\cos 2\Omega(t - r/c) & -\sin 2\Omega(t - r/c) & 0 \\ -\sin 2\Omega(t - r/c) & \cos 2\Omega(t - r/c) & 0 \\ 0 & 0 & 0 \end{pmatrix}. \tag{1.40}$$

To determine the amplitudes of the plus and cross polarizations that are observed, the result (Eq. 1.40) must be projected into the TT gauge at the position of the observer. For an observer on the z-axis, far from the source, the h_+ and $h_\times$ waveforms are given by:

$$\begin{pmatrix} h_+(t) \\ h_\times(t) \end{pmatrix} = -\frac{2G}{rc^4}MR^2\omega_{GW}^2 \begin{pmatrix} \cos(\omega_{GW}t_r) \\ \sin(\omega_{GW}t_r) \end{pmatrix}, \tag{1.41}$$

where we have made the substitution $\omega_{GW} = 2\Omega$ for the angular frequency of the gravitational wave, and $t_r = t - r/c$ for the retarded time. Likewise, for an observer on the $x - y$ plane far from the source, the polarizations are

$$\begin{pmatrix} h_+(t) \\ h_\times(t) \end{pmatrix} = -\frac{G}{rc^4}MR^2\omega_{GW}^2 \begin{pmatrix} \cos(\omega_{GW}t_r) \\ 0 \end{pmatrix}. \tag{1.42}$$

In general, to an observer located at an inclination angle i with respect to the z axis (or the rotational axis of the binary), the gravitational wave polarization takes

14

the form:

$$\begin{pmatrix} h_+(t) \\ h_\times(t) \end{pmatrix} = -\frac{G}{rc^4} M R^2 \omega_{GW}^2 \begin{pmatrix} (1 + \cos^2 i) \cos(\omega_{GW} t_r) \\ 2 \cos i \sin(\omega_{GW} t_r) \end{pmatrix}. \tag{1.43}$$

For the simple equal-mass binary system we are considering here, the power radiated in gravitational waves is given by:

$$P_{GW} = \frac{128G}{5c^5} M^2 R^4 \Omega^6. \tag{1.44}$$

The h_{rss}^2 value of the observed gravitational wave is defined as the integrated sum of the squares of the h_+ and $h_\times$ polarizations. That is,

$$h_{rss}^2 = \int (h_+^2 + h_\times^2) dt, \tag{1.45}$$

where *rss* stands for *root sum squared*. Given that the total emitted GW energy (E_{GW}) is equal to the integrated power, we can rewrite the h_{rss} of the 'face on' binary system (observed along the z axis), in terms of P_{GW} as follows:

$$\begin{aligned} h_{rss}^2 &= \int (h_+^2 + h_\times^2) dt \\ &= \int \left(\frac{4G^2}{r^2 c^8} M^2 R^4 \omega_{GW}^4 (\cos^2 \omega_{GW} t_r + \sin^2 \omega_{GW} t_r) \right) dt \\ &= \frac{10G}{c^3 r^2 \omega_{GW}^2} \int P_{GW} dt \\ &= \frac{10G}{c^3 r^2 \omega_{GW}^2} E_{GW}. \end{aligned} \tag{1.46}$$

The final relationship between h_{rss} and E_{GW} can be useful for placing bounds on the distance r to potential GW sources, as will be seen in Chapter V. This is especially true when treating the GW progenitor as a *standard candle*, that is, a class of GRB-producing sources for which E_{GW} is always more-or-less the same.

15

CHAPTER II

GAMMA-RAY BURSTS

2.1. Gamma-Ray Bursts Overview

Gamma-Ray Bursts are short and intense bursts of electromagnetic radiation in the high energy γ-ray spectrum which are detected above Earth's atmosphere at a rate of approximately 1 per day. The duration of the bursts ranges from between 10^{-3} and 10^3 seconds long with a majority of the radiation emitted in the 0.1-1 MeV range [5] [6]. Based on the observation of so-called *afterglow* lightcurves, we know that after the primary burst, emission extends into the X-ray and even optical and radio wavelengths. Afterglow redshift measurements along with host galaxy identification of GRBs show that they originate from sources at cosmological distances out to billions of light-years. Additionally, localization of GRBs shows an isotropic sky-position distribution, which further supports their extragalactic origin (since they do not appear to cluster in the plane of the Milky-Way).

Understanding the true nature of GRBs and the celestial events that produce them is an active and ongoing research topic in astrophysics. Due to the atmospheric absorption of γ-rays, GRBs are best observed from Earth-orbiting satellites equipped with specialized γ-ray telescopes. The first GRBs were discovered in 1967 by the Vela satellites. Their origin then was a complete mystery, and although many unknowns still exist, subsequent GRB missions have contributed a great deal to our understanding of them. The BATSE instrument on board the Compton Gamma-Ray Observatory which was launched in 1991 first showed the isotropic distribution of

GRBs [7], and in 1997 the Beppo-SAX satellite detected the first X-ray afterglows of GRBs which led to distance measurements using redshift [8].

The current generation of GRB detecting satellites is comprised of three primary missions: NASA's Swift and Fermi satellites (which are each independently capable of determining GRB positions to a precision of 3 arcminutes (Swift), and 1 degree (Fermi)), as well as the Third Interplanetary Network (IPN3), which as the name suggests, is comprised of a network of spacecraft and uses triangulation to recreate GRB positions with typical 3 arcminute precision. Because this dissertation uses GRB data provided exclusively by Swift, detailed descriptions of Swift and its on-board Burst Alert Telescope (BAT) are provided in Section 4.1.

2.2. Classification of Gamma-Ray Bursts

Classifying GRBs is mainly done by examining their *lightcurves* which show the flux of incident photons in different energy bands as a function of time for a particular event. One of the primary ways of classifying GRBs is based on the duration of the emission. T_{90} is the commonly used measure of duration, and is defined as the time interval during which the cumulative counts in the GRB increase from 5% to 95% above the background. BATSE observations were the first to show the bimodal distribution in the T_{90} values of GRBs it detected. This can be seen clearly in the histogram of BATSE GRB durations shown in Figure 2.1.

A cutoff value of 2 seconds is commonly used to differentiate between so-called *long* ($T_{90} > 2$s) and *short* ($T_{90} < 2$s) GRBs. In addition to duration, short GRBs share other characteristics which are not generally seen in the long GRB sample. For example, short GRBs tend to be found in regions of low star formation in galaxies, whereas long GRBs are found in active star-forming regions. Short GRBs also tend
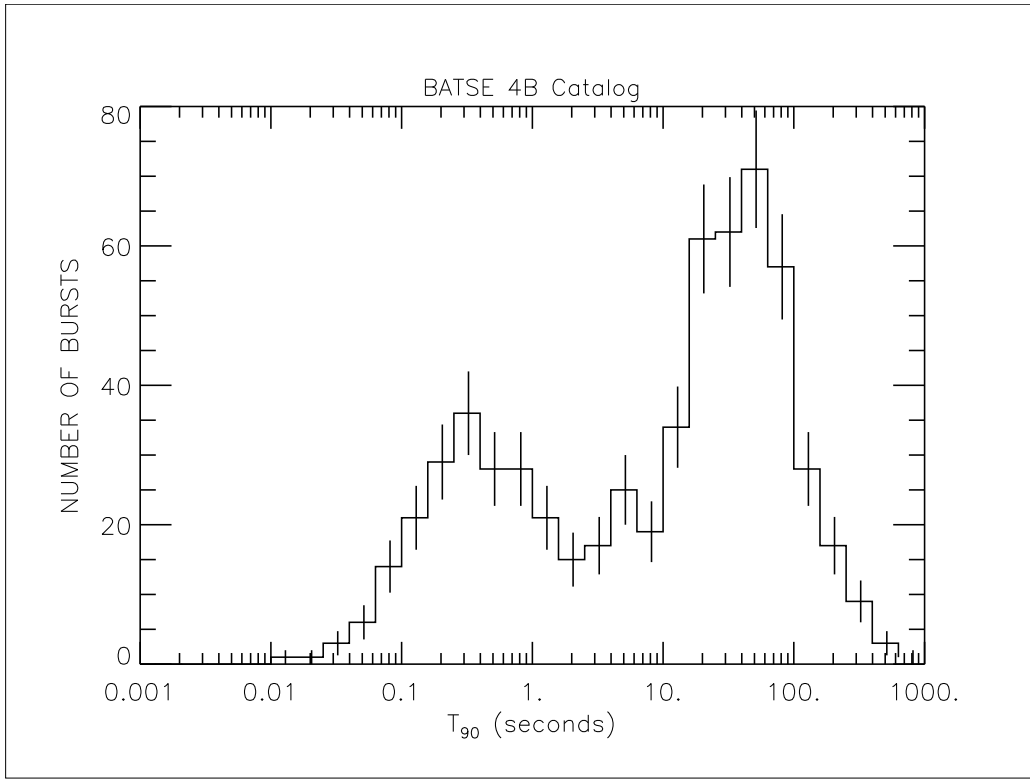
FIGURE 2.1.   Bi-modal distribution of GRB T_{90} values measured by BATSE [7]. Short GRBs have durations < 2 seconds and long GRBs have durations > 2 seconds.

to have harder (higher energy) spectra and lower measured redshifts (with an average of $z \sim 0.5$) than long GRBs, which have typical redshifts of $z = 1 - 2$.

Redshift (z) is a quantity that describes the difference between emitted and observed wavelengths of the electromagnetic radiation from a source that is receding from the observer. It is given by

$$z = \frac{\lambda_o}{\lambda_e} - 1, \tag{2.1}$$

where λ_o and λ_e are the observed and emitted wavelengths, respectively. Due to cosmological expansion, distant objects recede at higher velocities than more nearby objects, and are thus observed with larger redshifts. The relationship between z and proper distance D is given by:

$$D = c \int_0^z \frac{1}{H(z')} dz', \tag{2.2}$$

where the Hubble Parameter $H(z)$ describes the history of the expansion of the universe as a function of redshift[1]. Because large redshifts correspond to more distant sources, the sample of short GRBs with measured redshifts tend to be more nearby than the corresponding long GRB sample.

2.3. Gamma-Ray Burst Progenitors

Due to the distinguishing features of the short and long GRBs, they are believed to originate from two different progenitor classes. A comprehensive overview of GRBs

---

[1]For $z \ll 1$, the distance-redshift relationship reduces to $D \simeq v/H_0 \simeq cz/H_0$, where v is the recessional velocity of the source. H_0 is the current Hubble Parameter and has a measured value of $H_0 \simeq 70 \ \mathrm{km \, s^{-1} Mpc^{-1}}$.

and progenitor theories is given in [9] and [10]. The currently favored mechanisms responsible for short and long GRBs are summarized here.

The leading theory for long GRBs is known as the *collapsar* model, wherein the core of a massive rotating star collapses to form a black hole surrounded by a disk of residual matter. The accretion of this matter onto the black hole powers collimated jets of γ-rays which are emitted in opposite directions along the axis of the system's rotation. Collapsars include a particular type of supernovae (1b/c) which are distinguishable from other supernovae by their hydrogen-deficient spectra. Several long GRBs have been directly associated with type 1b/c supernovae through spectral analysis of optical lightcurves detected in close proximity to the GRB [9, and references therein], providing powerful evidence for the collapsar/supernova theory.

No short GRB has ever been linked to a supernova. Instead, the favored model for the production of short GRBs is the binary inspiral and merging of two neutron stars (NSNS), or a neutron star with a black hole (NSBH). In this scenario, the binary system loses energy in the form of gravitational radiation and eventually the two objects merge to form a stellar mass black hole, surrounded by an accretion disk, similar to the last phase of the collapsar model. Once again, accretion of this matter onto the central black hole is believed to power the beamed γ-ray emission that is observed.

2.4. Gamma-Ray Burst Jets

The isotropic equivalent energy of a typical GRB is huge. This is the γ-ray energy from a single event implied assuming isotropic emission. For GRBs it ranges between 10^{50} and 10^{54} erg, which is comparable to the entire rest mass of the sun

$(M_\odot c^2 \simeq 2 \times 10^{54}$ erg). This is one reason that GRBs are believed to be produced in so-called *jets*, which reduce the total energy requirement to $10^{50} - 10^{51}$ erg.

Evidence for GRB jets is seen as *jet breaks* in the lightcurves of GRB afterglows. In both progenitor models described above, the radiation is produced by a relativistically expanding *fireball* [11, and references therein] restricted to a cone-shaped jet with opening angle θ which is centered on the rotation axis (or $\hat{\mathbf{z}}$), as shown in Figure 2.2. Due to relativistic beaming, an observer at infinity can only see radiation from the internal section of the cone with opening angle Γ^{-1}, where Γ is the Lorentz factor of the fireball moving at speed v:

$$\Gamma = \frac{1}{\sqrt{1 - (v/c)^2}}. \tag{2.3}$$

As the fireball decelerates, Γ decreases and the size of the observation cone increases. However, when the threshold $\Gamma \leq 1/\theta$ is reached, the expansion of the observation cone naturally stops, which is seen as a steepening in the light curve, or a sudden increase in the observed rate of fading. The bottom panel of Figure 2.2 depicts a cartoon version of a lightcurve with such a jet break. The opening angle θ of the jet can be inferred from its shape. Typical GRB opening angles vary between 1 and 20 degrees. Observers at a viewing angle greater than $\theta + \Gamma^{-1}$ will not see any radiation at all. Typical opening angles for short GRBs are $\theta \sim 10°$-$20°$, and for long GRBs are $\theta \sim 5°$, as observed by Swift [12].

Local GRB rate densities can also be inferred from observations. The values commonly quoted are the rate of *observable* GRBs per unit volume. Typical observable rate density estimates are $\sim 10 \, \text{Gpc}^{-3}\text{yr}^{-1}$ for short GRBs, and
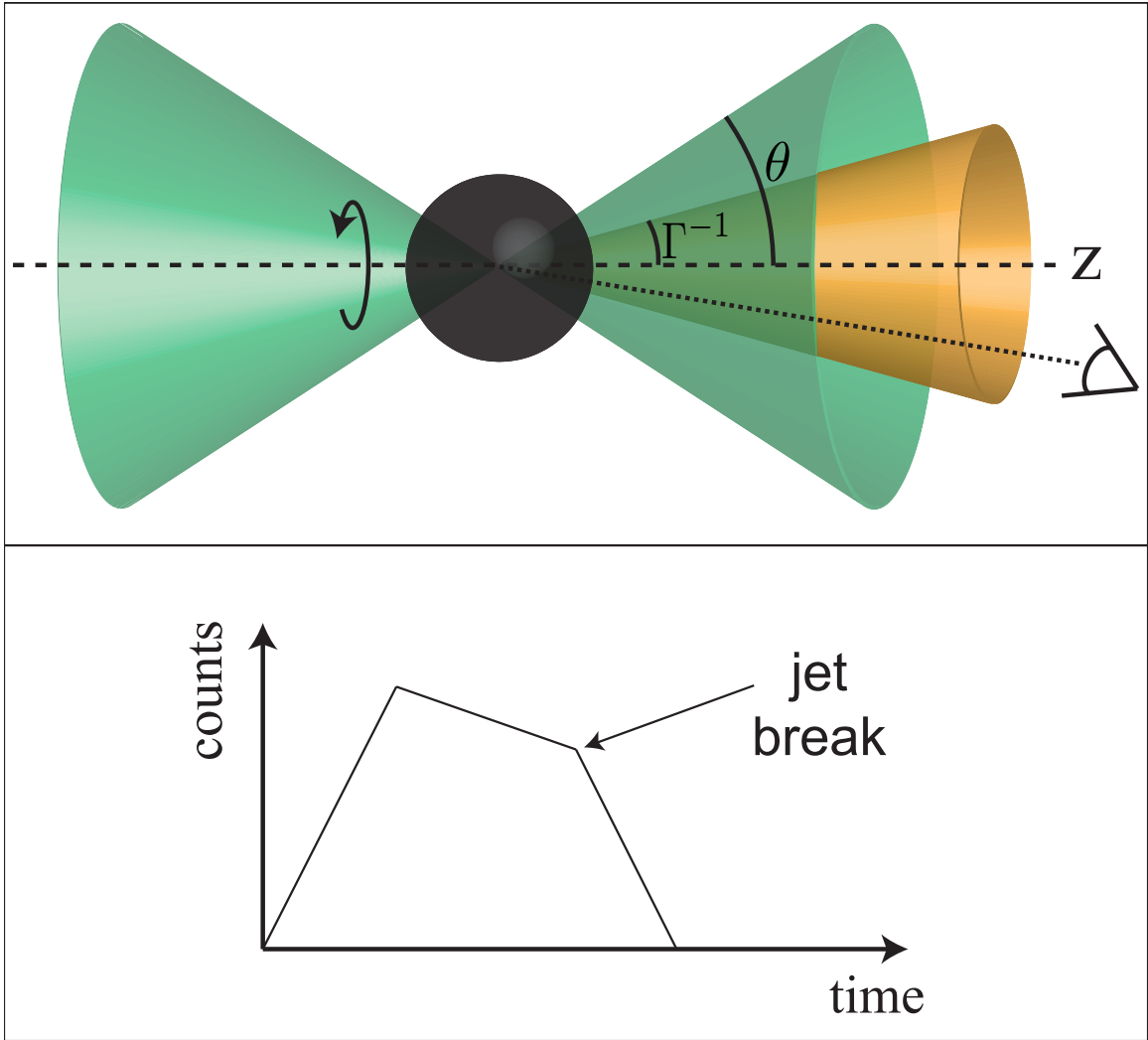
FIGURE 2.2. Emission pattern of GRBs and jet break phenomenon. Top panel: Collimated emission of a GRB progenitor. Because the emission is beamed with Lorentz factor Γ, an observer can only see radiation from a cone with opening angle $\sim\Gamma^{-1}$. Bottom panel: The jet break seen in the lightcurve when Γ reaches $1/\theta$ as the fireball decelerates.

$\sim 0.5\,\mathrm{Gpc}^{-3}\mathrm{yr}^{-1}$ for long GRBs[2] [13]. Although the actual number of observed long GRBs is 5-10 times greater than the number of observed short GRBs, the local rate estimates are corrected for the fact that long GRBs with redshift measurements are typically more distant than short GRBs. This correction factor is clearly significant since it results in a local observable rate for short GRBs that is 20 times greater than that of long GRBs.

2.5. Detecting Gravitational Waves from GRB Progenitors

Progenitors of both long and short GRBs are theoretically capable of producing observable gravitational waves, given the sensitivity of current GW detectors (see Section 3.4). In the case of short GRBs, the GW production is similar to the toy model discussed in Section 1.3. Generalizing the result from Eq. 1.43 for non-equal masses, m_1 and m_2, yields [14]:

$$\begin{pmatrix} h_+(t) \\ h_\times(t) \end{pmatrix} = -\frac{G}{rc^4}\frac{\mu}{2}R^2\omega_{GW}^2 \begin{pmatrix} (1+\cos^2 i)\cos(\omega_{GW}t_r) \\ 2\cos i \sin(\omega_{GW}t_r) \end{pmatrix}, \qquad (2.4)$$

where $\mu = m_1 m_2/(m_1 + m_2)$ is the reduced mass of the system. Therefore, the observed GW amplitude peaks along the axis of rotation ($i = 0$), where coincident GRB detection is most likely. In fact, the overall GW signal strength (received power) at a viewing angle i is weaker than the maximum on-axis signal strength by a factor of [15]:

$$F(i) = \frac{1}{8}[1 + 6\cos^2 i + \cos^4 i]. \qquad (2.5)$$

---

[2]These estimates assume isotropic energy emission, and therefore do not take into account the GRB beaming.

Detecting GWs from long GRBs is less straight-forward because the waveforms are not as well understood. Numerical simulations indicate several different *modes* of GW emission from a stellar collapse. Gravitational waves can be emitted from the initial core-collapse and post-collapse so-called *bounce* phases of the supernova event. However, the resulting GWs are likely too weak to be observed. The most promising sources of detectable GWs from a stellar collapse would come from the excitation of g-modes in the compact object during the accretion phase, or from rotating bar instabilities that can develop in the rotating core [16] [17]. However, since the g-mode studies assume system axis-symmetry, the polarization of the GWs is purely linear ($h_\times = 0$), and goes as $h_+ \propto \sin^2 i$, making the signal minimal near the rotational axis where the detection of coincident GRBs is most likely. However, for bar instabilities (imagine a solid bar that rotates around an axis perpendicular to its length, passing through the center of the bar), the angular dependence of the GW polarization amplitudes is the same as that of a binary system: maximal at the poles. Hence, bar-mode instabilities are the most likely observable phenomenon given a GRB detection.

2.6. Externally Triggered Search

In an externally triggered search for gravitational waves. The time and location of the trigger (in this case a GRB) are used to reduce the number of trials of the analysis, resulting in an increased detection significance[3]. The trials are effectively reduced by only searching in one position on the sky (or a grid covering a small patch

---

[3]The increase in sensitivity can be quantified by the ratio $R = N_{trig}/N_{all-sky}$, where N_{trig} and $N_{all-sky}$ are the expected number of detections from a triggered search and an all-sky search, respectively. R depends on percentage of the sky covered by GRB-detecting satellites, as well as the true distribution of GRB opening angles θ. The GRB-triggered search using LIGO's sixth science run was estimated to have R between 0.1 and 6. R can actually be less than 1 if the sky coverage and GRB opening angles are small enough [18].

of the sky), and by only searching data within a certain time window surrounding the trigger.

In this analysis, it is sufficient to use a single point on the sky, rather than a grid, because of high precision of the Swift GRB localizations (see Section 4.1.1). The time window that is used depends on two things: the first is the accuracy of the GRB trigger time (this will be discussed more in Section 4.2.2), and the second is the expected time delay between the GRB and GW arrival. (Given that both GRBs and GWs travel the same speed (c), the time delay only depends on the difference in their respective *emission* times.) Short GRBs are expected to arrive between 0 and 250 seconds *after* the arrival of the gravitational wave, and long GRBs are expected to arrive between 5 seconds *before* and 400 seconds *after* the GW (depending on the model) [18, and references therein]. Adding a safety buffer on each end, this analysis uses a time window of [-600,+60] seconds with respect to the GRB trigger time. (Some additional time is also added to the end of the window to account for error in the GRB trigger time.)

2.7. Motivation for a Low-Threshold Triggered Search

The advantages of using GRB triggers in a GW search were discussed above. Here, we focus on lower-significance GRB triggers and motivate their usefulness to the search.

First, it is important to specify what is meant by a "below-threshold" trigger. These are detections of possible GRBs that are made regularly by GRB-detection telescopes such as Swift's Burst Alert Telescope (BAT). In the case of the BAT, an excess of γ-ray flux in the image domain (an "image peak") is assigned a significance based on the local SNR of the peak in units of sigma [19]. Although the BAT

sensitivity and trigger selection are somewhat more subtle than what is described here and should be considered on a case-by-case basis (see Chapter IV), a high SNR image peak is generally reflective of an event with a large γ-ray flux at the detector. Image peaks with SNR above a certain pre-determined threshold are selected for follow-up observation (and usually confirmed as GRBs), and those that fall below the threshold are rejected. Almost all of the rejected image peaks are the result of background fluctuations or detector noise. However, a sharp cutoff in the SNR distribution of GRB detections below a given threshold is unphysical, and it is safe to assume that a yet unknown number of true GRBs are buried in the noise.

Below we consider several possible reasons for a real GRB to be detected with such a low significance.

An obvious naive assumption is that the detection is weak because the GRB source is very far away. Since the observed brightness of a given GRB will fall off as the distance to the source squared, a weakly-detected GRB may simply have originated from a very distant progenitor. The triggers used in this analysis do not have associated redshift observations, so the distance to each possible progenitor is unknown. For comparison, among those GRBs with a measured redshift, the smallest redshift from the set of triggers used in the main LIGO-Virgo S5 GRB analysis was z=0.125 [20, and references therein], corresponding to a distance of D=578 Mpc, which is well out of the current LIGO-Virgo detection range. (It is important to note, however, that only 30% of the GRBs had redshift measurements). If the only result of lowering the GRB detection threshold is to increase the distance limit of observing them electromagnetically, then it is unlikely that any of the new triggers would be close enough to be detected gravitationally.

Since the possibility of uncovering more distant – and therefore weakly observed – GRBs does not motivate this analysis, the remainder of this discussion explores the prospects for discovering relatively nearby faint GRBs with detectable GW counterparts.

It is already well-known that observed GRB brightness (or dimness) is not due to source proximity (or distance) alone. An example is the fact that short GRBs tend to be fainter yet have smaller associated redshifts than long GRBs [21]. This in itself is promising for GW detection because of the much stronger GW emission expected from the progenitors of short GRBs.

One explanation for distance-independent variability in GRB brightness has to do with the jet phenomenon discussed in Section 2.4. How this collimation leads to faint GRB detections depends on which jet model one considers: The angle-dependent jet model for GRBs suggests that the variation in observed GRB lightcurves is due to a non-uniform jet profile and varying off-axis viewing angles. Rather than dropping off abruptly at some angle θ_j, the GRB emission, according to this model, peaks along the axis and falls off proportional to θ^{-2} [22]. However, in the homogeneous jet model the edges of the jet are well-defined within the opening angle θ_j and fall off sharply for observation angles $\theta_o > \theta_j$. In this case, a so-called *low-luminosity* (LL) GRB would correspond to a GRB viewed just outside the opening angle, before the emission falls off completely [23]. In either jet profile scenario, lowering the GRB detection threshold would effectively increase the maximum viewing angle and pick up off-axis GRB events buried in the noise.

A potential increase in the number of off-axis GRB events begs the question of whether this is advantageous in a gravitational wave search. Because GW emission of inspiral events and bar-mode instabilities is much more isotropic than the expected

27

γ-ray emission for these progenitors (see Section 2.5), the usefulness of such events in a GW search is only slightly diminished by the non-ideal observation angle. Through Eq. 2.5 we see that an event viewed 30° off-axis which might be nearly unobservable in γ-rays (depending on the opening angle), would still contain 76% of its maximum gravitational wave signal strength.

Perhaps the most convincing case for studying sub-luminal detections comes from recent evidence for the existence of a separate nearby population of low-luminosity (LL), long-duration GRBs that is much larger than previously believed. LL-GRB studies have been strongly motivated by the fact that the two nearest GRBs with redshifts were both sub-luminous and possessed similar unique spectral properties. Lightcurve features from GRBs 980425 and 060218 (located at 36 Mpc and 153 Mpc, respectively) indicate that they may originate from a different progenitor class than the high-luminosity events, or even, as touched upon above, that they are typical GRBs viewed off-axis. Whatever the mechanism, based on the observation of these long GRB outliers, a local LL-GRB rate between $\sim$200 and $\sim$700 Gpc^{-3}yr^{-1} has been inferred, a full 3 orders of magnitude larger than the normal long GRB rate [24] [25].

The rate densities given above can be used to estimate the local rate of observable LL-GRB events with gravitational wave counterparts that would be detectable by the LIGO-Virgo interferometer network [13]. Assuming isotropic emission of circularly polarized GWs and a non-optimally oriented observer, the luminosity distance is given approximately by:

$$D \simeq \left(\frac{G}{\pi^2 c^3} \right)^{1/2} \frac{E_{GW}^{1/2}}{f_0 h_{rss}},$$ (2.6)

which is similar to Eq. 1.46, where a 0° observation angle was assumed. Here, we insert the total emitted GW energy $E_{GW} = 0.01\,M_\odot c^2$, and a frequency $f = \omega_{GW}/2\pi = 150$ Hz, which is right in the peak sensitivity region of the detectors.

28

Finally, given the h_{rss} sensitivity of the instruments during the time this data was collected (LIGO science run 5 (S5) and Virgo science run 1 (S1)), we get an average 'observable' distance $D \simeq 15$ Mpc. To convert this distance to a rate, we multiply the LL-GRB rate density ρ_0 by the total GW observation volume and the fraction of the sky that is observable. This gives

$$R_{GWB} = \rho_0 \left(\frac{4}{3} \pi D^3 \right) \frac{\Omega}{4\pi}, \tag{2.7}$$

where $\Omega = 1.5$ sr is the Swift BAT field of view, and the result R_{GWB} is the estimated rate of detectable GW bursts from LL-GRBs seen by Swift. Therefore, for the two different values of ρ_0 given above (200 and 700 Gpc^{-3}yr^{-1}), we obtain detectable event rates of $\sim 3 \times 10^{-4}$ yr^{-1} and $\sim 1 \times 10^{-3}$ yr^{-1}, respectively. However, these rates do not take into account the fact that the GRBs are beamed, since the ρ_0 values are isotropic equivalent rates. (Correcting for beaming would effectively increase the local rate density estimates.) Without this correction, the most optimistic LL-GRB rate estimate is on the order of 1 event per 1000 years. However, there are large uncertainties inherent in this estimate, stemming in part from the assumption of isotropic γ-ray emission mentioned above. Another large uncertainty comes from the value chosen for E_{GW}. The value $0.01 \, M_\odot c^2$ is most appropriate in the case of a binary inspiral progenitor (for which $E_{GW} \simeq 0.01(M_1 + M_2)c^2$), but is unrealistically large for long GRB progenitors (see Section 5.2).

In short, there are still many unanswered questions relating to the true nature of GRBs, and LL-GRBs in particular. Although the expected GW detection rate is small, the argument for studying even the faintest events is compelling since it is very possible that they dominate the nearby GRB population. The aim of this analysis is to retrieve such events from the Swift data archive by reaching below the

current detection threshold. The prediction, motivated by the reasons above, is that a small fraction of the resulting triggers are real GRBs from gravitational wave-emitting progenitors in the nearby universe.

CHAPTER III

INTERFEROMETRIC GRAVITATIONAL WAVE DETECTORS

The basic principle for detecting gravitational waves was touched on in Section 1.2. The essential goal is to detect length changes (ΔL) caused by incident GWs. Advanced interferometers (IFOs) are currently the most sensitive instruments designed for this purpose. An excellent description of interferometric GW detectors is given in [26] and [27]. This chapter will present an overview of the basic design, operation, and sensitivity limits of the IFO network used in this analysis.

3.1. Detector Design

Recall that the GW amplitude is proportional to the fractional length change:

$$h_{rss} \sim \frac{\Delta L}{L}. \tag{3.1}$$

Therefore, in order to maximize ΔL for a given h_{rss} amplitude, the size of the detector L must be large. LIGO and Virgo are km-scale detectors. Combined, they comprise 4 independent interferometers (IFOs) in 3 different locations: The 4 km (H1) and 2 km (H2) detectors in Hanford, WA U.S.A., another 4 km (L1) detector in Livingston, LA U.S.A., and the 3 km (V1) detector located in Cascina, Italy.

The basic design of each detector is that of a modified Michelson interferometer with light-recycling Fabry-Perot arm cavities. A schematic of the setup is shown in Figure 3.1. The IFOs work by pointing laser light at a beam splitter which separates it into two identical beams that propagate down the perpendicular x and y arms of the IFO. Each arm is made up of a vacuum-enclosed cavity with two mirrors at

opposite ends. Light in the arms bounces back and forth in the cavities while a small fraction (1/100 per bounce) returns to the beam splitter, where half of it is sent to the power recycling mirror and the other half is recombined with light from the other arm and exits through the output port. The mirrors, which are also the test masses in this setup, are suspended by wires and are therefore free to move in a direction parallel to the arm under the influence of a GW. Any length differences between the x and y arms will result in a phase difference between the two beams as they exit the cavities. This is observed as an interference pattern in the recombined light, which is sensed by a photodetector at the output port.

Although the actual distance between the test masses (in the case of H1, for example) is 4 km, the light-recycling feature increases the effective length to approximately 300 km. The optimal effective path length L_o is that which maximizes the intensity of recombined light at the output port, and depends on the frequency f_{GW} of the targeted GW signal:

$$L_o = \frac{c}{4f_{GW}}. \tag{3.2}$$

For frequencies between 40 Hz and 1 kHz, the optimal path length is $L_o = 75$ km to 1,875 km.

3.2. Antenna Patterns

The response of an interferometer to a GW signal is a function of the antenna pattern (F_+, $F_\times$), which reflects the IFO sensitivity to the h_+ and $h_\times$ polarization amplitudes for different source positions and orientations. The total response of the
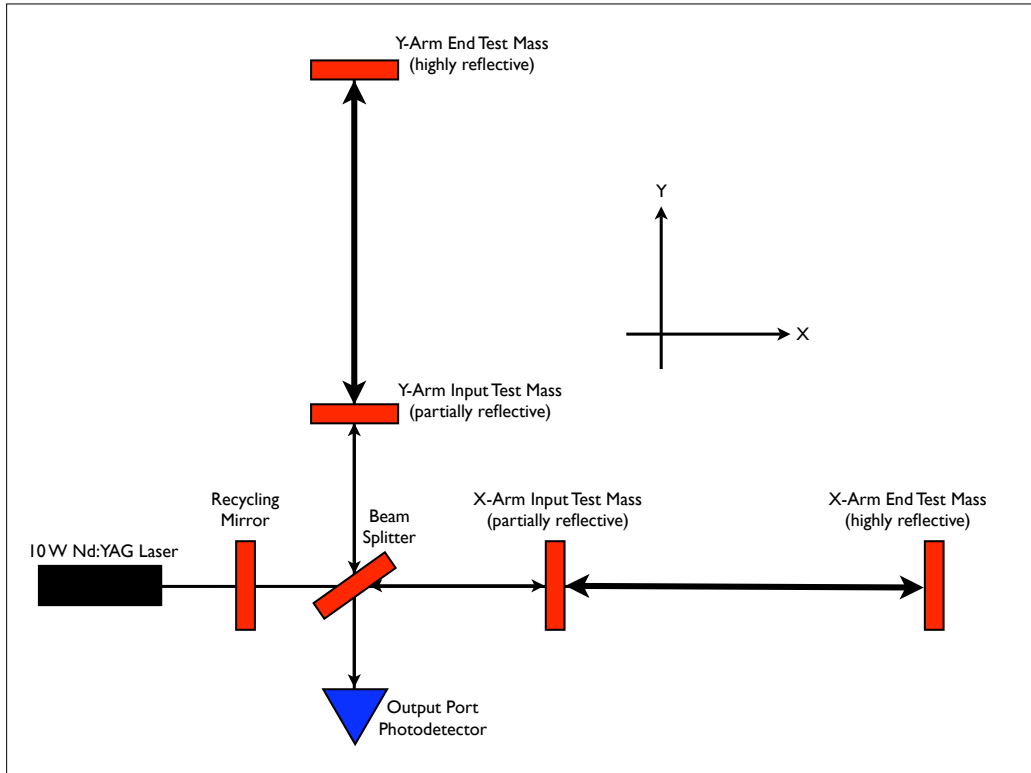
FIGURE 3.1. Simplified schematic diagram of an interferometric gravitational wave detector. Light travels in the direction of the arrows in the figure. A difference in the length of the arms causes the two beams of recombined light to be phase shifted from one another, which is observed at the output port as an interference pattern. The light and dark fringes of the pattern correspond to constructive and destructive interference, respectively. In the case of the LIGO H1 detector, the arm cavity lengths are each 4 km long and uses a 10 W Nd:YAG laser with wavelength $\lambda = 1064$ nm.

detector is given by

$$h(t) = F_+(\theta, \phi, \psi)h_+(t) + F_\times(\theta, \phi, \psi)h_\times(t), \qquad (3.3)$$

where θ and ϕ describe the location of the source in the local spherical coordinates of the IFO reference frame, and are defined as follows: θ is the zenith angle between the IFO z-axis and the line of sight to the source, and ϕ is the azimuth angle between the IFO x-axis and the projection of the line of sight onto the IFO x-y plane. ψ describes the source frame orientation with respect to the IFO, and is defined as angle between x-axis of the source frame, and the projection of the IFO x arm onto the plane orthogonal to the direction of propagation. The antenna pattern functions are given by

$$F_+(\theta, \phi, \psi) = \frac{1}{2}(1 + \cos^2\theta)\cos 2\phi \cos 2\psi - \cos\theta \sin 2\phi \sin 2\psi \qquad (3.4a)$$

$$F_\times(\theta, \phi, \psi) = \frac{1}{2}(1 + \cos^2\theta)\cos 2\phi \sin 2\psi + \cos\theta \sin 2\phi \cos 2\psi. \qquad (3.4b)$$

If we assume that the source is oriented with $\psi = 0$, then the observed gravitational wave amplitude can be computed as a function of source location alone. Figure 3.2 is a graphical illustration of the antenna factors for gravitational waves with different polarizations. In all three cases depicted, the IFO is the most sensitive to sources located directly above (or below) it on the z-axis of the detector, and least sensitive to sources in the x-y plane.
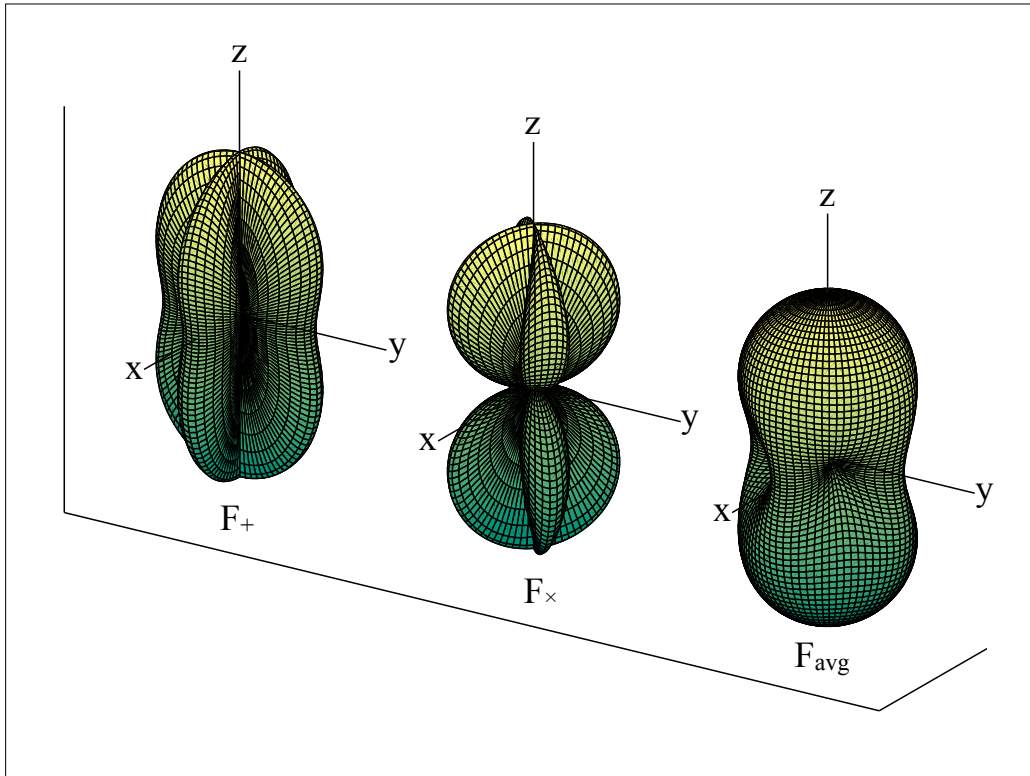
FIGURE 3.2. Antenna Factors as a function of source location for plus-polarization (left), cross-polarization (middle), and no polarization (right). This depicts the interferometer sensitivity to sources located at different positions on the sky.

3.3. Detector Noise

The sensitivity, or noise level of an interferometer is often given as an amplitude spectral density $A(f)$ which has units of $\text{Hz}^{-1/2}$:

$$A(f) = \sqrt{\int h(t)e^{2\pi i f t}dt}. \tag{3.5}$$

The *power* spectral density, therefore, is simply the square of the amplitude spectral density:

$$S(f) = (A(f))^2. \tag{3.6}$$

This representation is useful because it characterizes the noise at the specific frequencies we are interested in. The signal to noise ratio (SNR) of a gravitational wave in the detector is given by

$$\text{SNR} = \sqrt{2\int_{-\infty}^{\infty}\frac{|\tilde{s}(f)|^2}{S(|f|)}df}, \tag{3.7}$$

where $\tilde{s}(f)$ is the Fourier transform of the GW signal $h(t)$ at the detector. For a gravitational wave from an optimally oriented source with only a single frequency component, the SNR reduces to

$$\text{SNR} = \sqrt{2}\frac{h_{rss}}{\sqrt{S(f)}}, \tag{3.8}$$

which provides a simple relationship between the integrated GW amplitude (h_{rss}) and detection SNR.

Figure 3.3 shows the sources of noise that limit LIGO detector sensitivity in different frequency regions [28]. The primary limitations are caused by shot noise at
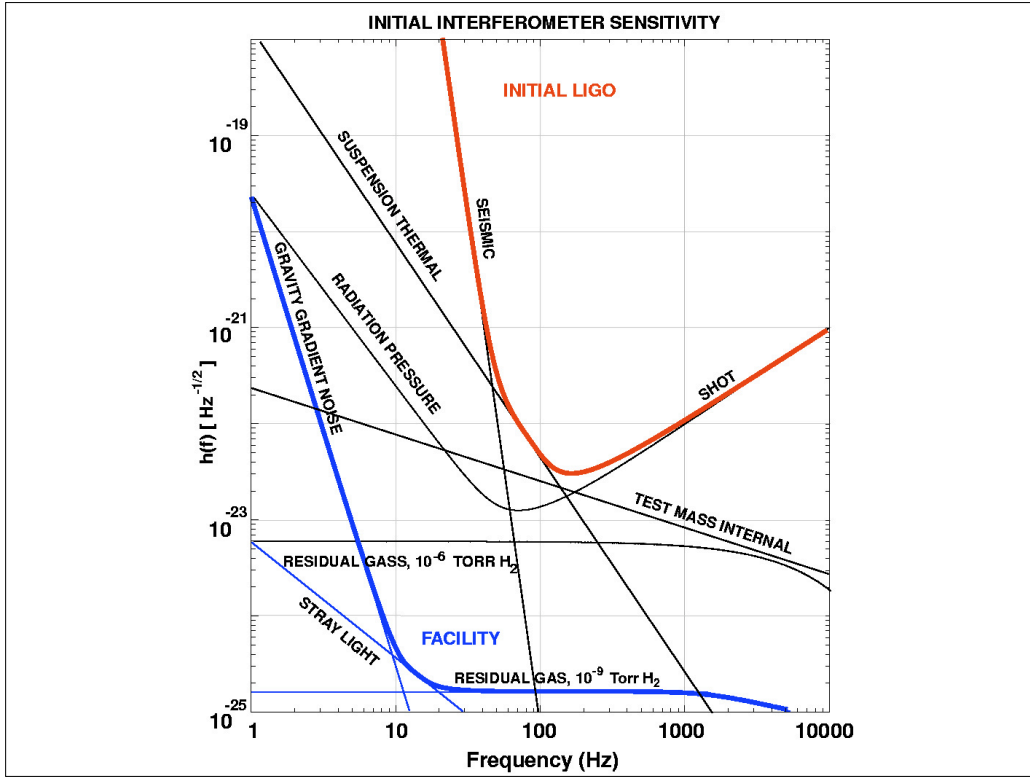
FIGURE 3.3. Amplitude spectral density of noise sources that limit the sensitivity in the initial LIGO design. The primary sources of noise are seismic, thermal noise in the test mass suspension system, and shot noise. Figure is taken from [28].

high frequencies ($\gtrsim$ 200 Hz), seismic noise at low frequencies ($\lesssim$ 40 Hz) and thermal noise in the test mass suspension system at mid-range frequencies (between 40 and 200 Hz). The shot noise is caused by natural fluctuations in the number of photons N that are incident on the output photodetector in a given interval of time. Since shot noise amplitude is proportional to $1/\sqrt{N}$, it can be attenuated by having a high-power laser system.

3.4. Detector Sensitivity from LIGO S5/Virgo VSR1

The LIGO and Virgo detectors were designed to be the most sensitive to gravitational wave signals between $\sim$40 Hz and $\sim$7 kHz, with a peak *design sensitivity* (for H1 and L1) of 10^{-23} Hz$^{-1/2}$ at $f = 150$ Hz. During the LIGO S5 and Virgo VSR1 science runs which collectively spanned a period of two years from November 5, 2005 to October 1, 2007, more than 1 year of triple coincidence[1] data was collected. The IFO duty factors for the run were 75% (H1), 76% (H2), 65% (L1), and 78% (V1)[2]. The best strain sensitivity achieved by all four detectors is show in Figure 3.4. Both H1 and L1 operated very close to the design sensitivity goal in the frequency 'sweet spot' near 150 Hz.

---

[1]Three or more detectors operating simultaneously and taking science-quality data.

[2]The Virgo duty factor is counted from the Virgo start date which was not until May 18, 2007.
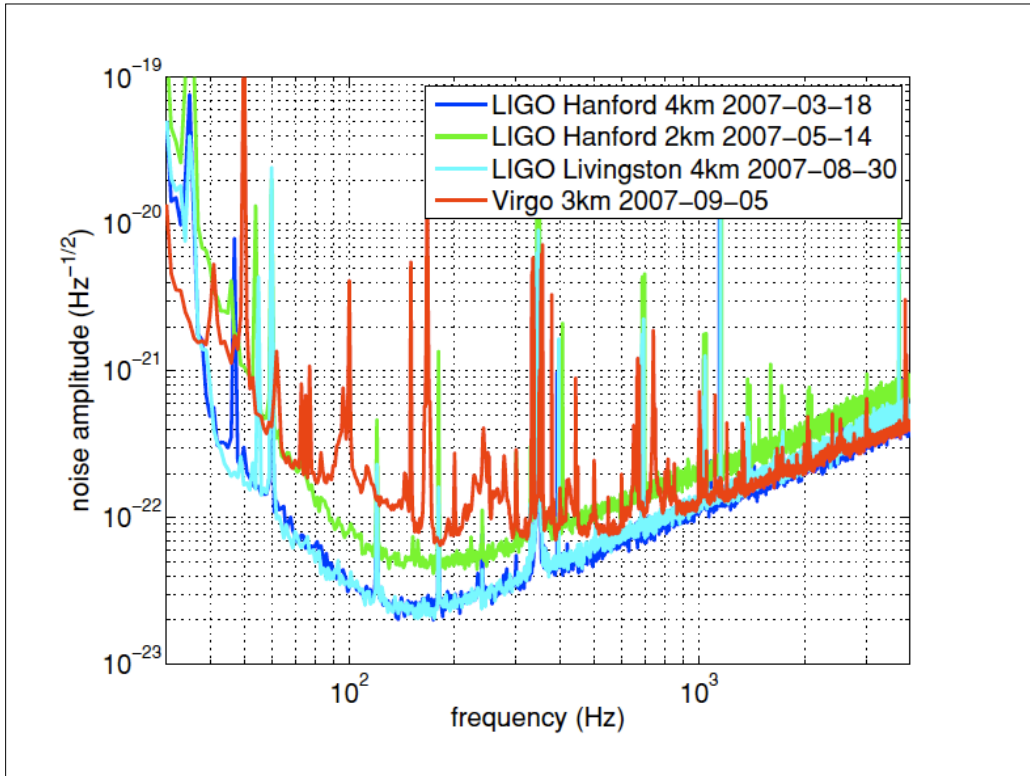
FIGURE 3.4.   Best strain sensitivity of LIGO and Virgo detectors during the S5/VSR1 run [20]. H1 and L1 operated close to the design sensitivity goal of $h \sim 10^{-23}$ Hz$^{-1/2}$ at $f = 150$ Hz.

CHAPTER IV

EXPERIMENTAL METHODS

This chapter is divided into three main parts which together provide the details of the sub-threshold GRB GW search. Section 4.1 gives an overview of Swift, the Burst Alert Telescope, and the method it uses to detect GRBs. Section 4.2 focuses on trigger selection and describes the process of collecting, sorting, and selecting possible GRB triggers, choosing a new lowered threshold, and making a purity estimate of the final trigger sample. Section 4.3 describes the data analysis method used to search for GWs in the interferometer data at the time and location of each trigger. We introduce the analysis code known as 'X-Pipeline', and discuss its theory and implementation.

4.1. Swift Gamma-Ray Burst Explorer

The Swift Gamma-Ray Burst Explorer spacecraft was developed by an international collaboration and is is managed and operated by NASA's Goddard Space Flight Center (GSFC) and by Pennsylvania State University's Flight Operation Team [29] [30] [31]. Swift was launched in November 2004 and maintains a circular low-Earth orbit (LEO) at an altitude of approximately 600 km. Although it was given a primary mission duration of 2 years, it is still in operation at the completion of this thesis (8 years after launch).

The main objective of Swift is to detect and observe GRB lightcurves in multiple wavelength bands with the ultimate goal of classifying the bursts, determining their origin, and using them as a tool to study cosmology and the early universe. There are three detectors on-board Swift that are each sensitive to a different range of

wavelengths or photon energies: the Burst Alert Telescope ($15 - 150\,\mathrm{keV}$), the X-Ray Telescope ($0.2 - 10\,\mathrm{keV}$), and the UltraViolet/Optical Telescope ($170 - 650\,\mathrm{nm}$).

The Burst Alert Telescope (BAT), which technically operates in the hard x-ray (or soft γ-ray) regime, detects the first onset of a GRB. With its large field of view (FOV $\approx 1.5\,\mathrm{sr}$ with 50% partial coding fraction[1] [19]), the BAT is able to survey the sky for sources, determine the sky location of each source to an accuracy of 1-4 arcminutes, and pass the information to scientists on the ground. The location information is also passed to the spacecraft so that it can perform an automatic slew (or rotation) to point the other two instruments (with their narrower FOVs) directly at the GRB source for further observation. The spacecraft slew is rapid, and within a minute of the GRB onset all three detectors are pointing at the source. Data from the burst is telemetered to the ground, and within hours the ground-based software is able to produce calibrated lightcurves of the event showing how the emission evolves over time through a wide range of energies. The shape and spectral properties of these lightcurves provide information that is essential for classifying GRBs and gaining an understanding of their progenitor systems.

4.1.1. The Burst Alert Telescope

The BAT detector [32] was designed and built at Goddard Space Flight Center. It is a plane made up of approximately 32,000 photon-counting CdZnTe detector elements spanning an area of $5,240\,\mathrm{cm}^2$. Each element is able to detect an individual incident γ-ray photon and resolve its energy. Because of the high energies involved, traditional focusing optics do not work in the γ-ray spectrum. Therefore, in order to determine the direction from which a burst of γ-ray photons originated, the BAT uses

---

[1]Events within this FOV are at least 50% partially coded, meaning that the shadow cast by the coded-aperture mask illuminates at least 50% of the detector area (see Section 4.1.1).
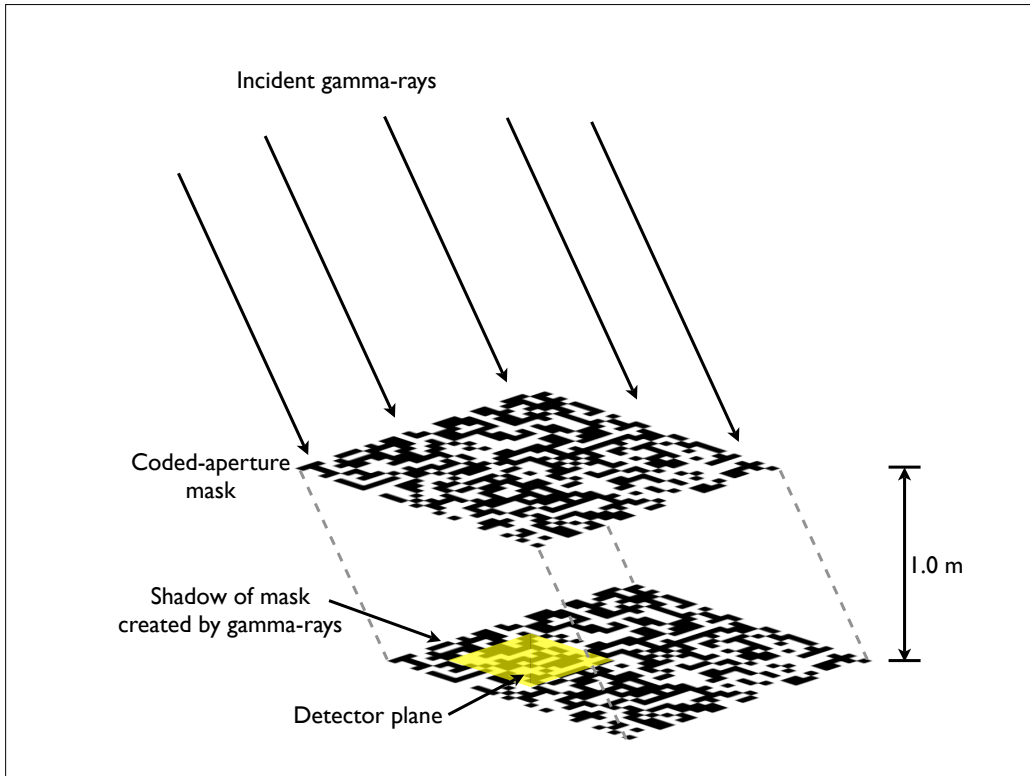
FIGURE 4.1. Burst Alert Telescope source localization using coded-aperture imaging. For each source position on the sky, the 50% open coded-aperture mask creates a unique shadow pattern on the detector plane, located 1 m below it.

the technique of coded-aperture imaging. A coded-aperture is a lead mask located 1 m above the detector array consisting of a random pattern of ∼52,000 square 'open' or 'closed' pixels, with an open fraction of 50%. The pixel size is 5 × 5 mm, with a mask thickness of 1 mm, designed to block 90% of 150 keV incident radiation. When γ-rays pass through the aperture, the mask pattern creates a shadow on the detector plane that depends uniquely on the location of the source in the BAT's FOV.

For each BAT exposure, a detector plane image (DPI) is created, which is a rectangular map giving the number of counts in each individual detector. Images of the sky are produced by cross-correlating the DPI with the the expected shadow

pattern from each possible source position on the sky. If a source is present at a certain position, there will be an excess in the cross-correlation product corresponding to that position. The resulting image, with its pixel size of 17 arcmin, is then scanned for regions of excess flux to identify bright sources. If a new source or so-called 'image peak' is present, it is assigned a significance based on its flux.

Image peaks above a certain significance threshold are *back-projected* in order to get a more accurate measure of their position and significance. This method involves ray-tracing each detector count back towards the source position. Rays that encounter a closed mask element are added to the background count, and rays that encounter an open element are added to the source count. The estimate of actual counts that came from the source is obtained by subtracting the background total from the source total.

The resulting re-imaged peak has a position error radius of only $1 - 3$ arcmin depending on its significance value, which is typically quoted as a signal to noise ratio (SNR) and given in units of σ, where σ is the standard deviation of the background noise distribution. In the case of a 50%-open coded-aperture mask, the SNR is given by [33], [34]

$$\text{SNR} = \frac{f_m C_s}{\sqrt{C_s + B}}, \tag{4.1}$$

where C_s is the total number of detector counts from the signal, B is the total number of background counts, and the factor f_m is included to compensate for the finite size of the detector pixels. (For the BAT, $f_m \approx 0.73$.) Setting a threshold on the SNR of image peaks is one of the primary methods used by the BAT software to determine whether they are true GRB candidates and worthy of follow-up observations.

4.1.2. GRB Detection

There are two different ways that Swift detects GRBs [19]. Typically the BAT operates in *survey mode*, where it accumulates energy spectra for each of its detectors, but does not produce any images. A 'rate trigger' occurs when the count rate summed over the detector elements in a particular energy band exceeds some pre-determined threshold. At the onset of a rate trigger, the BAT produces an image of the sky in order to confirm the existence of a new point source and determine its location. The image is compared to an on-board source catalog to remove known sources. If there are any surviving peaks in the image, the BAT uses two different thresholds (TH_{low} and TH_{high}) and will respond in one of three ways depending on the peak's significance SNR_{peak}:

1. If $SNR_{peak} < TH_{low}$, the image peak is ignored.

2. If $SNR_{peak} \geqslant TH_{high}$, the spacecraft initiates a GRB response (including GRB announcement to ground-based scientists and telescopes, spacecraft slew, and follow-up observations).

3. If $TH_{low} \leqslant SNR_{peak} < TH_{high}$, then one of two things can happen:

   a. If a higher rate trigger occurs while the first image is being processed, the initial image peak is ignored and another image is produced corresponding to the higher rate trigger time interval. Any peaks in this new image are then subject to the same TH_{low} and TH_{high} threshold tests (go back to step 1).

   b. If *no* higher rate triggers occur while processing the first one, then the spacecraft initiates a GRB response.

The threshold values can be modified by scientists on the ground based on the behavior of the noise distribution and the desired *false alarm rate* (the percentage of GRB 'detections' that turn out to be the result of noise fluctuations). During the LIGO and Virgo science runs used in this analysis (S5/VSR1), the threshold values of TH_{low} and TH_{high} were set to $6.5\,\sigma$ and $7.0\,\sigma$, respectively.

The second way that the BAT detects GRBs is by periodically producing sky images even when there is no rate trigger. These images are also scanned for peaks above a certain significance level. A third threshold TH_{image}, is used on these 'image only triggers' (henceforth in this thesis referred to as *image triggers*). TH_{image} is a hard threshold such that there are only two possibilities resulting from an image trigger peak:

1. If $\text{SNR}_{peak} < \text{TH}_{image}$, the image peak is ignored.

2. If $\text{SNR}_{peak} \geqslant \text{TH}_{image}$, a GRB response is initiated.

Just like the rate trigger thresholds, TH_{image} is a commandable parameter which, during S5/VSR1, was set to $7.0\,\sigma$.

4.2. Trigger Selection

The process of selecting GRB triggers to use in the analysis is described below. The two main steps are collecting image peak data, and choosing a new threshold, which involves making an estimate of the sample purity. The primary codes used in the trigger selection process and further documentation can be found online at the following URL: http://zebu.uoregon.edu/~uoligo/Emelie/Subprime/scripts/.

45

4.2.1. Image Peak Data Collection

One of the primary tasks of this thesis is deciding on a set of new lowered thresholds to use in selecting possible GRB triggers for the GW search. In order to do this, one requires a trigger sample to begin with. The collection of triggers we have to choose from is the set of all Swift BAT image peaks resulting from both rate triggers and image triggers that occurred during S5/VSR1 that did not result in a GRB response. This section will describe how the raw image peak data is collected, parsed, and finally 'weeded' to remove uninteresting events.

When an image peak passes the appropriate threshold tests and a GRB response is commenced, the information about the peak is sent electronically to scientists and researchers on the ground through the so-called *Gamma-Ray Coordinates Network* (or GCN). The *GCN notices* which are received in the form of emails (but are also accessible on the web [35]), provide the time, location, position accuracy, duration, and significance of the burst along with other data relevant to astronomers and GRB physicists.

Unfortunately, when an image peak does *not* trigger a GRB response, none of this information about the peak is readily available. However, the data is publicly available in its raw form via the Swift data archive [36]. Collecting and converting this information into a usable format (from data spanning the approximate 2-year LIGO/Virgo science run) involves downloading, processing, and parsing thousands of files. For the purpose of this thesis, various scripts are used to automate this process. The main steps are summarized here:

1. Download raw data files: A Perl script is used to automatically download all of the relevant BAT files that contain image peak data. The following information is needed for each peak:

46

– **Sky location** - the right ascension (RA), and declination (Dec) of the peak in celestial coordinates.

– **Time** - the GPS start and stop time of the imaging interval during which the peak was found.

– **Strength** - the SNR of the image peak (SNR_{peak}).

– **CatNum** - the *catalog number* of any known source that overlaps with the peak position. (If CatNum=0, then the peak is not associated with a previously cataloged source and is therefore a possible GRB candidate.)

The information is contained in two different file types on the data archive:

i. **'Image' files:** These files contain a record of every image peak detected by the BAT. They are easy to parse, include precise SNR_{peak} values, but do not give the celestial coordinates of the peak. The directory location of image files in the data archive [36] is:

/swift/data/trend/YYYY_MM/bat/btbimgtr/swNNNNNNNNNNNbittb.fits.gz, where 'YYYY' is the year, 'MM' is the 2-digit month, and 'NNNNNNNNNNN' is the observation number.

ii. **'Debug' files:** These files contain a data stream describing the BAT's operational state. They are difficult to parse (not in tabular format), contain imprecise (truncated) SNR_{peak} values, but do give the celestial coordinates of each peak. The directory location of debug files in the data archive is:

/swift/data/trend/YYYY_MM/bat/bshelllg/swNNNNNNNNNNNbshtb.fits.gz.

After the files are downloaded, they are converted from FITS (Flexible Image Transport System) format into ASCII files using a software package called FTOOLS

47

provided by NASA's High Energy Astrophysics Science Archive Research Center (HEASARC) [37].

2. Parse files and compare image peaks: A set of MATLAB-based codes are used to parse the ASCII files to search for peaks. The resulting peaks from the debug and image files are sorted and compared to compile the full data set for each peak. However, since many of the peaks from the image files are missing in the debug files, the celestial sky-location data was initially not available. To fill in this data, a separate set of scripts and FTOOLS functions is implemented to download spacecraft attitude files and use them to convert peak coordinates in the image file into celestial coordinates.

3. Remove uninteresting image peaks: Once the data for all the peaks is tabulated, it can be further pruned by removing peaks that are not useful to the analysis. The following uninteresting peaks are removed from the set obtained in step 2 above:

i. **Bad time intervals:** A list of good and bad BAT science time intervals can be found in the Swift data archive. The most recent version is: /caldb/data/swift/bat/bcf/swbbadtimes20041120v005.gti. To avoid erroneous data, image peaks that occurred during a interval flagged as 'bad' are removed.

ii. **Known sources:** Image peaks located within a 12 arcmin radius of a previously identified and catalogued non-GRB source that emits hard x-ray radiation are also removed from the sample. This comparison is done once by the on-board software which assigns each known source-associated peak with a non-zero CatNum corresponding to the source identity. However, a second comparison is performed for the purpose of this analysis using a more complete source catalog provided by David Palmer [38].

iii. **Long imaging intervals:** Peaks identified within very long imaging intervals ($\gtrsim 5\,\mathrm{min}$) are removed. Such long survey intervals are known to contain large systematic errors [19] and the BAT team does not recommend their use for data analysis.

iv. **GRB events:** So as to not re-analyze triggers that were already used in the main S5 GRB search [20], image peaks that are associated with a confirmed GRB are also eliminated. These are found by comparing the image peak sample with a list of S5 GRB times and locations and flagging the matching events.

v. **GCN eliminated events:** Some events trigger a GRB response, but are later (upon follow-up observation) discovered to be caused by some other phenomenon (the most common examples are cosmic ray shower events, and South Atlantic Anomaly events discussed below).

vi. **Cosmic ray shower events:** Cosmic rays (highly energetic protons and nuclei) incident on the Earth, interact with molecules in the atmosphere and create 'showers' of lighter particles including γ-rays. When a primary cosmic ray particle hits the BAT detector, it can result in a false GRB detection. Cosmic ray shower (CRS) events can be identified by looking at the $100\,\mu$s lightcurve provided in the observation *event file* in the data archive. Figure 4.2 shows a cosmic ray shower event as seen in the lightcurve at the time of a particularly strong image peak. All of the excess counts appear to occur in the same $100\,\mu$s bin (as opposed to being spread out over time). Such a single-bin event is the mark of a CRS. A handful of peaks can be eliminated using this method. However, since no event file is produced for most of the below-threshold image peaks, this is rarely possible.
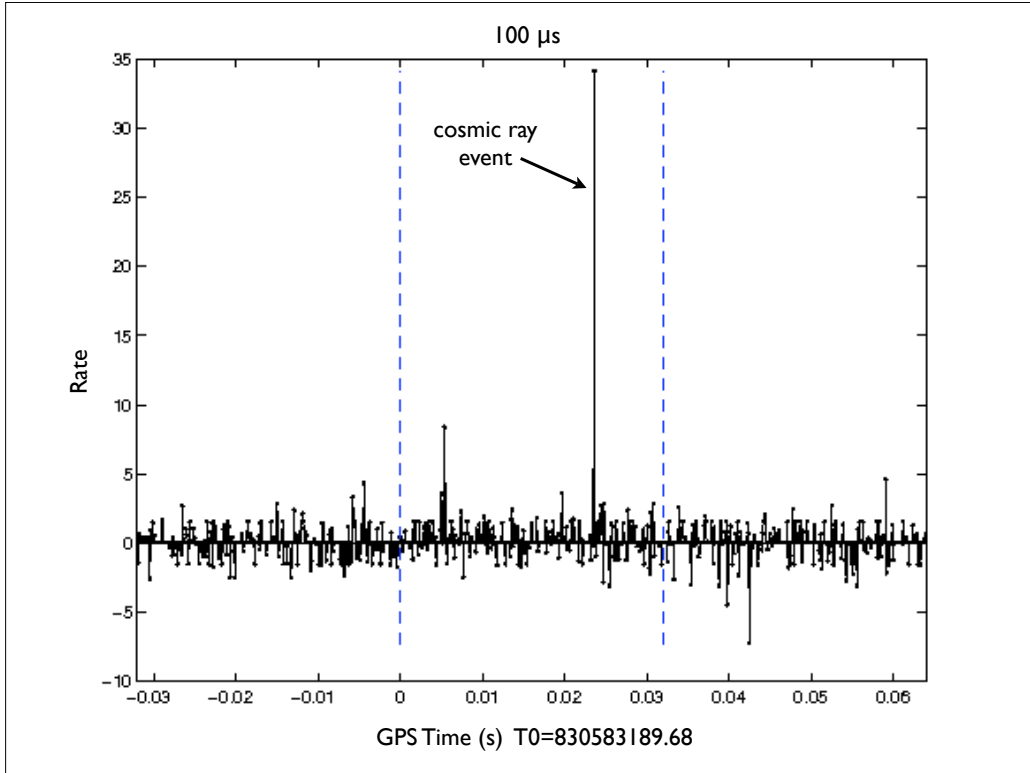
FIGURE 4.2.   A cosmic ray shower event as seen in the $100 \, \mu$s BAT-produced lightcurve during the time of an image peak.   The vertical dashed lines mark edges of the imaging interval used for finding the peak.   This particular peak has $\mathrm{SNR}_{peak} = 6.86 \, \sigma$.   Such events are *not* GRBs and are therefore removed from the trigger sample.

vii. **SAA events:** The Earth's magnetic field holds in place a torus-shaped region of highly-energetic charged particles known as the Van Allen belt. The region where this radiation comes closest to the surface of the Earth is known as the South Atlantic Anomaly (SAA). When the spacecraft passes through the SAA, the BAT event rate increases dramatically and often causes a strong rate trigger to occur even in the absence of a GRB or other source.

SAA-triggered events can be eliminated by finding the position of the spacecraft above Earth at the time of the event, and by examining the 64 ms lightcurve produced. Figure 4.3 shows the location of the spacecraft for a typical SAA-induced rate trigger. The 64 ms lightcurve from the same time interval is shown in Figure 4.4. As Swift approaches the SAA, the corresponding lightcurve shows a gradual but pronounced rising slope, indicating that the resulting image peak is most likely due to noise, and can be removed from the sample.

The final cumulative SNR distribution of the image peaks is shown in Figure 4.5. Due to the huge number of total peaks (over 30,000 total), checking for SAA events is only possible for peaks with $\text{SNR}_{peak} > 6.0\,\sigma$, and the CRS test is only possible for a handful of those for which the $100\,\mu$s lightcurves are available.[2] For this analysis, the relevant part of the distribution plot begins at $\sim 6.0\,\sigma$, because this is approximately where the new thresholds will be set. The true S5 GRB peaks are included in the distribution in order to emphasize what appears to be an overlap of two unique distributions. The noise peak distribution and the GRB peak distribution merge at the 'elbow' in the curve between 6 and $7\,\sigma$. There is no hard SNR cutoff

---

[2]SAA events in the rate trigger peaks are checked down to an SNR of $6.0\,\sigma$, but image trigger peaks are only checked down to $6.3\,\sigma$. However, because of the extremely low number of SAA events (less than 1%) in the image trigger peak sample, the shape of this plot should not be affected by this omission.
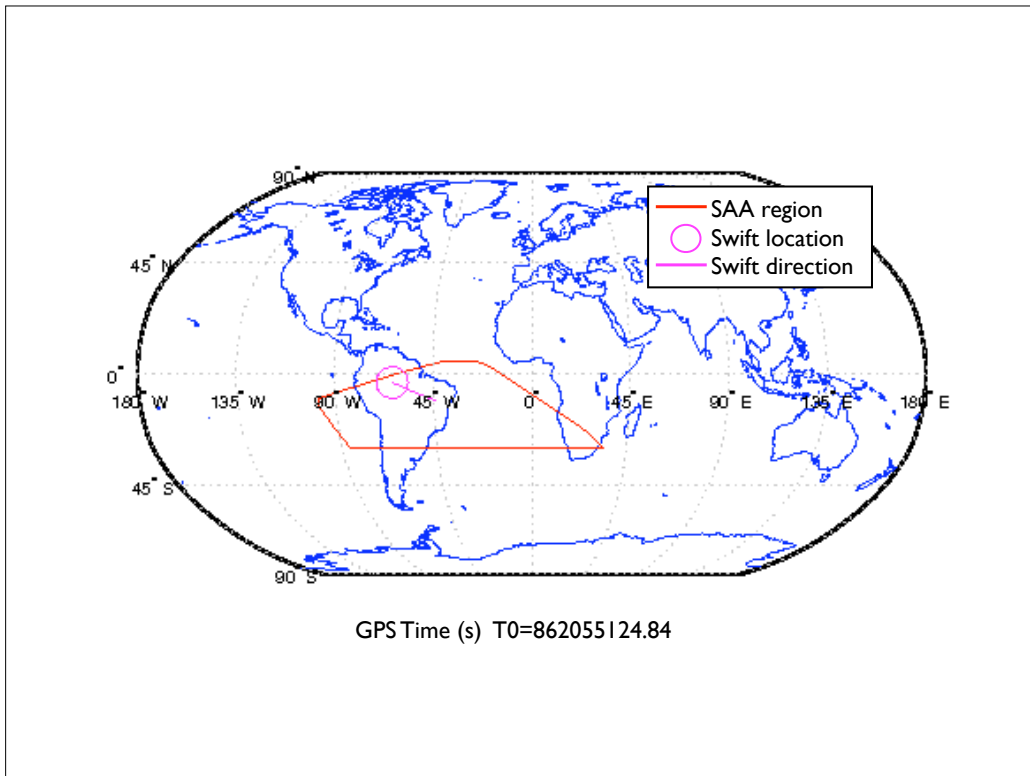
FIGURE 4.3. The Swift spacecraft entry into the South Atlantic Anomaly, a region of high background radiation. At the same time, a rate trigger and subsequent $6.68\,\sigma$ image peak is produced, which is removed from the trigger sample.
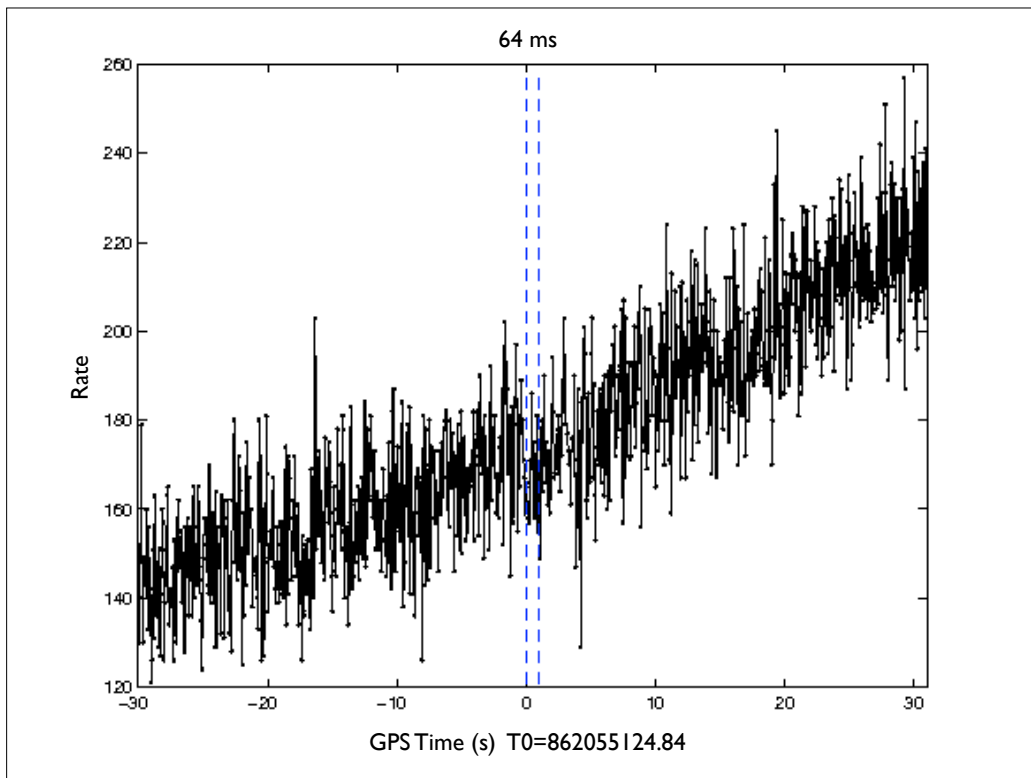
FIGURE 4.4. The 64 ms lightcurve during the Swift spacecraft entry into the South
Atlantic Anomaly as shown in Figure 4.3. The rising rate induces a (most likely) false
image peak.
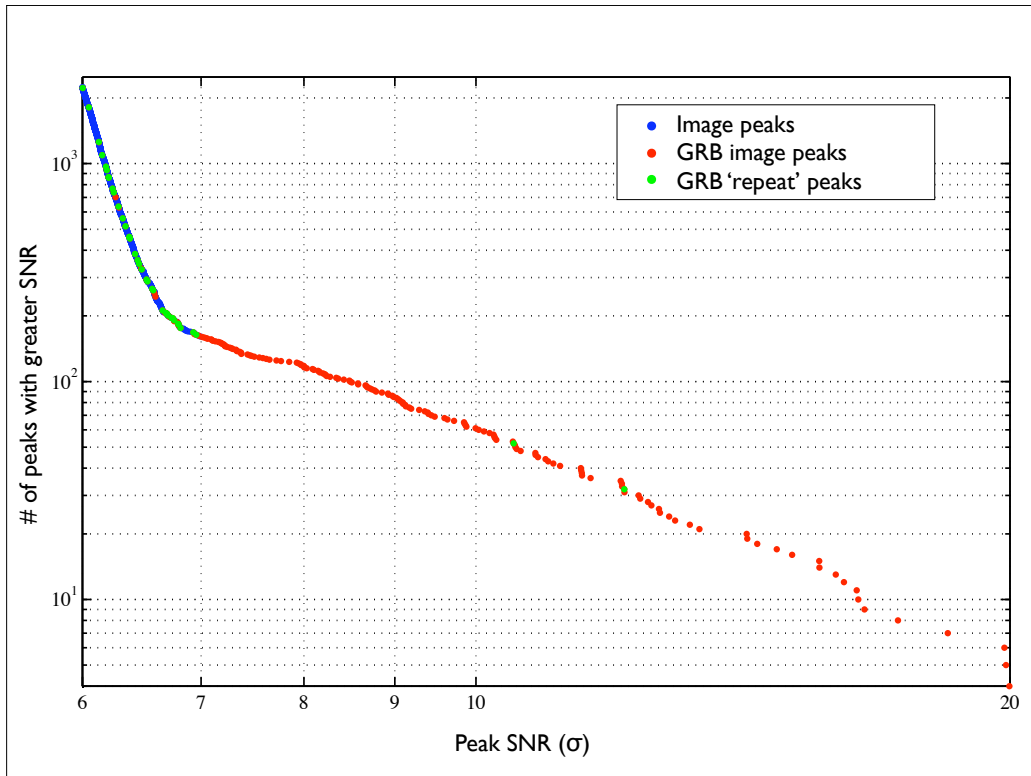
FIGURE 4.5. The cumulative distribution of BAT image peaks above $6.0\,\sigma$ during S5/VSR1. GRB-associated peaks are shown in red, and assumed non-GRB peaks are in blue. If there is more than one peak associated with a GRB ('repeat' GRB peaks), then the weaker peaks are indicated with green dots (and the strongest is in red). The GRB and noise distributions merge at elbow in the curve.

between the two distributions due in part to the complicated thresholding of the rate trigger peaks. In fact, the tail of the 'noise' distribution almost certainly contains real GRB peaks as well. Estimating *how many* real GRBs are present, is the focus of the next section.

4.2.2. Threshold Selection and Purity Estimate

Following the method used by the BAT software, it makes sense to treat rate and image trigger peaks separately and choose different lowered thresholds for each. Information about the *type* of each trigger is contained in the 'triggerIsOn' column of the image file (see Section 4.2.1). One notable difference between the two types is that image triggers use longer imaging durations (the time intervals during which the peak counts are accumulated). Figure 4.6 shows a histogram of the imaging durations for all non-GRB triggers above $6.0\,\sigma$. Although these durations do not have anything to do with actual GRB durations (T_{90} values), they will be important in defining the GW search window discussed more in Section 4.3.5.

A simple extrapolation method is used to estimate the number of GRBs in the below-threshold image peak sample for both types of triggers: *The number of GRBs in the SNR bin directly below the BAT threshold should be approximately the same as the number of GRBs in the bin right above the threshold.*

This method is implemented fairly easily in the case of the image triggers because of the strict $7.0\,\sigma$ threshold. The tail of the differential image trigger distribution is shown in Figure 4.7. The plot is essentially a magnification of the region of interest near the threshold. The 'repeat' GRB peaks have been removed from this plot, in order to give a more accurate representation of the true population. Since there are 8 GRBs in the SNR interval (7.0, 7.5), by the reasoning given above, one would expect
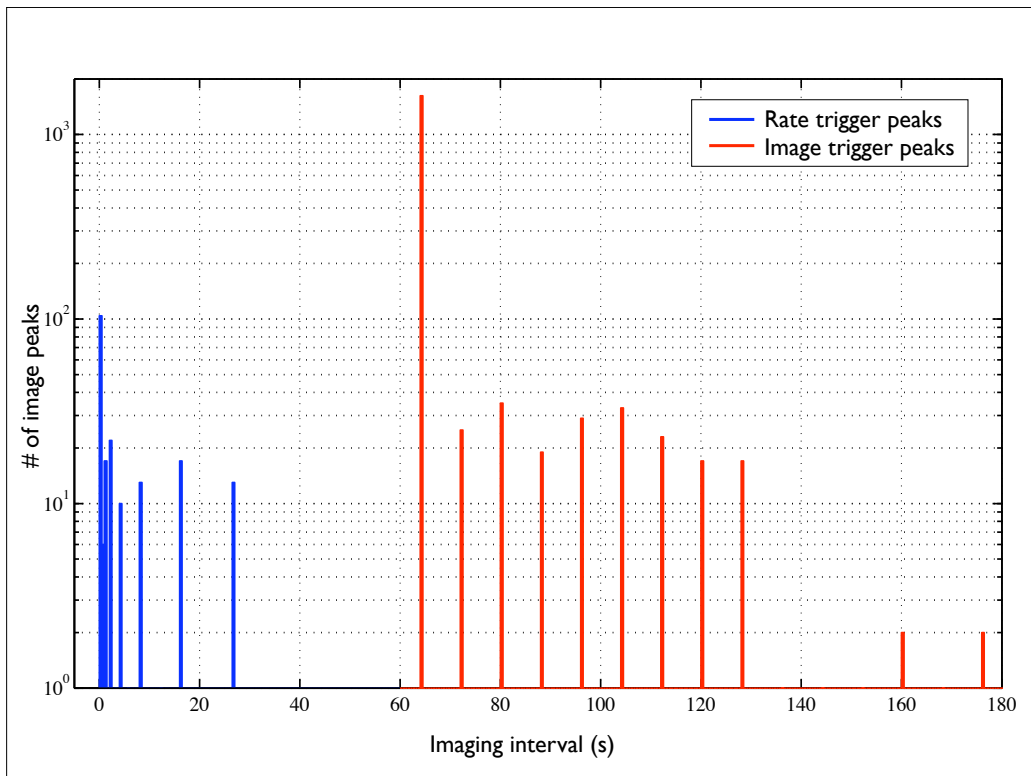
FIGURE 4.6. Histogram of imaging intervals. Rate and image triggers use different time intervals to produce image peaks. The histogram above shows the imaging durations of all non-GRB peaks above $6.0\,\sigma$. This is a fair representation of the final trigger sample distribution, which will be just a small fraction of the events shown here.
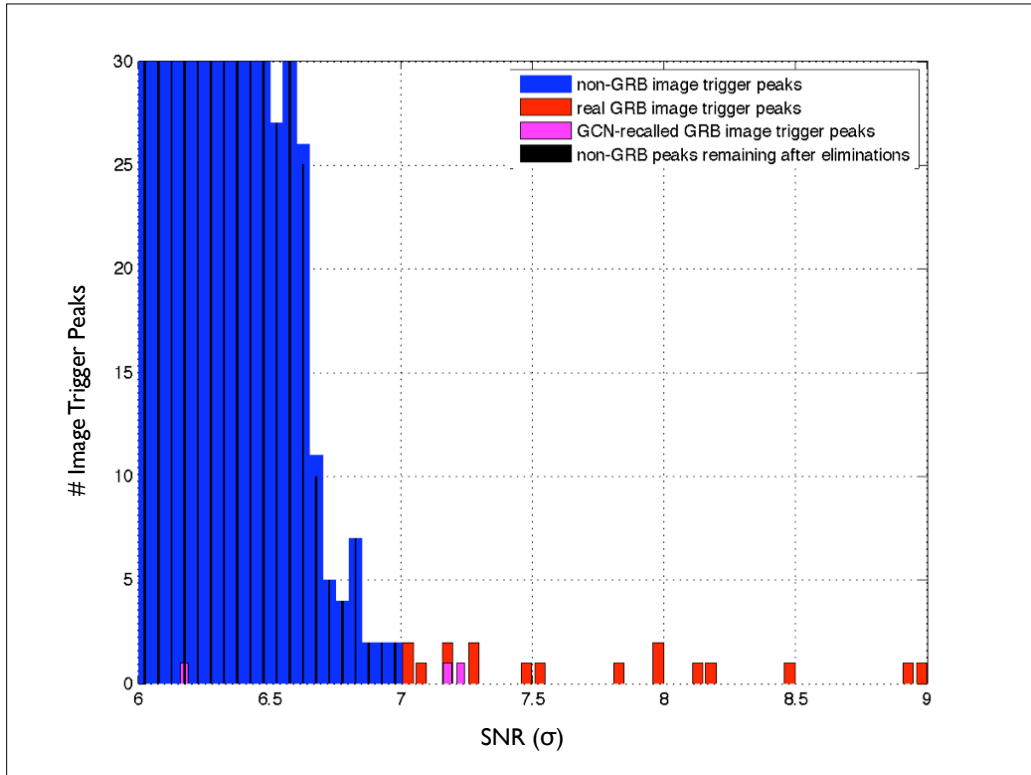
FIGURE 4.7. A histogram of the image trigger peak SNR is shown near the tail of the noise distribution. Peaks associated with a confirmed GRB are shown in red, peaks that were not followed-up by Swift ('non-GRB' peaks) are shown in blue, and peaks that were initially declared as GRBs and later revealed to be false alarms are shown in magenta. The black bars depict the number of non-GRB peaks remaining after SAA eliminations (only a few SAA events are identified in the image trigger sample).

to find the same number of GRBs in the interval (6.5, 7.0). Assuming the 8 GRBs are distributed evenly within this region, this equates to an average of 1.6 new GRBs per $0.1\,\sigma$ bin below TH_{image}. If the new image trigger threshold is $\text{TH}'_{image} < 7.0\,\sigma$, then the total number of expected new GRBs N_{image}, is given by

$$\text{N}_{image} = 16 \cdot (7.0 - \text{TH}'_{image}). \qquad (4.2)$$

And the estimated purity P_{image}, is simply

$$\text{P}_{image} = \text{N}_{image}/\text{S}_{post-SAA}, \qquad (4.3)$$

where $\text{S}_{post-SAA}$ is the number of image peaks above TH'_{image} left in the sample after the SAA eliminations (shown by the black bars in Figure 4.7).

N_{image} is actually reduced even further, however, by *network selection cuts.* Since the interferometers do not take science-quality data for the entire duration of the run, some triggers cannot be analyzed because no data are available for that time (or the data are insufficient, or flawed in some way). Approximately 2/3 of the image triggers above $6.3\,\sigma$ remain after the network selection is made, and the final expected number of real GRBs ($\text{N}_{image}^{post-net}$) should be reduced by the same fraction:

$$\text{N}_{image}^{post-net} = \text{P}_{image} \cdot \text{S}_{post-SAA}^{post-net}, \qquad (4.4)$$

where $\text{S}_{post-SAA}^{post-net}$ is the number of sample triggers that remain post SAA elimination and network selection cuts. Figure 4.8 shows a plot of both $\text{N}_{image}^{post-net}$ and $\text{S}_{post-SAA}^{post-net}$ as a function of TH'_{image}. The purity can also be extracted from this plot through Eq. 4.4.
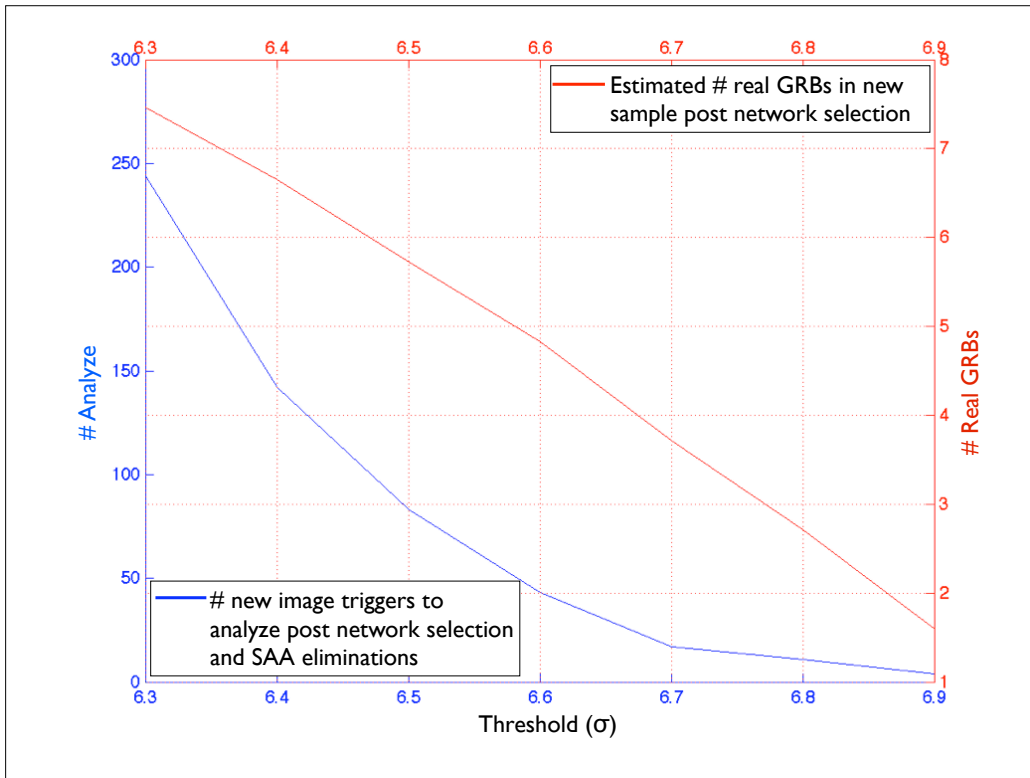
FIGURE 4.8. The estimated number of GRBs in the new image trigger sample is plotted in red as a function of threshold choice. The blue curve depicts the total number of new image triggers to analyze, also as a function of threshold, after SAA eliminations and network selection cuts.
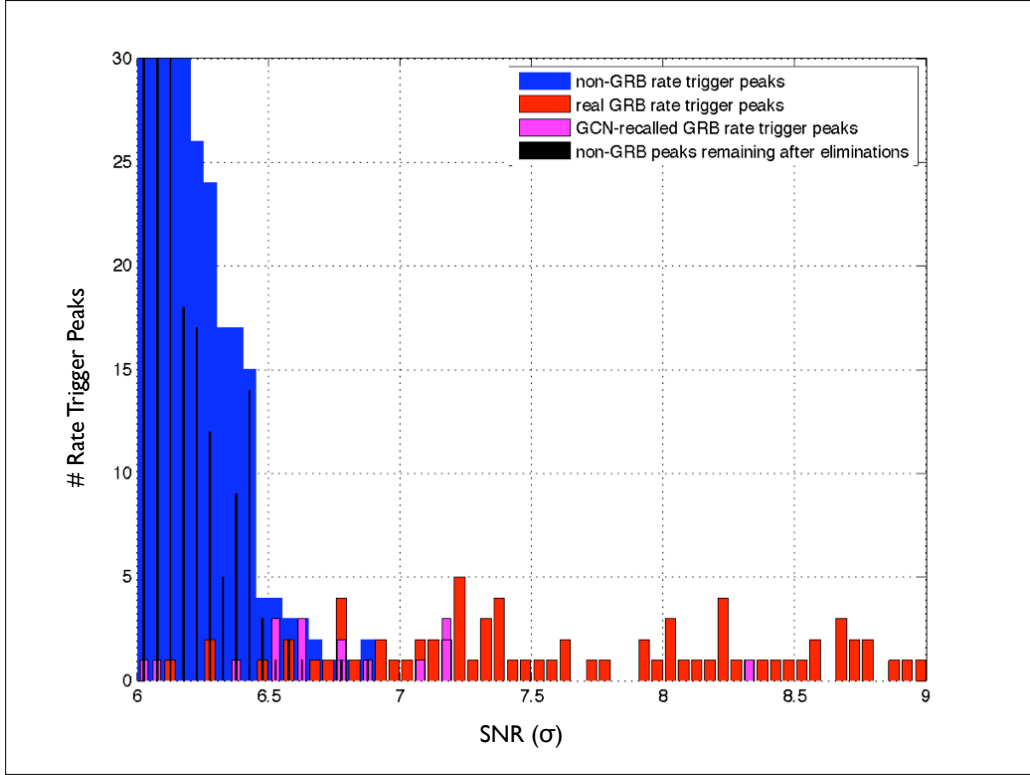
FIGURE 4.9.   A histogram of the rate trigger peak SNR is shown near the tail of the noise distribution. The main differences between this plot and Figure 4.7 (the image trigger peak histogram), are the mixing of GRB and non-GRB peaks in the $6.5 - 7.0\,\sigma$ region, and the large number of SAA-eliminated events (seen as the height difference between blue and black bars).

Estimating the purity of the rate trigger image peak sample is done in the same way with one minor change: Because the BAT uses two different thresholds, the number of real GRBs in the region *between* the thresholds ($6.5\,\sigma$ and $7.0\,\sigma$) must also be estimated. The tail of the differential rate trigger peak distribution is shown in Figure 4.9. The number of GRBs between thresholds ($\mathrm{N}_{rate}(6.5, 7.0)$) is estimated as follows:

$$\mathrm{N}_{rate}(6.5, 7.0) = \mathrm{N}_{rate}^{det}(6.5, 7.0) + f \cdot \mathrm{S}(6.5, 7.0) \tag{4.5}$$

60

where $N_{rate}^{det}(6.5, 7.0) = 12$ is the number already detected in this interval, $S(6.5, 7.0) = 16$ is the number of peaks on this interval that were *not* followed up by Swift (blue 'non-GRB' peaks in the histogram), and f represents the fraction of $S(6.5, 7.0)$ that are GRBs. After SAA eliminations, only 6 non-GRB peaks remain in the interval. That is, $S_{post-SAA}(6.5, 7.0) = 6$. Since it is not likely that *all* 6 are actually GRBs, it is reasonable to require $0 \leqslant f \leqslant 6/16 \approx 0.4$.

Then for a lowered threshold of $TH'_{rate} < 6.5$, the total expected number of real GRBs in the new rate trigger peak sample is given by

$$
\begin{aligned}
N_{rate} &= (6.5 - TH'_{rate}) \cdot (N_{rate}(6.5, 7.0) - 4)/0.5 + f \cdot S(6.5, 7.0) \\
&= (6.5 - TH'_{rate}) \cdot (12 + 16f - 4)/0.5 + 16f
\end{aligned}
\tag{4.6}
$$

where 4 is subtracted from $N_{rate}(6.5, 7.0)$ to account for the detected GRBs[3] below $6.5\,\sigma$.

The purity P_{rate}, and post-network selection GRB estimate $N_{rate}^{post-net}$, are derived following the image trigger example above (Eqs. 4.3 and 4.4). However, $N_{rate}^{post-net}$ is still a function of both TH'_{rate} and f. To display its behavior, $N_{rate}^{post-net}$ is plotted against TH'_{rate} for a range of different f values between 0 and 0.4. The final result is shown in Figure 4.10 along with the the number of new triggers as a function of threshold.

A high purity estimate (or low false alarm rate) increases the significance of any potential GW wave detections made using the trigger sample. Therefore, one would like to optimize the analysis by choosing the threshold combination (TH'_{image}, TH'_{rate})

---

[3]There are two reason that non-'repeat' GRBs exist even in the below-threshold region. The first is that for the first ∼few weeks of S5/VSR1, the BAT rate threshold TH_{low} was actually set to $6.3\,\sigma$. The second reason is that ground-based analysis of a below-threshold peak sometimes yields a stronger peak if, for example, a different selection of the data is used for the image reconstruction (see GCN circulars 4272 and 5076 corresponding to GRBs 051114 and 060505, respectively [35]).
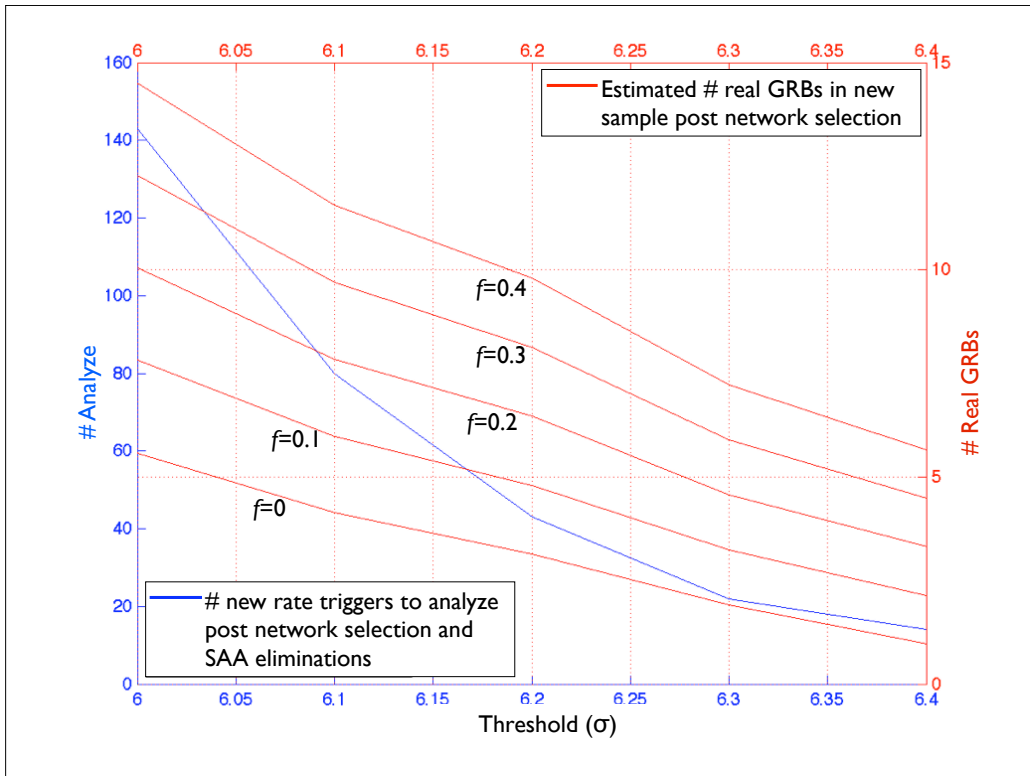
FIGURE 4.10. The estimated number of GRBs in the new rate trigger image peak sample is plotted as a function of threshold choice (red), along with the total number of new rate triggers to analyze (blue) after SAA eliminations and network selection cuts. The 4 red curves correspond to different values of f, the fraction of non-GRB peaks in $(6.5\,\sigma,\,7.0\,\sigma)$ that are estimated to be real.

that maximizes the estimated purity of the sample, but also yields a high number of GRBs. Specifically, the thresholds are chosen to maximize the purity *for a given range of total new triggers* that it is deemed reasonable to analyze[4]. In general, the purity decreases with the thresholds, and the expected GRB number increases. The naive assumption then, is that the *minimum* number of new triggers yields the *maximum* purity. However, since both quantities depend on the somewhat erratic behavior of the number of SAA events and total number of peaks in each SNR bin[5], this is not necessarily the case.

A range of 100-200 new triggers is chosen[6], along with the following selection of possible threshold values:

$$\text{TH}'_{image} = [6.3,\ 6.4,\ 6.5,\ 6.6,\ 6.7,\ 6.8,\ 6.9]$$
$$\text{TH}'_{rate} = [6.0,\ 6.1,\ 6.2,\ 6.3,\ 6.4].$$

Next, the overall purity is compared for each possible threshold combination that yields between 100 and 200 total triggers (after network selection cuts), and for each value of $f = [0,\ 0.1,\ 0.2,\ 0.4]$. The results are shown in Table 4.1.

Since all values of f produce the same optimized thresholds (TH'_{image}, TH'_{rate})=(6.6 σ, 6.1 σ), this is the obvious choice. For quoted estimates in the right-hand column of Table 4.1, $\pm 2\sigma$ errors are calculated by the propagation of Poisson $\sqrt{N}$ standard deviations which are assigned to the estimated values of N_{image} and N_{rate}.

---

[4]The computational time for this analysis is significant.

[5]For example, the estimated purity is higher in SNR bins with a high percentage of SAA events.

[6]The main GRB GW burst search on LIGO S5 and Virgo VSR1 data used 137 triggers [20].

f	Total New Triggers	Optimal Thresholds (σ) (TH'_{image}, TH'_{rate})	Estimated Purity	Estimated # GRBs
0.0	123	(6.6, 6.1)	7.3	9.0 ± 5.0
0.1	123	(6.6, 6.1)	8.8	10.8 ± 5.5
0.2	123	(6.6, 6.1)	10.3	12.7 ± 5.9
0.3	123	(6.6, 6.1)	11.8	14.5 ± 6.3
0.4	123	(6.6, 6.1)	13.3	16.4 ± 6.7

TABLE 4.1. Optimized threshold combinations and purity estimates for different values of f (fraction of rate trigger events between $6.5\,\sigma$ and $7.0\,\sigma$ not followed up by Swift that are real GRB events). Regardless of the true value of f, the threshold combination yielding the highest overall sample purity in the 100-200 new trigger range is (TH'_{image}, TH'_{rate})=($6.6\,\sigma$, $6.1\,\sigma$), for a total of 123 new triggers.

To verify that this is indeed optimized (and is not simply the threshold combination that yields the *lowest* trigger total between 100 and 200 new triggers), one can check the 100-120 triggers range, which produces a different optimal threshold combination ($6.5\,\sigma$, $6.3\,\sigma$) for a total of 105 new triggers and a slightly *lower* purity estimate than the optimized case for all possible values of f.

The final set of 123 triggers is presented in Tables A.1 (image triggers) and A.2 (rate triggers) of Appendix A. In addition to GPS time, imaging interval duration, sky-location, SNR_{peak}, and available IFO network, the tables also list the 1σ error radius corresponding to the sky locations. This is the 68% confidence region of the sky position measurement, and is calculated from SNR_{peak} as follows [39]:

$$\mathrm{ERR\_RAD}_{68\%} = \frac{7.32 \cdot (\mathrm{SNR}_{peak})^{-0.7}}{60} \ \ (\mathrm{deg}). \tag{4.7}$$

The high position accuracy ($\sim 0.03°$) of Swift BAT triggers is beneficial to this analysis. The errors are small enough that they do not need to be accounted for by creating a grid of possible source positions in the GW search (Section 4.3), which saves computational time and increases search sensitivity.

4.2.3. Nearby Galaxy Coincidence Study

Typical Swift-detected GRBs occur at distances between several hundred to several thousand Mpc [40]. However, only a relatively nearby ($\lesssim$ 50 to 100 Mpc) GRB has a chance of being detected in gravitational waves by the initial LIGO/Virgo detectors during the S5/VSR1 run. Although redshift (distance) measurements are not available for the triggers in our sample, the sky position (RA and DEC) measurements can be used to determine whether a likely host galaxy exists for the GRB. Then one might infer the GRB distance from the *known* distance of its possible host galaxy. However, a certain amount of *chance* position overlaps are expected even from a completely random distribution of sky locations. Therefore, we first wish to determine whether the number of galaxy overlaps is consistent with, or significantly more than what would be expected from a random distribution.

A catalog [41] of approximately 53,000 nearby galaxies all within $100\,\mathrm{Mpc}$ is used to compare with trigger locations from Tables A.1 and A.2. To qualify as a match, the trigger must lie within d_{min} arcmin of a galaxy center. If d is the angular distance between the trigger and galaxy center, b is the major diameter of a galaxy, ERR_b is major diameter error, and $\mathrm{ERR\_RAD}_{peak} = 3\,\mathrm{arcmin}$ is the assumed error radius of the trigger position[7], then the following condition must be met:

$$d_{min} = \mathrm{ERR\_RAD}_{peak} + (b + \mathrm{ERR}_b)/2. \tag{4.8}$$

Using this method, only 3 of the triggers in Tables A.1 and A.2 are found to overlap with the known sky position of a nearby galaxy. For each match, the trigger

---

[7]Actually, all triggers have $\mathrm{ERR\_RAD}_{68\%} < 2.1\,\mathrm{arcmin}$ and $\mathrm{ERR\_RAD}_{90\%} < 3.1\,\mathrm{arcmin}$, based on the maximum SNR_{peak} of $6.1\,\sigma$ and the BAT centroid uncertainty relation given in [39].

Peak SNR (σ)	Trigger Position (RA,DEC) (deg)	Galaxy Position (RA,DEC) (deg)	Galaxy Size $(b+\mathrm{ERR}_b)/2$ (arcmin)	d (arcmin)	Galaxy Dist. (Mpc)
6.75	$(22.936, -74.358)$	$(13.158, -72.800)$	210.85	190.05	0.06
6.42	$(246.399,\ \ 37.649)$	$(246.395,\ \ 37.637)$	0.35	0.78	72.2
6.12	$(41.501, -55.432)$	$(41.574, -55.458)$	0.62	2.91	87.2

TABLE 4.2. Triggers that overlap the sky-location of a nearby galaxy from the GWGC catalog. A 3-arcmin radius is used for trigger position errors, and galaxy radii are determined by the semi-major axis measurement. The names of the three galaxies as given by the GWGC catalog are (in order), 1) NGC0292 (Small Magellanic Cloud) 2) SDSSJ162534.81+373811.7, 3) ESO154-013. The total number of matches is consistent with the null hypothesis.

and galaxy positions are displayed in Table 4.2 along with the angular distance to the nearest galaxy, the size $((b+\mathrm{ERR}_b)/2)$ of the galaxy, and its radial distance from Earth.

Repeating this calculation for 100,000 randomly-located triggers yields 2009 galaxy matches (or 2.0%). (See Appendix B for the details.) Since 3/123 (or approximately 2%) of the possible GRB triggers are galaxy matches, we find this to be consistent with the null hypothesis that all matches are merely chance coincidence.

4.3. Coherent Network Analysis Overview: X-Pipeline

The following section will provide an overview X-Pipeline, the MATLAB-based software package used in the GW analysis. X-Pipeline is a robust and fully LVC-reviewed code, versions of which have been used in previous LIGO [42], and joint LIGO/Virgo [20], [43] gravitational wave searches. A detailed description of the pipeline is provided on the following pages, but the basic steps are summarized here:

1) **Calculate coherent energies:** Combine data from the network of interferometers around the time of the GRB trigger and calculate the *coherent energies.*

2) **Identify events:** Search for possible gravitational wave events in the data and rank them according to a *detection statistic*.

3) **Tune the analysis:** Estimate the background noise in the data and inject simulated waveforms into the data near the GRB trigger time to determine how sensitive the analysis is to real GWs in the data. Repeat this process for multiple tuning parameters and choose the parameters that give the best sensitivity results.

4) **Calculate upper limits:** Apply the final tuning parameters to the possible GW events found in the data near the trigger time. Follow-up surviving candidate events, and calculate GW amplitude upper limits in the absence of any surviving events.

The remainder of this section is broken down into five parts: 1) Coherence is discussed and the coherent energies are derived. 2) The detection statistics used for ranking events are introduced. 3) The waveforms used in the tuning process are described. 4) A tuning example is shown using real data and a set of waveform injections. 5) The final details of the analysis are filled in as the pipeline is described step-by-step.

4.3.1. Coherence

The concept of *coherently* combining data from a network of separated gravitational wave detectors is part of what makes X-Pipeline a unique and powerful tool. In this analysis, the individual sensitivity of each detector is folded into the computation of the coherent energies, which makes analysis tuning simple because separate thresholds are not needed for identifying events in each detector. The coherent energies are used for separating noise glitches from gravitational waveforms

67

in the data. Here, we derive the coherent sums [44], and describe how they are used for glitch rejection.

We begin with a gravitational wave originating from a direction $\hat{\Omega}$. If there are D detectors, each located at a different position, $\vec{r}_\alpha$ for $\alpha \in [1, ..., D]$, then the arrival time of the GW in detector α is delayed by an amount

$$\Delta t_\alpha = \frac{1}{c}(\vec{r}_0 - \vec{r}_\alpha) \cdot \hat{\Omega} \tag{4.9}$$

with respect to the arbitrary reference position $\vec{r}_0$, where we have used the fact that the gravitational wave travels at the speed of light, c. If the antenna response of detector α in the direction of $\hat{\Omega}$ is $(F_\alpha^+(\hat{\Omega}), F_\alpha^\times(\hat{\Omega}))$, then the output of the detector is given by

$$d_\alpha(t + \Delta t_\alpha(\hat{\Omega})) = F_\alpha^+(\hat{\Omega})h_+(t, \vec{r}_0) + F_\alpha^\times(\hat{\Omega})h_\times(t, \vec{r}_0) + n_\alpha(t + \Delta t_\alpha(\hat{\Omega})), \tag{4.10}$$

where $n_\alpha(t)$ is the noise in detector α at time t. In this analysis, the sky-locations of the triggers are known to a high degree of accuracy (see Section 4.1.1), and for each trigger, the data in each detector are time-shifted according to Eq. 4.9 prior to the search. Henceforth in this discussion, the time-delay will be excluded from the notation for brevity.

For the purpose of identifying events in the data, the discrete Fourier transform of the time series in each detector is computed to produce pixelated time-frequency maps of the data streams. The data are also weighted by the noise power spectral

density present in each detector. Eq. 4.10 then becomes

$$
\begin{pmatrix} d_1^w(j,k) \\ \vdots \\ d_D^w(j,k) \end{pmatrix} = \begin{pmatrix} F_1^{+w}(k) \\ \vdots \\ F_D^{+w}(k) \end{pmatrix} h_+(j,k) + \begin{pmatrix} F_1^{\times w}(k) \\ \vdots \\ F_D^{\times w}(k) \end{pmatrix} h_\times(j,k) + \begin{pmatrix} n_1^w(j,k) \\ \vdots \\ n_D^w(j,k) \end{pmatrix}, \quad (4.11)
$$

where $d_\alpha^w(j,k)$ is the noise-weighted amplitude in pixel (j,k) of the Fourier transformed output of detector α. The quantities F_α^{+w}, $F_\alpha^{\times w}$, and n_α^w are weighted by the same amount, while h_+ and $h_\times$ are of course not weighted, because the gravitational wave signal does not depend on the detector noise.

More concisely, Eq. 4.11 can be written

$$
\vec{d} = \vec{F}^+ h_+ + \vec{F}^\times h_\times + \vec{n}, \quad (4.12)
$$

by simply leaving off the pixel indices and weighting superscripts, and noting that $\vec{d}$ is a vector in the D-dimensional detector space defined by $\vec{F}^+$ and $\vec{F}^\times$.

A better basis for $\vec{d}$ can be constructed by rotating the vectors into the *dominant polarization frame*. In the DPF frame, the basis vectors are orthogonal to one another and the antenna response is maximized along the plus-polarization vector and minimized along the cross-polarization vector. After rotating the original frame through the polarization angle ψ, the new frame is given by

$$
\vec{F}^+(\psi) = \cos 2\psi \vec{F}^+ + \sin 2\psi \vec{F}^\times, \quad (4.13a)
$$

$$
\vec{F}^\times(\psi) = -\sin 2\psi \vec{F}^+ + \cos 2\psi \vec{F}^\times. \quad (4.13b)
$$

The choice of polarization angle ψ_{DP}, is the one that maximizes the quantity $|\vec{F}^+(\psi)|^2$. This yields the result

$$\psi_{DP} = \frac{1}{4} \arctan \left(\frac{2\vec{F}^\times \cdot \vec{F}^+}{|\vec{F}^+|^2 - |\vec{F}^\times|^2} \right). \tag{4.14}$$

The new basis vectors are denoted by the lower-case symbols

$$\vec{f}^+ = \vec{F}^+(\psi_{DP}) = \cos 2\psi_{DP} \vec{F}^+ + \sin 2\psi_{DP} \vec{F}^\times, \tag{4.15a}$$

$$\vec{f}^\times = \vec{F}^\times(\psi_{DP}) = -\sin 2\psi_{DP} \vec{F}^+ + \cos 2\psi_{DP} \vec{F}^\times, \tag{4.15b}$$

which are then normalized to form unit vectors $\hat{e}^+$ and $\hat{e}^\times$ that define the new basis:

$$\hat{e}^+ = \frac{\vec{f}^+}{|\vec{f}^+|}, \tag{4.16a}$$

$$\hat{e}^\times = \frac{\vec{f}^\times}{|\vec{f}^\times|}. \tag{4.16b}$$

Using the new basis vectors, one can calculate several different quantities formed by projections of the data. These so-called coherent energies[8] have properties that prove useful in discerning between noise glitches and GW signals in the data [44], [45]. We begin with the plus- and cross-energies which are given by the projection of the data vector $\vec{d}$ from Eq. 4.10 onto $\hat{e}^+$ and $\hat{e}^\times$. Thus, for a single time-frequency pixel, the energies are

$$E_+ = |\hat{e}^+ \cdot \vec{d}|^2, \tag{4.17a}$$

$$E_\times = |\hat{e}^\times \cdot \vec{d}|^2. \tag{4.17b}$$

---

[8]Although we use the term *energy*, these quantities have units of squared strain h, and therefore do not represent *physical* energies in the normal sense.

The corresponding *incoherent* energies (I_+ and $I_\times$) can also be constructed by simply leaving out the cross-correlation terms:

$$I_+ = \sum_\alpha |e_\alpha^+ d_\alpha|^2, \tag{4.18a}$$

$$I_\times = \sum_\alpha |e_\alpha^\times d_\alpha|^2. \tag{4.18b}$$

Noise in the data is not found to be correlated between the detectors. Therefore, for a noise glitch, the cross-correlation terms (e.g. $e_\alpha^+ d_\alpha e_\beta^+ d_\beta$) will be small compared to the auto-correlation terms (e.g. $(e_\alpha^+ d_\alpha)^2$), making the coherent and incoherent parts of the energy approximately equal ($E \simeq I$). It is only for a gravitational wave signal that the following inequalities will hold:

$$
\begin{aligned}
E_+ > I_+ \quad &\& \quad E_\times < I_\times \quad \text{(for predominantly } h_+ \text{ GW)} \\
E_+ < I_+ \quad &\& \quad E_\times > I_\times \quad \text{(for predominantly } h_\times \text{ GW)}
\end{aligned}
\tag{4.19}
$$

Another energy can be formed by the projection of the data onto the so-called *null space* which is orthogonal to the space spanned by $(\hat{e}^+, \hat{e}^\times)$. This is appropriately named the null energy. For the case of 3 non-aligned detectors, the coherent and incoherent parts are given by

$$E_n = |\hat{e}^n \cdot \vec{d}|^2 \tag{4.20a}$$

$$I_n = \sum_\alpha |e_\alpha^n d_\alpha|^2. \tag{4.20b}$$

where $\hat{e}^n = \hat{e}^+ \times \hat{e}^\times$ is the null unit vector. Unlike the other coherent energies described here, the *null* energy will be smaller for GW signals than it will be for noise glitches. Therefore, glitches for which E_n/I_n is sufficiently large can be discarded as noise.

71

The only time that the null stream is not available is when there is only data from 2 detectors available and those detectors are not aligned (see reference [45] for a full discussion). In this case (an H1L1 trigger for example) other energy projections can still be used for glitch rejection criteria (such as E_{circ} discussed below).

The final energy stream to be introduced here is the circular energy E_{circ}, which is based on the assumption of circular polarization of the GW signal. The unit vectors spanning the circular space are the right and left polarized $\hat{e}^{\circlearrowright}$ and $\hat{e}^{\circlearrowleft}$, constructed as follows:

$$\hat{e}^{\circlearrowright} = \frac{\vec{f}^{\circlearrowright}}{|\vec{f}^{\circlearrowright}|} \quad \text{and} \quad \hat{e}^{\circlearrowleft} = \frac{\vec{f}^{\circlearrowleft}}{|\vec{f}^{\circlearrowleft}|}, \tag{4.21}$$

where

$$\vec{f}^{\circlearrowright} = \vec{f}^{+} + i\vec{f}^{\times} \quad \text{and} \quad \vec{f}^{\circlearrowleft} = \vec{f}^{+} - i\vec{f}^{\times}. \tag{4.22}$$

The circular null unit vectors are given analogously by:

$$\hat{e}^{n\circlearrowright} = \frac{\vec{f}^{n\circlearrowright}}{|\vec{f}^{n\circlearrowright}|} \quad \text{and} \quad \hat{e}^{n\circlearrowleft} = \frac{\vec{f}^{n\circlearrowleft}}{|\vec{f}^{n\circlearrowleft}|}, \tag{4.23}$$

where

$$\vec{f}^{n\circlearrowright} = \vec{f}^{+} - i\vec{f}^{\times} \quad \text{and} \quad \vec{f}^{n\circlearrowleft} = \vec{f}^{+} + i\vec{f}^{\times}. \tag{4.24}$$

Finally, we have E_{circ} and $E_{n,circ}$ which are determined by taking the maximum and minimum of their respective projections as follows [18]:

$$\begin{aligned} E_{circ} &= \max(E_{\circlearrowleft}, E_{\circlearrowright}) & = \max(|\hat{e}^{\circlearrowright} \cdot \vec{d}|^2, |\hat{e}^{\circlearrowleft} \cdot \vec{d}|^2) \\ E_{n,circ} &= \min(E_{n\circlearrowleft}, E_{n\circlearrowright}) & = \min(|\hat{e}^{n\circlearrowleft} \cdot \vec{d}|^2, |\hat{e}^{n\circlearrowright} \cdot \vec{d}|^2). \end{aligned} \tag{4.25}$$

Analogous to the cases discussed above (E_+, $E_\times$ and E_n), for a real circularly polarized gravitational wave signal one would expect:

$$E_{circ} > I_{circ} \tag{4.26a}$$

$$E_{n,circ} < I_{n,circ}. \tag{4.26b}$$

Thus, for all energies the quantity $|E - I|$ which contains cross-correlation terms only, is greater for GW transient signals than for noise transients, a fact that can be exploited to separate noise from signal and, in effect, create a pass/fail test for possible GW events found in the data. The test used in this analysis is discussed in more detail in reference [18], but can be summarized as follows: The two parameters used for tuning the veto cut are r and α. For a particular combination choice (r,α), an event is *vetoed* (i.e. removed from the data) if it does not meet the criteria

$$r < \frac{I - E}{(E + I)^\alpha} \quad \text{(for \textit{null} energies),} \tag{4.27a}$$

$$r < \frac{E - I}{(E + I)^\alpha} \quad \text{(for \textit{non-null} energies).} \tag{4.27b}$$

Here, the choice of energy used (circular, null, plus, cross, etc.) is left ambiguous intentionally. The test is done for different coherent/incoherent energy pairs depending on which detectors and how many have data for that particular GRB trigger. All of the possible network combinations but H1H2 use the pairs (E_{circ}, I_{circ}), ($E_{n,circ}$, $I_{n,circ}$) and (E_n, I_n). However, as noted above, 2 non-aligned detector networks do not use E_n. H1H2 network cuts are done using the pairs (E_+, I_+) and (E_n, I_n). (Because H1 and H2 are aligned, $E_\times$ is always zero and $E_{circ} = E_+$.) During the tuning process, the value of α is fixed (see Section 4.3.5) and the optimal value

of r (the one that maximizes the analysis sensitivity) is found automatically by the pipeline.

The choice to use the circular polarization assumption whenever possible is valid because of the types of signals being targeted in this search. The GRB progenitor models capable of producing GWs strong enough to be observed by LIGO/Virgo S5/VSR1 detectors are those that predict circularly polarized GW emission. The amplitude of the waves peak along the rotational axis of the system, but when viewed off-axis, even from a large angle, the ratio of the h_+ and $h_\times$ amplitudes of the observed GW is not greatly affected. Was(2011) [18] observes that at an inclination angle of $60°$, the amplitude ratio is still $A_+/A_\times(i = 60°) = 0.8$ (as opposed to $A_+/A_\times(i = 0°) = 1$ for perfect circular polarization), and within the typical $\sim 20\%$ amplitude calibration errors of GW detectors.

4.3.2. Detection Statistics

The process of identifying events in the data stream is described in Section 4.3.5. Here we introduce the detection statistics that are used to rank time-frequency pixels in the Fourier-transformed data. This ranking system will be used to determine how strong a glitch is in the data and it will play a key role in almost every aspect of the analysis, from background estimation and glitch rejection, to GW signal detection and upper limit estimation. For a full derivation of the statistics and their properties, see [45], [18], [46].

X-Pipeline is capable of calculating several different types of detection statistics, but for the purposes of this analysis, only two are used. The best statistic is the one that results in the best analysis sensitivity, and is chosen by the pipeline during the tuning process. The first statistic is the *log-likelihood* which assumes Gaussian

distributions of both noise and GW signal amplitudes. The shape of a Gaussian amplitude distribution (with characteristic amplitude A_c) is given by

$$p(A) = \frac{1}{A_c\sqrt{2\pi}}\exp[-A^2/(2A_c^2)].\tag{4.28}$$

Given h_+ and $h_\times$ characteristic amplitudes $A_c^+ = \sigma_h|\vec{f}^+|$ and $A_c^\times = \sigma_h|\vec{f}^\times|$, the per-pixel log-likelihood for data $\vec{d}$ is

$$L(\vec{d}|\sigma_h) = \frac{|\hat{e}^+ \cdot \vec{d}|^2}{1 + 1/(\sigma_h|\vec{f}^+|)^2} + \frac{|\hat{e}^\times \cdot \vec{d}|^2}{1 + 1/(\sigma_h|\vec{f}^\times|)^2} - \log(1 + \sigma_h^2|\vec{f}^+|^2) - \log(1 + \sigma_h^2|\vec{f}^\times|^2).\tag{4.29}$$

Using the Bayesian methodology of marginalizing over the unknown parameter σ_h yields the marginalized log-likelihood

$$L(\vec{d}|A) = 2\log\left\{\sum_{\sigma_h \in A}\frac{\exp[\frac{1}{2}L(\vec{d}|\sigma_h)]}{|A|}\right\},\tag{4.30}$$

where A is a discrete set of plausible characteristic amplitudes.

The second detection statistic used in this analysis assumes a *power-law* shape in the tail of the noise distribution, and is marginalized with a *flat* signal amplitude distribution (rather than Gaussian). The resulting statistic will not be shown here, as it is cumbersome and depends on the size of the detector network. However, its main advantage over the Gaussian log-likelihood statistic is that it is much less sensitive to glitches that do not appear in *all* of the detectors. Therefore, a noise glitch present in only one detector will contribute significantly less to the power-law statistic than to the log-likelihood statistic.

4.3.3. Waveform Injections

As stated above, part of the analysis tuning process requires making an estimate of how sensitive it is to actual gravitational waveforms present in the data. This is accomplished by first estimating the background noise in the data using so-called 'off-souce' time intervals that are sufficiently far from the GRB trigger to minimize the risk of contamination by a real GW. The second part involves producing simulated gravitational waveforms which are injected into data stream around the time of the GRB trigger (the 'on-source' time) and determining how efficiently the injections are detected by the analysis.

For this purpose, waveforms are chosen to reflect as closely as possible the GW one would expect to see in the case of a GRB, while remaining general enough to be inclusive of the majority of expected signals. As noted in Section 2.3, current favored predictions for GRB progenitors are compact binary coalescence, and stellar collapse. The two fundamentally different waveform types used by this analysis to model these phenomena are described in more detail below.

4.3.3.1. Compact Binary Coalescence Waveforms

The basic shape of the gravitational waveforms radiated by two point masses orbiting one another is well understood. Eq. 1.43 gave h_+ and $h_\times$ GW amplitudes for this system, which we recall here, remembering that R is the orbital radius, r is the distance to the object, i is the inclination angle, and μ is the reduced mass:

$$\begin{pmatrix} h_+(t) \\ h_\times(t) \end{pmatrix} = -\frac{G}{rc^4}\frac{\mu}{2}R^2\omega_{GW}^2 \begin{pmatrix} (1+\cos^2 i)\cos(\omega_{GW}t_{ret}) \\ 2\cos i \sin(\omega_{GW}t_{ret}). \end{pmatrix}, \qquad (4.31)$$

In actuality, the binary system will lose energy through gravitational radiation causing the orbit and orbital period to shrink, while the amplitude increases. The zeroth order approximation for the time evolution of the angular frequency is [47]

$$\omega_{GW}(t) = \frac{1}{4}\left(\frac{G^{5/3}}{5c^5}\mathcal{M}_c^{5/3}(t_c - t)\right)^{3/8}, \tag{4.32}$$

where t_c, or the *time of coalescence*, is the time at which the objects merge, and $\mathcal{M}_c = \mu^{3/5}(m_1 + m_2)^{2/5}$ is the so-called *chirp mass* of the system. The waveform created by a binary system *radiating gravitational energy* at any time t before the coalescence time, can be expressed in terms of $\omega_{GW}(t)$ and $\mathcal{M}_c$ as

$$\begin{pmatrix} h_+(t) \\ h_\times(t) \end{pmatrix} = -\frac{G}{rc^4}2\mathcal{M}_c^{5/3}\left(\frac{G\omega_{GW}(t)}{2}\right)^{2/3}\begin{pmatrix} (1 + \cos^2 i)\cos(\int^t \omega_{GW}(t')dt') \\ 2\cos i \sin(\int^t \omega_{GW}(t')dt') \end{pmatrix}. \tag{4.33}$$

X-Pipeline actually produces so-called *second order restricted post-Newtonian* waveforms, which use the more accurate (expanded to higher order) angular frequency evolution equation given by [48]:

$$\begin{aligned} \omega_{GW}(\Theta) = \frac{c^3}{4GM}&\left(\Theta^{-3/8} + \left(\frac{743}{2688} + \frac{11}{32}\frac{\mu}{M}\right)\Theta^{-5/8}\right. \\ &\left. -\frac{3\pi}{10}\Theta^{-3/4}\left(\frac{1855099}{14450688} + \frac{56975}{258048}\frac{\mu}{M} + \frac{371}{2048}\frac{\mu^2}{M^2}\right)\Theta^{-7/8}\right), \end{aligned} \tag{4.34}$$

where

$$\Theta = \frac{c^3\mu}{5GM^2}(t_c - t), \tag{4.35}$$

and $M = m_1 + m_2$.

For the purposes of a burst-type search such as this one, the approximation given in Eqs. 4.33 through 4.35 sufficiently models the waveform shape of an inspiral
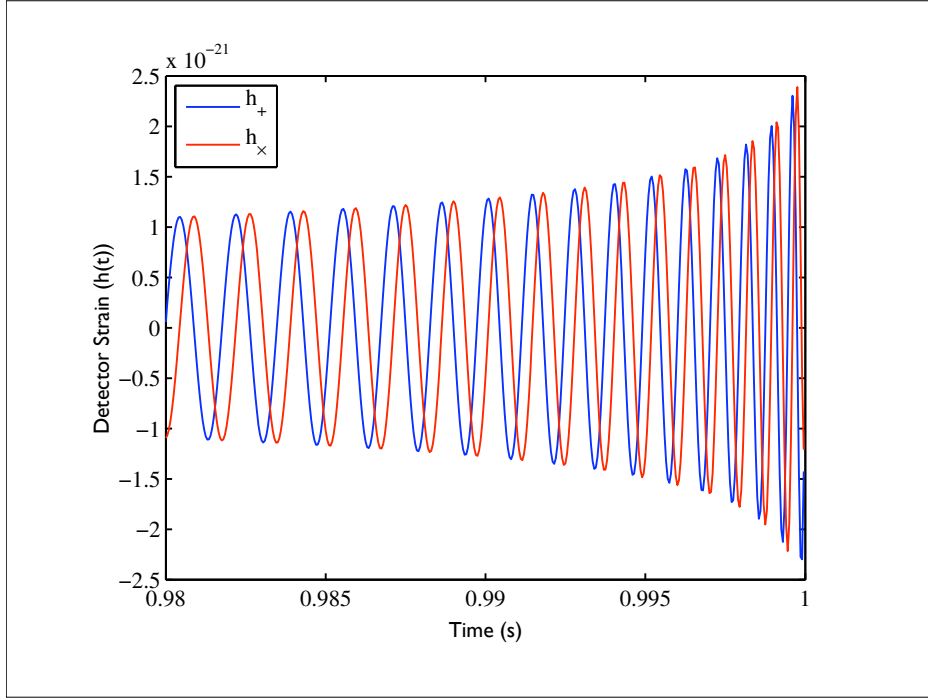
FIGURE 4.11.   The final $20\,\mathrm{ms}$ of a simulated inspiral waveform as seen by the detector. This waveform is modeled after a binary neutron star coalescence with the following parameters: $m_1 = m_2 = 1.4\,M_\odot$, $r = 10\,\mathrm{Mpc}$, and $i = 10°$.

event. Each waveform can be uniquely determined by the following four parameters: distance r, inclination i, and the masses m_1 and m_2. An example of an equal-mass $(m_1 = m_2 = 1.4\,M_\odot)$ inspiral at a distance of $r = 10\,\mathrm{Mpc}$ is plotted in Figure 4.11.

A total of 4 inspiral waveform families were chosen for this analysis. The specific parameters characterizing each family are summarized in Table 4.3. The first two entries in the table represent waveforms produced by double neutron star coalescence (NSNS), in which both objects have similar mass. The next two represent neutron star - black hole coalescence (NSBH), where the mass of one object (BH) is significantly larger than the other (NS).

Name	r (Mpc)	i (deg) (min,max)	Mass Parameters ($M_\odot$)							
			mean		Std. Dev.		Lower		Upper	
			m_1	m_2	m_1	m_2	m_1	m_2	m_1	m_2
NSNS I	10	(0,30)	1.4	1.4	0.2	0.2	0.9	0.9	3.0	3.0
NSNS II	10	(0,90)	1.4	1.4	0.2	0.2	0.9	0.9	3.0	3.0
NSBH I	20	(0,30)	1.4	10	0.4	6.0	0.9	2.0	3.0	25
NSBH II	20	(0,90)	1.4	10	0.4	6.0	0.9	2.0	3.0	25

TABLE 4.3. Inspiral waveform injection parameters used for determining analysis sensitivity. The maximum inclination i in column 3 reflects the expected opening angle of a GRB. An observer outside of this range would likely not see any γ-rays. The (0,90) range is included to account for the uncertainties discussed in Section 2.7.

Since each waveform family is actually used for hundreds of injections, the parameters are varied. Masses are Gaussian distributed with mean, standard deviation and upper and lower bounds given in the table. Inclination is distributed evenly over the specified range. Although the nominal amplitude is constant (r is not varied) the injections are assigned an overall scaling factor A, and repeated at different amplitudes (see Section 4.3.5).

It is worth noting that NSNS II and NSBH II are essentially identical to the other two waveform families in the table, with the exception of the inclination range. The wider range $(0, 90)$ is included to allow for the possibility of off-axis viewed GRBs as hypothesized for the low-luminosity events (see Section 2.7).

4.3.3.2. Stellar Collapse Waveforms

In the case of a GRB produced by stellar core collapse, the resulting gravitational waveforms are not known. Rather than using complex simulated waveforms which can vary widely depending on the specific parameters and assumptions of the model, more general elliptically polarized sine-Gaussian waveforms are used for X-Pipeline injections. These represent the dominant mode of the most likely observed

79
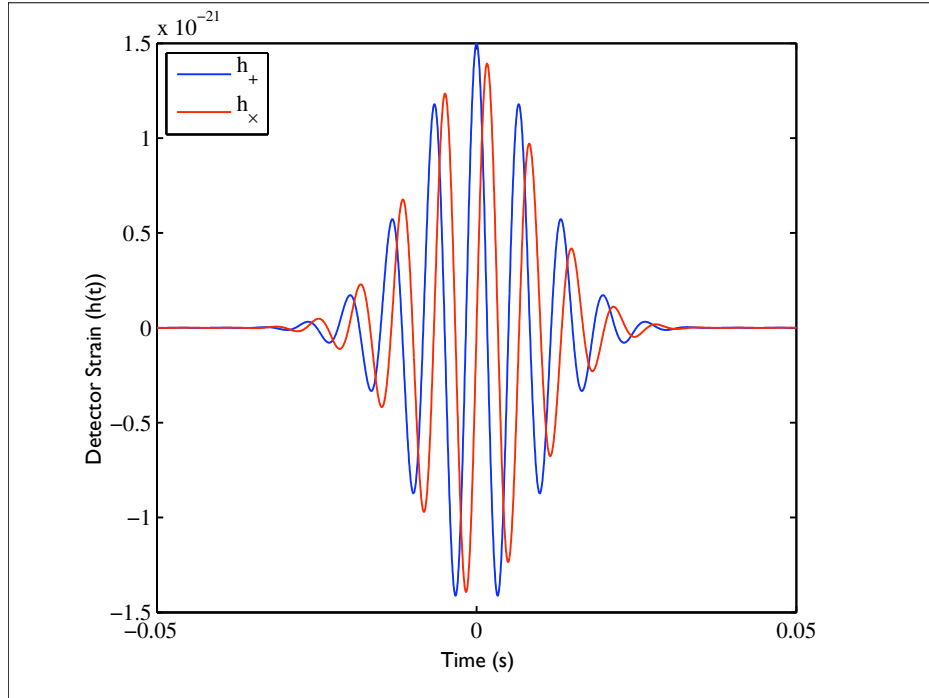
FIGURE 4.12. An elliptical sine-Gaussian waveform with central frequency $f_0 = 150\,\text{Hz}$, inclination angle $i = 45°$, envelope peak time $t_0 = 0$, and amplitude scaling factor $A_0 = 10^{-21}$.

gravitational radiation from a core collapse which, for our purposes, can be simply modeled as a rigidly rotating quadrupolar mass distribution with a slowly evolving (compared to the rotational frequency) quadrupolar mass moment. Observed at an inclination i, the waveforms are given by

$$\begin{pmatrix} h_+(t + t_0) \\ h_\times(t + t_0) \end{pmatrix} = A_0 \exp\left(-\frac{(2\pi f_0 t)^2}{2Q^2}\right) \begin{pmatrix} (1 + \cos^2 i)\cos(2\pi f_0 t) \\ 2\cos i \sin(2\pi f_0 t) \end{pmatrix}, \qquad (4.36)$$

where f_0 is the central frequency, t_0 is the peak time of the Gaussian envelope, and $Q = 9$. An example of an elliptical sine-Gaussian waveform with $f_0 = 150\,\text{Hz}$, $i = 45°$, and $A_0 = 10^{-21}$ is shown in Figure 4.12.

Type	f_0 (Hz)	i (deg)
SG I	150	(0,5)
SG II	300	(0,5)
SG III	150	(0,90)
SG IV	300	(0,90)

TABLE 4.4. Elliptical sine-Gaussian waveform injection parameters used for determining analysis sensitivity.

A total of 4 elliptical sine-Gaussian waveform families are used as injections in this analysis. The parameters chosen for each are summarized in Table 4.4. The set of central frequencies is $f_0 = [150, 300]$ Hz, and A_0 is determined such that

$$h_{rss} = \sqrt{\int \left(h_+^2(t) + h_\times^2(t) \right) dt} = 2.5 \times 10^{-21} \, \text{Hz}^{-1/2}. \tag{4.37}$$

for $i = 0$.

To form the hundreds of injections needed by the pipeline, i is evenly distributed within the given range, and t_0 is distributed evenly within the on-source window. As in the case of the inspiral waveform set, SG III and SG IV are repeats of the other two waveform families, with the exception of a wider inclination range to allow for off-axis GRB viewing.

In addition to creating a distribution of the parameter space that defines each waveform family, X-Pipeline randomly distributes the sky-location (right ascension and declination) of the injections and takes into account the calibration errors of the detectors by jittering the time and amplitude of the waveform in each detector individually.

The end result of the pipeline sensitivity analysis is a detection efficiency curve from which one can determine the h_{rss} amplitude at which the analysis can detect injected gravitational waves at a given efficiency level. In order to calculate the

81

efficiency curve, the injections must be repeated at several different amplitudes. All 8 waveform families described above use the following injection scales:

$$A/A_0 = [0.001,\ 0.0316,\ 0.0442,\ 0.0619,\ 0.0866,\ 0.121,\ 0.169,\ 0.237,\ 0.332,\ 0.464,$$
$$0.649,\ 0.909,\ 1.271,\ 1.778,\ 2.488,\ 3.481,\ 4.870,\ 6.813,\ 9.532,\ 13.335,\ 18.657,$$
$$26.102,\ 36.517,\ 51.090,\ 71.477,\ 100.00],$$

where A_0 is the nominal waveform amplitude. Scaling the h_+ and $h_\times$ polarizations effectively scales the h_{rss} amplitude of the entire waveform by the same factor, as shown in Eq. 4.37.

4.3.4. Waveform Injection and Tuning Example

In this section we combine the concepts of waveform injections and coherent veto tests described above and show an example of how noise and simulated GW glitches are separated. Figures 4.13 and 4.14 show a collection of recovered GW injections and background (i.e. noise) glitches for one segment of data and one waveform family. In both plots, the coherent and incoherent energies of the events are plotted against one another, and the color scale indicates the strength (measured by the detection statistic) of the glitch. The energy pairs plotted are E_{circ} vs. I_{circ} (Figure 4.13), and $E_{n,circ}$ vs. $I_{n,circ}$ (Figure 4.14). The shape of the veto function (the dashed magenta line given in Eqs. 4.27a and 4.27b) is tuned by the analysis to separate the injections from the noise as efficiently as possible.
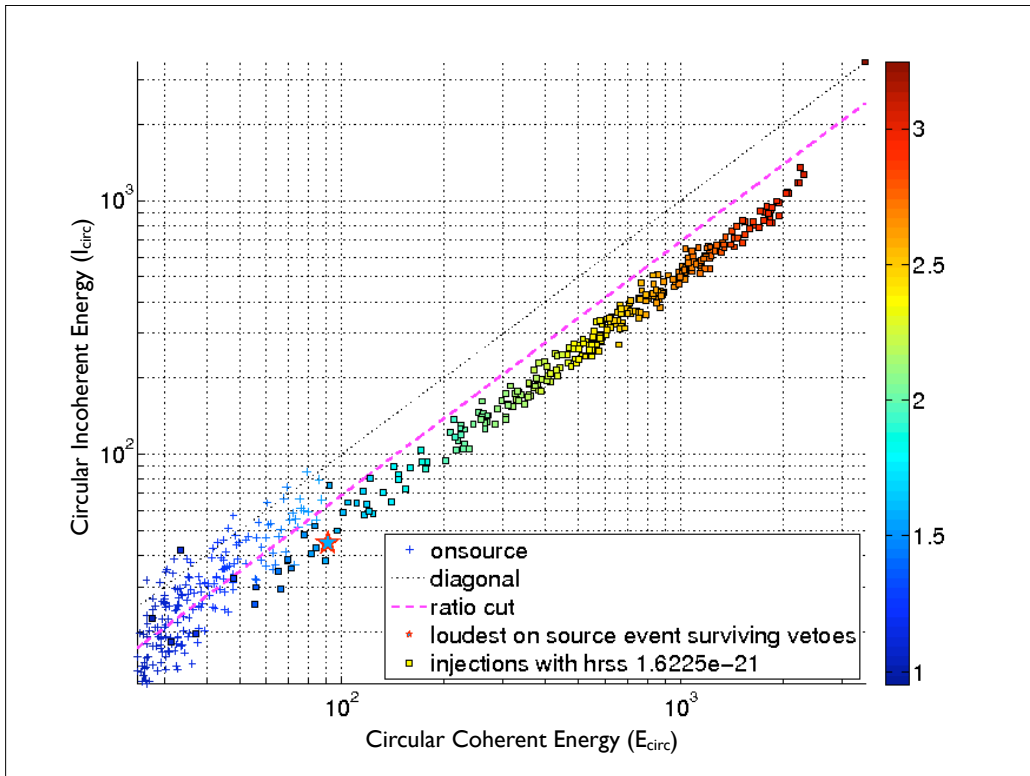
FIGURE 4.13. Circular energy veto. The coherent and incoherent parts of the circular energy are plotted against one another for both recovered injections and background events. The shape of the ratio cut is tuned to efficiently separate the background from the signal. Events above the line can be 'vetoed' as they are most likely noise.
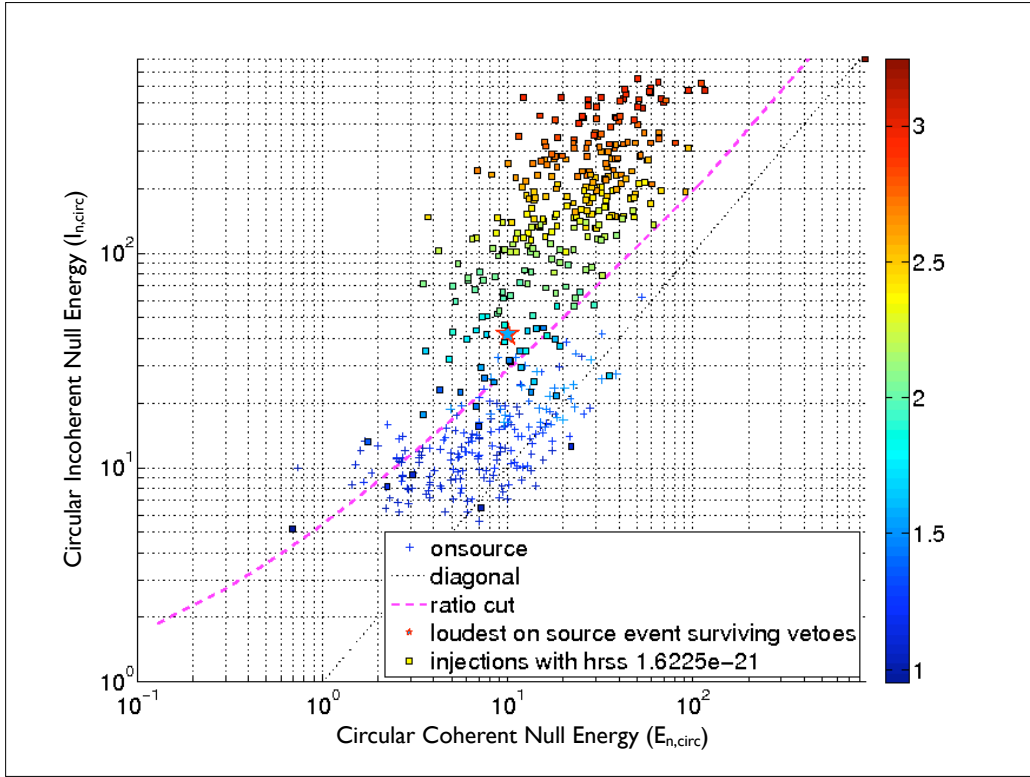
FIGURE 4.14. Circular null energy veto. The coherent and incoherent parts of the circular null energy are plotted against one another for both recovered injections and background events. As in Figure 4.13, the shape of the ratio cut is tuned to efficiently veto noise glitches. However this time it is the events *below* the line that are excluded (because the cut is made on *null* energy quantities).

Figure 4.15 shows the *detection efficiency curve* for the same set of injections and background glitches (detection efficiencies and amplitude upper limits are discussed more in Section 4.3.5). The curve summarizes the success of the tuning procedure. For example, the solid red point at $h_{rss} \approx 1.6 \times 10^{-21}\,\mathrm{Hz}^{-1/2}$ indicates that 90% of recovered injections (GWs) made at this amplitude are detected with a larger detection statistic than the loudest background glitch in this data segment that survived the veto cuts.
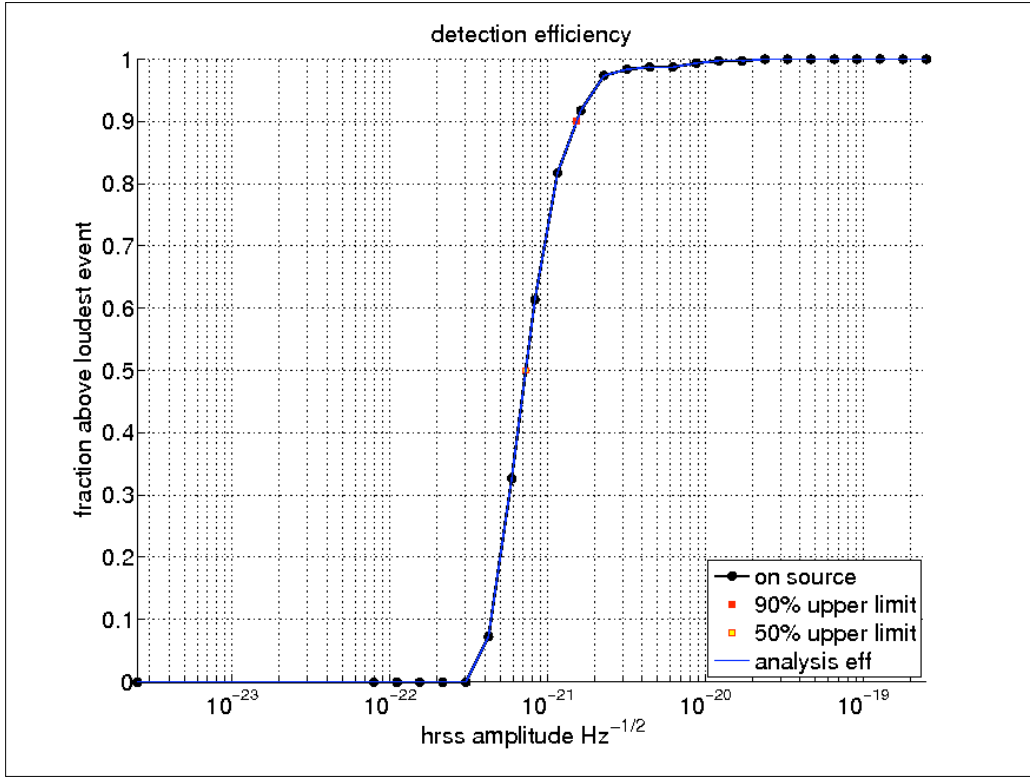
FIGURE 4.15. Detection efficiency curve corresponding to the veto cuts shown in Figures 4.13 and 4.14 above. The detection efficiency is the fraction of injections with a given amplitude that were recovered with a statistic larger than the loudest noise glitch in the data segment.

4.3.5. Analysis Pipeline Walkthrough

The basic steps of the analysis are outlined below along with some additional details about the specific parameters that were used in this search.

1. Provide input: Data from a network of GW Interferometers, as well as triggers (sub-threshold GRB times and locations) are provided to the pipeline. An input file is also provided which contains various housekeeping and user-defined analysis parameters.

2. Subdivide interferometer data: The time surrounding each trigger time (t_0) is divided into 'on-source' and 'off-source' regions as follows: the on-source begins 600 seconds before t_0, and extends 60 seconds past t_0 to allow for the time delay between GW and GRB emission (see Section 2.6). In the case of the sub-threshold GRB triggers, each trigger time is an interval of duration d (seconds), so that the end of the on-source actually extends to $t_0 + 60 + d$.

$$\text{On-source region: } (t_0 - 600, \, t_0 + 60 + d)$$

The off-source region is chosen to be all of the data within ± 1.5 hours of the on-source region (excluding the on-source segment itself). Off-source data (which are assumed to not contain a GW signal associated with the trigger), are used for background noise estimation. Therefore, it is advantageous to use data that represents, as closely as possible, the state of the detectors at the time that the trigger occurred. The total effective amount of background data is then increased by a factor of approximately 1000 by using artificial time-shifts between the data of different detectors.

On- and off-source regions are divided further into segments of length 256 seconds. The data in each segment are low and high pass filtered (at 506 Hz and 32 Hz, respectively), whitened, and down-sampled to 1024 Hz. Using the location of the trigger, the data are then time-shifted to correct for the different GW arrival time in each detector (see Section 4.3.1). The first and last 4 seconds of each segment are discarded to eliminate filter transients, and segments are overlapped by 8 seconds, to make up for the discarded portions. The inner 248 seconds of each data block remain for clustering and event identification.

3. Construct time-frequency maps and find events: The first step in identifying events in the data is the construction of time-frequency maps. Each block of data identified in the previous step is Fourier transformed to produce time-frequency maps for individual detectors, which are then merged pixel-by-pixel to create time-frequency maps of the detection statistic and desired coherent energies in the data stream for all detectors combined. The FFT integration lengths used (in seconds) are: 1/4, 1/8, 1/16, 1/32, 1/64, 1/128. The following energies and statistics are calculated for all network combinations with the exceptions already noted in Section 4.3.1[9]: *log-likelihood* statistic, *power-law* statistic, E_{circ}, I_{circ}, E_n, I_n, $E_{n,circ}$, $I_{n,circ}$.

In each map, pixels with central frequency less than 64 Hz are discarded due to the poor detector sensitivity at such low frequencies. The 1% of remaining pixels in the current time-frequency map with the highest detection statistic are marked as 'black pixels'. So-called '8-connected' clusters are identified by grouping together black pixels that share either an edge or a vertex with another black pixel. The statistical quantities listed above are then summed over the pixels in each cluster, which allows the clusters to be ranked according to their resulting detection statistics. Only the loudest 62 clusters in each 256 second data block (across all FFT resolutions) are kept for further processing (this amounts to 1 cluster every 4 seconds over the inner 248 second interval). The set of resulting clusters is further pruned by eliminating those that coincide with 'category 2' flags (periods of understood glitchiness in the data which would result in false GW events).

---

[9]H1H2 triggers only use the energies E_+, I_+, E_n, and I_n. In the case of 2 non-aligned detectors (H1L1 for example) E_n and I_n are not available.

4. Tune analysis and calculate upper limits: Once clusters have been identified in the on- and off-source (including time-shifted) segments, events that don't pass certain coherent consistency veto tests are eliminated. To determine the most effective thresholds to use for the coherent vetoes, the analysis must be tuned. For this, a closed-box analysis is done, meaning that only the off-source data segments are used, in order to prevent biasing the results.

The closed-box tuning uses simulated gravitational-wave signals which are injected into the on-source data repeatedly and at different amplitudes to determine the sensitivity of the analysis, that is, how strong a GW signal must be in order to be detected. The process of tuning and estimating upper limits is done separately for each possible GRB trigger. This analysis uses the 8 waveform families which were described in detail in Section 4.3.3.

The actual parameter space $\mathcal{R}$, being tuned includes the following:

- The shape of circular energy cuts being used (r_{circ}, r_{null}, etc.)

- The choice of detection statistic used for event ranking (log-likelihood, or power-law).

The tuning and upper limit estimation procedure is as follows:

  I. Select a GRB and a set of waveform families.

 II. Identify clusters in on- and off-source data as prescribed above.

III. For each separate waveform family, choose 600 waveform injections (by drawing from the parameter distributions described in Section 4.3.3).

IV. Randomly divide the injections and off-source segments into two equal groups to be used for tuning and upper limit estimation.

V. Tune thresholds (using the first group of injections and off-source segments):

1. For each parameter in $\mathcal{R}$, choose a set of trial values (veto thresholds).

2. Apply veto thresholds to the background clusters in the off-source segments and identify the loudest surviving event in each segment, S_{max}. The cumulative distribution of loudest events from each segment is $C(S_{max})$.

3. Choose the off-source segment for which S_{max} is closest to $C(S_{max}) = 0.99$ (the 99th percentile of the off-source S_{max} distribution). This segment is called the *dummy on-source* segment and is used in place of the true on-source segment for the remainder of the tuning process.

4. Read dummy on-source clusters and apply chosen vetoes from step 1. Calculate the 95% efficiency (at 99% confidence level) amplitude upper limit as follows:

   (a) For each h_{rss} amplitude A, inject tuning waveforms (scaled by A) one-by-one into the *true* on-source data and identify clusters as described above. Determine the largest significance S, of all clusters (if any) within a small time window of the injection (± 0.1 s for sine-Gaussians and $(-5, 0.1)$ s for inspirals). Calculate the percentage of injections for which S is at least a big as the most significant cluster in the dummy on-source segment $S \geqslant S_{max}^{dummy-on}$.

   (b) After repeating step (a) for all amplitudes, determine the h_{rss} amplitude for which 95% of the injections have $S \geqslant S_{max}^{dummy-on}$. This is the 95% efficiency, 99% confidence level amplitude upper limit.

5. Repeat steps 1-4 above for each waveform family and for each possible combination of veto thresholds. Choose the combination of thresholds which

minimizes the upper limits (averaged across all waveform families). These are the final tuned veto thresholds.

Note: The tuning is actually done in 2 steps. In the first step, the parameter α from Eqs. 4.27a and 4.27b is set to 1 and steps 1-5 proceed as described above. In the second step, α is set to 0.8, the first set of tuned thresholds $\mathcal{R}_{tuned}$ are applied, and a second set of optimized thresholds is chosen using a 50% detection efficiency instead of 95%. The reason for tuning in 2 steps, is to efficiently reject all loud glitches and as many as possible of the remaining glitches, while maintaining good sensitivity to injections.

VI. Estimate upper limits (using the second group of injections and off-source segments):

The actual estimated upper limits are found by applying the tuned thresholds to the second group of injections and off-source segments that were set aside for this purpose. Tuning steps 2 through 4 above are repeated for all waveform families, using only the tuned thresholds. The upper limits calculated in step 4 are the closed-box estimated upper limits for the current GRB.

VII. Calculate local probability and final upper limits (using the on-source data and tuned thresholds):

Read in the event clusters found in the real on-source data and apply the tuned thresholds. Assign a local probability p to the loudest surviving on-source event based on the background distribution of loudest events in order to determine its significance. A local probabililty less than the 3σ (5σ) tail of a Gaussian distribution is considered evidence for (detection of) a GW. However, this requirement is somewhat arbitrary and follow-up studies must be done on

any low-p trigger before making a GW detection claim. (See Section 5.1 for more details.) In the absence of a GW detection re-calculate the upper limits as described in the steps above, replacing the dummy on-source events with the real on-source events.

CHAPTER V

RESULTS AND INTERPRETATION

In this chapter, the main results are summarized and their significance is quantified. This is done first on a per-GRB basis, by treating each trigger result independently. Next, the overall significance of the combined result from the entire trigger set is determined by calculating the probability of obtaining such a result in the *null hypothesis* case (ie. assuming that no gravitational wave signal is present in the data). A detailed listing of the numerical results for each possible GRB trigger is provided in Appendix C.

Disclaimer: This thesis has not yet been reviewed by the LIGO or Virgo scientific collaborations and therefore the results presented here do not necessarily reflect the opinion of these collborations or the members therein.

5.1. Per-GRB Results

The loudest surviving event for each trigger in the analysis is assigned a *local probability p*, which is based on the distribution of background loudest events found in the off-source time segments surrounding the trigger on-source segment as described in Section 4.3.5. The local probability is defined as the fraction of background trials that resulted in a louder, or more significant event than the loudest surviving on-source event (which has significance $S_{max}^{on-source}$). That is,

$$p \equiv 1 - C(S_{max}^{on-source}),$$
(5.1)

where $C(S_{max})$ is the cumulative distribution of loudest events found in the background trials. Therefore, a very significant event will have a small local probability. Assuming the S_{max} values for each GRB form a Gaussian distribution, the p-value represents the probability that $S_{max}^{on-source}$ lies n standard deviations from the mean; that is, the area beneath the $n\sigma$ tail of the Gaussian curve. Using this interpretation, we would need a 3σ level detection corresponding to a local probability of $p \leq 2.7 \times 10^{-3}$ in order to state that *evidence* of gravitational waves was found. Likewise, a 5σ detection (or $p \leq 5.7 \times 10^{-7}$) is needed for for a statement of GW *detection*. These requirements, although somewhat arbitrary, are commonly used in experimental analyses such as this one.

Only one of the 123 triggers in this analysis meets the 3σ requirement above. The lowest local probability is $p = 0.002$ which is measured for the trigger at GPS time 865807941. Given the number of GRB triggers analyzed, the null hypothesis binomial probability (see Section 5.3) of obtaining one or more with a p-value this small is approximately 22%, which is certainly not small enough for a detection claim. What's more, this particular trigger occurred during a period of elevated non-Gaussian noise in the Virgo detector in the same frequency band as the loudest surviving on-source event (216-280 Hz). The Gaussianity measure of the detector noise during the on-source interval is shown in Figure 5.1. The significantly non-Gaussian behavior of Virgo during this event casts further doubt on its validity as a GW detection.

Because there are only 3 triggers with sky positions overlapping the location of nearby galaxies, it is worth determining whether a significant number of these, if any, occurred for the events in the tail of the local probability distribution (the lowest p-values - see Section 5.3). However, out of the 5% of events (7 total) with the lowest p-values, none of them coincide with a nearby galaxy. The local probability of all
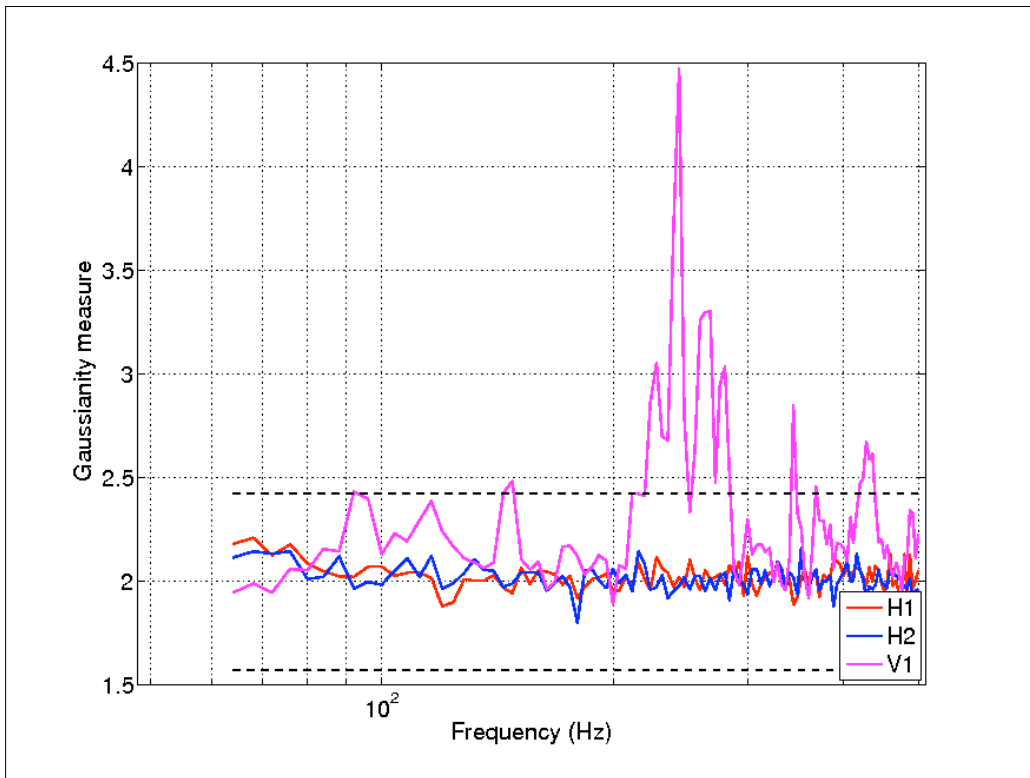
FIGURE 5.1. Gaussianity measure for the on-source interval of the GRB trigger with the lowest calculated local probability. This measure is defined as $\overline{|x(f)|^4}/\overline{|x(f)|^2}^2$, where x is the data. Highly non-Gaussian data extends beyond the 3σ-level bounds shown by the dashed horizontal lines. V1 shows non-Gaussian behavior over the same frequency band as the on-source loudest event, which extended from 216 to 280 Hz.

GPS Time (s)	Local Probability	Network	Swift Trigger Type	Peak SNR	Peak SNR Percentile
865807941	0.0020	H1H2V1	rate	6.2038	0.54
816788077	0.0030	H1H2	image	6.6425	0.60
857550694	0.0045	H1H2	rate	6.1049	0.98
840563576	0.0088	H1H2	rate	6.125	0.89
847552356	0.0155	H1H2	image	6.6518	0.53
862604184	0.0163	H1H2L1	rate	6.1366	0.81
840027606	0.0264	H1H2L1	rate	6.1252	0.88

TABLE 5.1. Trigger data for the 7 lowest p-value events in the tail of the local probability distribution. The significance of the Swift image peak SNR is given in the right-hand column, as the percentage of triggers of the same type (rate or image) with greater or equal SNR_{peak}.

seven events are listed in Table 5.1 along with the IFO network, Swift trigger type (rate or image), and SNR_{peak} of the trigger, as measured by the Swift BAT. The last column is a measure of the significance of SNR_{peak} given as a percentile of the overall distribution of SNR_{peak} values for that trigger type (an above average SNR_{peak} value corresponding to a low percentile). For example, the first trigger in the table is a rate trigger with $\text{SNR}_{peak} = 6.203$, which is less than 54% of the rate trigger peaks in the total sample. The SNR_{peak} values of the Swift image peaks for these triggers are unremarkable compared to the overall SNR_{peak} distribution, with a mean percentile of 0.74. At 53%, the lowest percentile (highest significance) peak is still below the average SNR of the image trigger distribution.

5.2. Distance Exclusion Results

Section 4.3.5 introduced how h_{rss} amplitude upper limits are estimated for each possible GRB trigger. These upper limits can be converted into distance lower limits by examining the relationship between signal amplitude and source distance r. For

inspiral waveforms, the conversion is simple because amplitude and distance are inversely related through Eqs. 2.4 and 4.37. In the case of sine-Gaussian waveforms h_{rss} amplitude is converted to a distance approximation through the GW energy relation for an on-axis observer (Eq. 1.46) which we recall here:

$$h^2_{rss} = \int (h^2_+ + h^2_\times)dt \simeq \frac{1}{\omega^2_{GW}}\frac{10G}{r^2c^3}E_{GW},\qquad(5.2)$$

where E_{GW} is the total energy emitted in gravitational waves by the source. The distance limits shown here use a value of $E_{GW} = 10^{-2}\,M_\odot c^2$ where $M_\odot$ is the mass of the sun. This is the value of E_{GW} that is commonly used for computing distance limits. However, realistic estimates for the total GW energy emitted by bar-mode instabilities in core-collapse supernovae are substantially less (by a factor of 10), with large associated uncertainties [49]. To obtain the results for any other energy (say E'_{GW}), one can simply multiply the distance limit by the factor $\sqrt{E'_{GW}/10^{-2}\,M_\odot c^2}$. Generally speaking, however, the observer does not lie directly on the rotational axis of the system, and the h_{rss} energy relation instead takes the following form: [20], [50]

$$h^2_{rss} =\simeq \frac{\alpha}{\omega^2_{GW}}\frac{G}{r^2c^3}E_{GW},\qquad(5.3)$$

where the value α is of order 1, and depends on the viewing angle and specific geometry of the system [18].

In the general case setting $\alpha = 1$, we see that compared to the ideal rotating quadrupole of Eq. 5.2, the exclusion distance results are smaller (by a factor of $\sqrt{10}$). Realistically, due to the coincident γ-ray observation and the beamed nature of GRBs, the line of sight is close to the rotational axis, so the true relationship between r and h_{rss} is somewhere between Eqs. 5.2 and 5.3.

Waveform Family Description	Median 90% Amplitude UL $(\mathrm{Hz}^{-1/2})$	Median 90% Distance LL (Mpc)
NSBHI $m(1.4, 10)$ $r(20)$ $i(0, 30)$	5.66×10^{-22}	16.12
NSNSI $m(1.4, 1.4)$ $r(10)$ $i(0, 30)$	4.82×10^{-22}	6.70
NSBHII $m(1.4, 10)$ $r(20)$ $i(0, 90)$	1.53×10^{-21}	5.96
NSNSII $m(1.4, 1.4)$ $r(10)$ $i(0, 90)$	1.30×10^{-21}	2.49
SGI $f_0(150)$ $i(0, 5)$	4.57×10^{-22}	15.82
SGII $f_0(300)$ $i(0, 5)$	6.06×10^{-22}	5.97
SGIII $f_0(150)$ $i(0, 90)$	1.16×10^{-21}	6.24
SGIV $f_0(300)$ $i(0, 90)$	1.67×10^{-21}	2.17

TABLE 5.2. Mean 90% confidence level amplitude upper limits and corresponding exclusion distances for each injected waveform family.

The distance lower limit that is calculated for each GRB trigger and waveform family combination represents the distance from which 90% of injected waveforms are recovered with a significance greater than or equal to the loudest surviving cluster in the on-source data segment. In the absence of a GW detection, the distance limits reflect the sensitivity of the search (with higher limits corresponding to greater sensitivity).

The exclusion distances computed for the inspiral and sine-Gaussian (using Eq. 5.2) waveform families are plotted in Figures 5.2 and 5.3, respectively (and given numerically in Table C.1 of Appendix C). As expected, the search is most sensitive to waveforms with small inclination angles (nearly circular polarization). The median exclusion distances and amplitude upper limits for each waveform family are displayed in Table 5.2.

5.3. Binomial Test Results

Because of the large number of trials used in this analysis, finding a few GRBs with very low p-values is not necessarily inconsistent with the null hypothesis. Even
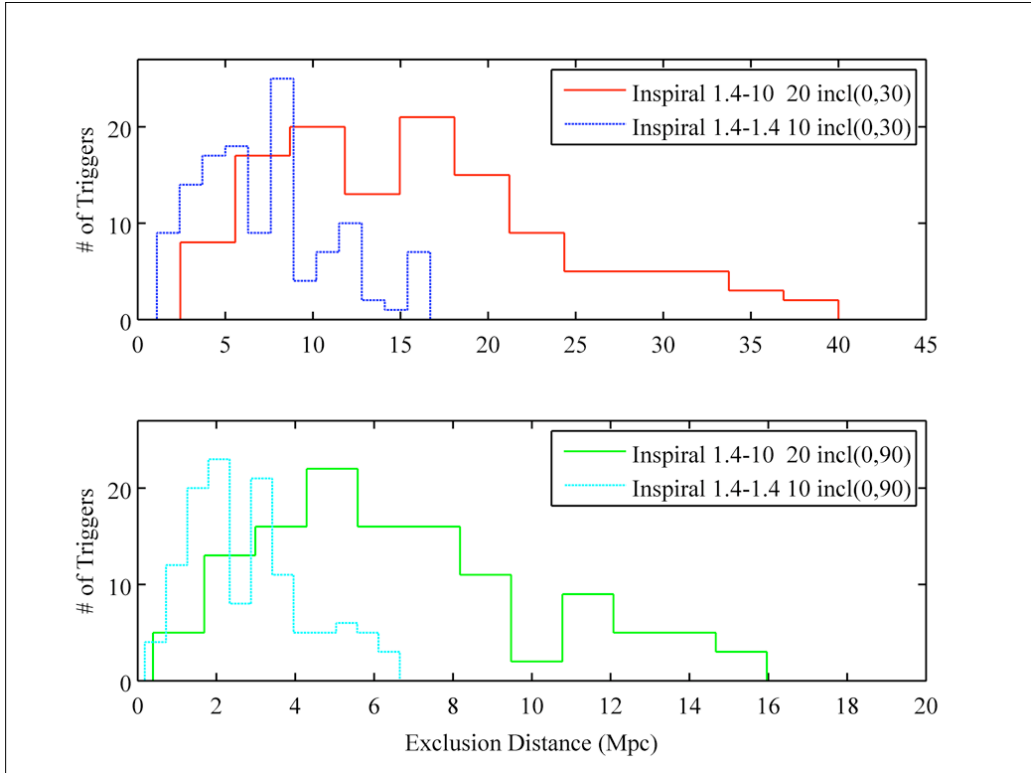
FIGURE 5.2. Histogram of 90% confidence level exclusion distances for inspiral waveform families. The top panel shows NSBH (nominal $r = 20\,\mathrm{Mpc}$) and NSNS (nominal $r = 10\,\mathrm{Mpc}$) waveforms with inclination jittering between 0° and 30°. The bottom panel shows the same waveforms with a larger inclination spread (between 0° and 90°).
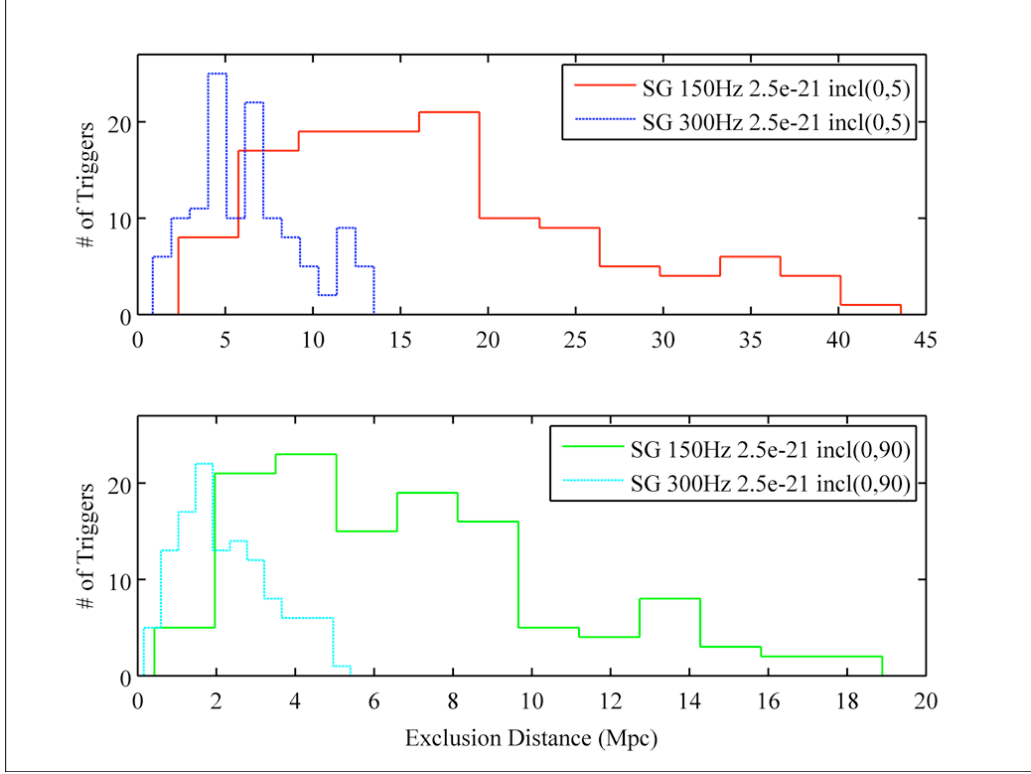
FIGURE 5.3. Histogram of 90% confidence level exclusion distances for sine-Gaussian waveform families assuming $E_{GW} = 10^{-2} M_\odot c^2$ (distance limits for any other energy E'_{GW} can be obtained by multiplying the given limits by the factor $\sqrt{E'_{GW}/10^{-2}M_\odot c^2}$). The top panel shows $f_0 = 150\,\mathrm{Hz}$ and $f_0 = 300\,\mathrm{Hz}$ SG waveforms (nominal amplitude $A_0 = 2.5 \times 10^{-21}$) with inclination jittering between $0°$ and $5°$. The bottom panel shows the same waveforms with a larger inclination spread (between $0°$ and $90°$).

with no gravitational wave present in the data, a very significant background event may be detected in the on-source window a small percentage of the time. Under the null hypothesis, the p-values of the 123 triggers should form a flat distribution on the interval [0,1]. The binomial test takes into account the trial factor of the analysis, and determines the significance of the deviation of the measured local probability distribution from the null hypothesis [50]. This deviation can be from either one very loud event, or a collection of moderately loud events, which might indicate a group of weak detections.

For an experiment that is repeated N times with a per-trial probability of success p, the binomial probability of measuring exactly k successes is given by

$$P_k(p) = \binom{N}{k} p^k (1-p)^{N-k},$$

(5.4)

where

$$\binom{N}{k} = \frac{N!}{k!(N-k)!}.$$

(5.5)

In this analysis, $N = 123$ and the p-values of all 123 triggers in ascending order are $p_1, p_2, p_3, \cdots p_N$. Then for each p_k, the probability of getting k *or more* p-values less than p_k is

$$P_{\geq k}(p_k) = \sum_{r \geq k} \binom{N}{r} p_k^r (1-p_k)^{N-r}$$

(5.6a)

$$= 1 - \sum_{r < k} \binom{N}{r} p_k^r (1-p_k)^{N-r}.$$

(5.6b)

The binomial probability is calculated for the smallest 5% of the p-values (p_1 through p_7). The largest deviation from the null hypothesis is taken to be the

100

minimum $P_{\geq k}(p_k)$ for $k = 1 \cdots 7$. That is

$$P_{binomial} = \min_{1 \leq k \leq N_{tail}} P_{\geq k}(p_k), \qquad (5.7)$$

where $N_{tail} = 0.05 \cdot N = 7$.

The cumulative distribution of p-values is shown in Figure 5.4 along with the distribution one expects from the null hypothesis. The largest deviation from the null hypothesis occurs at $k = 6$ ($p_6 = 0.0163$), corresponding to a binomial probability of $P_{binomial} = 0.0159$. This means that the probability of having 6 or more events with local probability $p \leq 0.0163$ is 1.59%.

This result, however, does not take into account the trial factors introduced by testing all 7 events in N_{tail}. To account for these additional trial factors and determine the true significance of the result a Monte Carlo simulation is used. 123 fake p-values are randomly drawn from a flat distribution between 0 and 1, and the smallest binomial probability is again calculated using the 7 events in the tail of the fake distribution. This simulation is repeated 100,000 times with different fake p-value distributions. The fraction of Monte Carlo trials that result in binomial probabilities as small or smaller than $P_{binomial} = 0.0159$ is 0.096 (or approximately 10%). In other words, the analysis would produce results at least this significant 10% of the time under the null hypothesis. Therefore, this result is found to be consistent with the null hypothesis that there is no gravitational wave present in the signal.
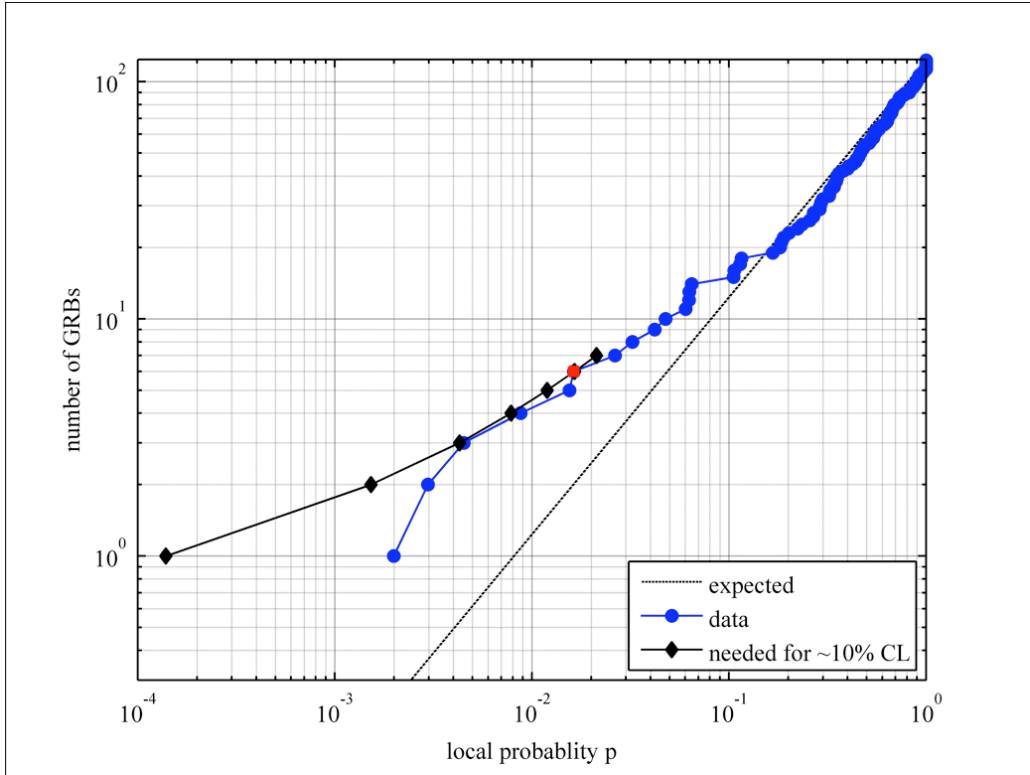
FIGURE 5.4.   Binomial test: the cumulative distribution of local probabilities calculated for each of the 123 possible GRB triggers. The maximum deviation from the null hypothesis (depicted by the diagonal dashed line), occurs for the 6 smallest p-values in the tail of the distribution. The binomial probability of having 6 or more events with a local probability $p \leq p_6 = 0.0163$, is 1.59%. 10% of Monte Carlo trials obtain a result this significant. The black solid line shows the maximum local probability needed by each trigger for a 10% confidence level (C.L.) in the null hypotheses. The red data point which marks the largest deviation from the null hypothesis at p_6 just touches the 10% C.L. curve.

CHAPTER VI

SUMMARY AND DISCUSSION

This thesis presented results of a LIGO-Virgo gravitational wave search using 123 below-threshold potential GRB triggers detected by the Swift Burst Alert Telescope. Due to the low SNR of the GRB detections and the lack of follow-up observations, the validity of the triggers has never been assessed. However, based on above-threshold detection rates and SNR distriubtions, approximately 10% of the below-threshold trigger sample is estimated to be from real GRB events. Interferometer data was analyzed for each trigger time and location using the coherent network analysis code X-Pipeline, which is more sensitive by a factor of ~ 2 than cross-correlation analyses previously used in GRB-triggered GW searches [44].

No gravitational wave signal was detected for any of the individual GRB triggers. The most significant local probability found was $p = 0.002$. However, given the number of triggers used, the probability of obtaining at least one result this significant in the null hypothesis is 22%. The binomial test was used on the 7 triggers in the smallest 5% of the p-value distribution (the tail) to determine the collective significance of a handful of weak detections. The largest deviation from the null hypothesis occurs for the 6 events with the lowest p-values. Given the additional trial factor of testing all 7 events in the tail, the binomial probability of this result is approximately 10%, which is consistent with the null hypothesis. In the absence of a GW detection, 90% confidence level distance lower limit estimates were calculated for each of the waveform families used in the analysis. The median lower limits are approximately 16 Mpc for both the 1.4-10$M_\odot \sim$NSBH$\sim i(0°$-30°) and the 150Hz$\sim$SG$\sim i(0°$-5°) waveforms families.

We can compare these results to those obtained by the primary GRB-GW burst search which used 137 confirmed (above threshold) GRB triggers during the same science run (S5/VSR1)[20]. The primary search also did not find a sufficiently significant excess in the tail of the local probability distribution to claim GW detection. And the median 90% exclusion distance for the 150 Hz sine-Gaussian waveforms was 12 Mpc[1].

The low-threshold GRB results are not surprising given that the most optimistic estimate for rates of Swift-observable GRBs with detectable GW counterparts in range of the LIGO-Virgo detectors is on the order of one per millenium (see Section 2.7). However, Advanced LIGO-Virgo, the new generation of interferometers scheduled to come online in 2015, will be 10 times more sensitive than S5/VSR1 which increases the total observation volume by a factor of 10^3 [51]. In addition, new GRB-detecting satellites such as Fermi - with its 9 sr FOV - will also be able to cover larger areas of the sky, leading to a much higher rate of observable GRBs. Projected rates of LL-GRBs during the advanced phase of LIGO-Virgo are as high as ~ 2.8 yr^{-1}. In that case, an analysis such as this one is of paramount importance, since the cost of missing a GRB that is buried beneath the detection threshold could truly mean a missed opportunity for gravitational wave detection.

---

[1]Unfortunately, we cannot compare that result to the low-threshold GRB result *directly*, because updates have since been made to the analysis code. In addition, the primary search uses the distance energy relation given in Eq. 2.6. Correcting for this difference gives $D = \sqrt{5/2}D_0 = 18$ Mpc, where $D_0 = 12$ Mpc is the quoted median distance LL.

TRIGGER TABLES

TABLE A.1. The final list of BAT image trigger peaks selected for the GW analysis (ordered by SNR_{peak}).

GPS Start Time (s)	Interval Dur. (s)	RA (deg)	DEC (deg)	SNR_{peak} (σ)	IFO Network
858177484.170	64.000	140.380	−3.842	6.990	H1H2L1
844577068.501	64.000	126.524	−38.302	6.970	H1L1
862466068.064	64.000	8.245	−27.756	6.939	H1H2L1
854403276.263	64.000	50.291	23.953	6.904	H1H2
846544204.454	120.000	138.440	−36.534	6.880	H1H2L1
859065868.148	64.000	39.933	31.468	6.864	H1H2
874302531.764	64.000	103.039	50.918	6.848	H1H2L1V1
852907292.299	64.000	185.408	−25.854	6.845	H1H2L1
826509228.926	64.000	28.383	45.371	6.840	H1H2L1
850389924.361	64.000	116.042	33.508	6.803	H1H2L1
865317027.992	64.000	154.516	69.876	6.801	H1H2L1V1
874549587.757	64.000	22.479	−45.938	6.783	H1H2L1V1
833212212.771	64.000	234.811	5.807	6.755	H1H2
862033540.074	64.000	22.936	−74.358	6.753	H1H2
841408244.577	96.000	217.741	27.741	6.715	H1H2
849328468.386	64.000	303.335	16.961	6.706	H1H2
830351932.838	120.000	103.598	−40.716	6.704	H1H2

Continued on next page

GPS Start Time (s)	Interval Dur. (s)	RA (deg)	DEC (deg)	SNR$_{peak}$ (σ)	IFO Network
873468299.785	64.000	41.322	-71.114	6.699	H1H2V1
860580388.111	64.000	311.733	50.204	6.668	H1H2L1
842098828.560	64.000	32.161	-57.364	6.662	H1H2L1
860116364.122	64.000	203.710	23.790	6.654	H1H2L1
850389844.361	80.000	157.580	35.254	6.652	H1H2L1
847552356.429	64.000	308.716	-27.269	6.652	H1H2
817689293.124	64.000	211.097	25.601	6.648	H1H2
851057372.344	64.000	189.372	-8.763	6.644	H1H2L1
816788077.144	64.000	291.490	57.422	6.643	H1H2
851953868.323	64.000	202.304	-29.154	6.641	H1H2L1
870223963.868	64.000	22.918	-49.584	6.641	H1H2L1
865151435.996	64.000	114.656	-31.099	6.639	H1H2V1
856082012.222	64.000	56.615	1.783	6.637	H1H2L1
853856716.276	64.000	216.618	27.142	6.635	H1H2L1
874576283.757	64.000	226.184	-50.062	6.635	H1H2L1V1
862636892.059	64.000	208.276	-67.476	6.630	H1H2
853223932.292	64.000	55.998	9.244	6.620	H1H2L1
833844948.756	72.000	354.980	-16.805	6.616	H1H2
818406557.109	64.000	184.919	20.626	6.613	H1H2L1
852176148.317	64.000	33.631	-6.445	6.611	H1H2L1
835976828.706	64.000	189.612	-6.981	6.610	H1H2L1

GPS Start Time (s)	Interval Dur. (s)	RA (deg)	DEC (deg)	SNR$_{peak}$ (σ)	IFO Network
821858869.032	80.000	72.243	−1.438	6.610	H1H2
856234004.218	64.000	113.950	34.009	6.607	H1L1
874824715.750	64.000	247.593	3.066	6.602	H1H2L1
841912820.565	64.000	248.986	33.871	6.602	H1H2L1
816444029.151	64.000	93.854	−11.402	6.602	H2L1

TABLE A.2. The final list of BAT rate trigger image peaks selected for the GW analysis (ordered by SNR$_{peak}$).

GPS Start Time (s)	Interval Dur. (s)	RA (deg)	DEC (deg)	SNR$_{peak}$ (σ)	IFO Network
848418081.528	2.048	165.442	−32.361	6.863	H1H2
836273494.107	0.512	239.273	59.063	6.553	H1H2L1
853585913.339	16.384	235.827	51.896	6.471	H1H2
827871479.775	4.096	288.611	−35.554	6.468	H1H2
843115976.568	8.192	256.188	12.456	6.443	H1H2L1
819407708.271	0.032	150.284	−50.763	6.429	H1H2L1
842062199.829	0.004	246.399	37.649	6.424	H1H2
842297485.708	0.128	139.792	−69.920	6.420	H1H2L1
820185622.797	16.384	342.494	−32.610	6.417	H1H2
831557048.377	0.032	162.233	29.863	6.416	H1H2

GPS Start Time (s)	Interval Dur. (s)	RA (deg)	DEC (deg)	SNR$_{peak}$ (σ)	IFO Network
850648764.994	12.160	236.336	51.927	6.406	H1H2
853216748.064	0.032	38.297	−45.227	6.406	H1H2L1
861782384.561	0.256	279.119	32.002	6.406	H1H2L1
837519190.653	26.880	62.134	−62.087	6.401	H1H2L1
867288774.119	16.384	344.506	73.754	6.396	H1L1V1
844175313.759	0.032	262.264	57.479	6.378	H1H2L1
863430876.167	1.024	285.310	−52.881	6.374	H1H2L1
832389447.798	1.024	139.330	10.353	6.373	H1H2L1
851774057.383	0.512	253.373	−4.009	6.365	H1H2
857958733.587	0.032	250.000	45.274	6.335	H1H2L1
843666389.223	0.032	262.755	6.875	6.332	H1H2
864963955.105	2.048	323.613	9.692	6.331	L1V1
815824247.933	0.032	173.111	−62.178	6.298	H1H2
855010885.560	0.032	300.634	79.857	6.296	H1H2L1
858740863.452	0.032	330.353	−69.547	6.295	H1H2L1
846526620.838	0.032	138.244	−66.224	6.283	H1H2
823070283.917	8.192	270.947	10.002	6.274	H1H2
833372166.303	16.384	148.262	−25.724	6.268	H1H2L1
841498341.471	8.192	61.905	5.440	6.267	H1H2
843267762.676	26.880	347.521	12.192	6.267	H1H2
841116961.160	0.032	78.509	−25.939	6.265	H1H2

Table A.2 – *Continued from previous page*

GPS Start Time (s)	Interval Dur. (s)	RA (deg)	DEC (deg)	SNR$_{peak}$ (σ)	IFO Network
839466268.815	16.384	269.432	-69.157	6.246	H1H2L1
829989795.886	0.256	248.602	-17.432	6.245	H1H2L1
857037909.606	8.192	85.073	49.852	6.239	H1H2L1
821079740.497	0.032	281.871	63.366	6.235	H1H2L1
861589474.493	0.032	204.284	31.886	6.234	H1H2L1
839508155.726	0.512	322.778	50.245	6.227	H1H2
858426396.592	0.032	125.423	19.796	6.226	H1H2L1
852063930.720	0.032	231.852	-16.844	6.224	H1H2
849747438.720	0.032	127.954	55.225	6.222	H1H2
831857240.834	26.880	215.965	56.523	6.208	H1H2
831317033.871	0.032	80.199	10.156	6.207	H1H2
865807941.772	2.048	331.092	25.314	6.204	H1H2V1
861619987.573	0.256	321.778	45.714	6.198	H1H2
843006677.947	2.048	302.519	22.946	6.190	H1H2L1
833328678.304	2.048	264.933	-23.215	6.189	H1H2L1
866348894.334	26.880	12.417	-58.148	6.182	H1H2L1V1
842059076.377	0.032	30.406	-25.984	6.180	H1H2
846507013.159	2.048	309.124	35.892	6.179	H1H2L1
824493786.413	0.064	261.955	35.592	6.178	H1H2
838499784.934	1.024	179.141	-12.543	6.177	H1H2
833784414.805	2.048	250.152	-65.848	6.168	H1H2L1

Continued on next page

GPS Start Time (s)	Interval Dur. (s)	RA (deg)	DEC (deg)	SNR$_{peak}$ (σ)	IFO Network
833932139.094	0.032	10.618	−1.775	6.165	H1H2L1
847969536.979	0.032	339.574	−3.623	6.155	H1H2L1
820765571.488	0.032	160.515	55.899	6.152	H1H2
838985780.059	2.048	252.276	36.584	6.150	H1H2L1
843354482.418	16.384	321.294	0.025	6.144	H1H2
827659765.572	0.064	276.479	27.011	6.143	H1H2L1
831604317.640	4.096	197.273	−50.582	6.142	H1H2L1
854342827.176	1.024	239.408	−49.627	6.141	H1H2L1
843236536.181	8.192	228.385	−10.432	6.140	H1H2
830474146.647	0.032	163.918	51.455	6.140	H1H2
821279599.929	0.032	60.291	−8.648	6.138	H1H2
867256915.368	0.032	14.970	28.594	6.138	H1H2L1
862604184.412	4.096	355.771	1.368	6.137	H1H2L1
846153122.415	0.064	270.261	5.284	6.134	H1H2L1
817809804.626	0.032	227.046	15.960	6.133	H1H2L1
863784633.599	16.384	211.324	−62.060	6.130	H1H2L1V1
857647220.887	26.880	333.772	45.964	6.130	H1L1
840027606.018	1.024	337.019	32.254	6.125	H1H2L1
840563576.949	2.048	283.600	69.051	6.125	H1H2
862308146.595	2.048	233.638	40.863	6.120	H1H2L1
824848909.540	1.024	41.501	−55.432	6.119	H1L1

Table A.2 – *Continued from previous page*

GPS Start Time (s)	Interval Dur. (s)	RA (deg)	DEC (deg)	SNR_{peak} (σ)	IFO Network
838955625.051	1.024	308.049	60.618	6.119	H1H2L1
863923625.019	2.048	298.015	66.934	6.117	H1H2L1V1
849276413.668	16.384	314.743	-23.746	6.115	H1H2
868322023.693	1.024	220.998	35.937	6.114	H1H2V1
857550694.490	26.880	102.772	-26.016	6.105	H1H2
833479016.505	0.032	265.489	-30.799	6.103	H1H2L1
852058475.708	0.032	237.342	21.068	6.100	H1H2

APPENDIX B

GALAXY CATALOG STUDY

The sizes and sky positions of the $\sim$53,000 galaxies within a distance of 100 Mpc are obtained from the Gravitational Wave Galaxy Catalog [41]. The location of each galaxy center is plotted in Figure B.1.

A simulated trigger sample is constructed by drawing random RA and DEC values from a uniform sky distribution. That is, the RA values form a flat distribution on the interval $(0°, 360°)$ (shown in Figure B.2), and the $\cos(DEC - 90°)$ values form a flat distribution on the interval $(-1, 1)$ (shown in Figure B.3).

Each of the 100,000 simulated trigger locations is compared with each of the GWGC galaxies. A match is declared if the angular distance between trigger and galaxy is less than $3 + (b + \text{ERR}_b)/2$ arcmin, where b, and ERR_b are the major axis and major axis error, respectively. If a trigger has more than one galaxy match, only the closest one is counted.

In total, 2009 of the 100,000 random trigger locations overlap with a nearby galaxy. Therefore, the estimate of the nearby galaxy effective sky coverage (given triggers with 3-arcmin error radii) is $2.0 \pm 0.1\%$.
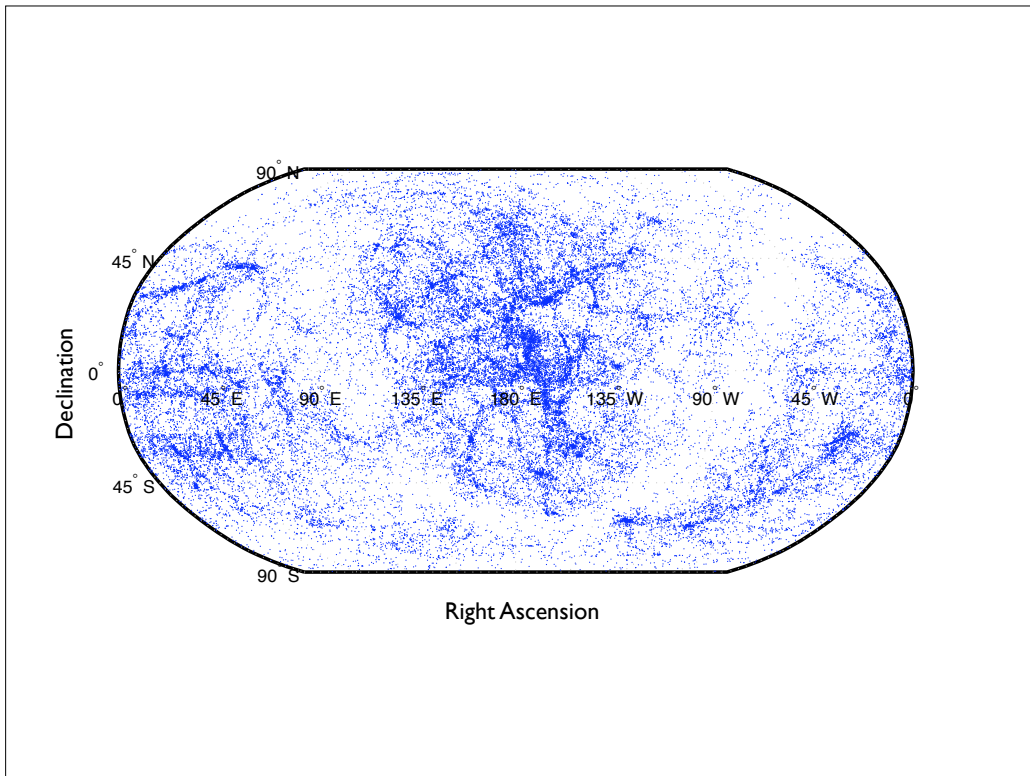
FIGURE B.1. The sky position of each galaxy center from the GWGC catalog (galaxies within 100 Mpc), plotted as a point (marker size in the figure is not indicative of galaxy sky coverage).
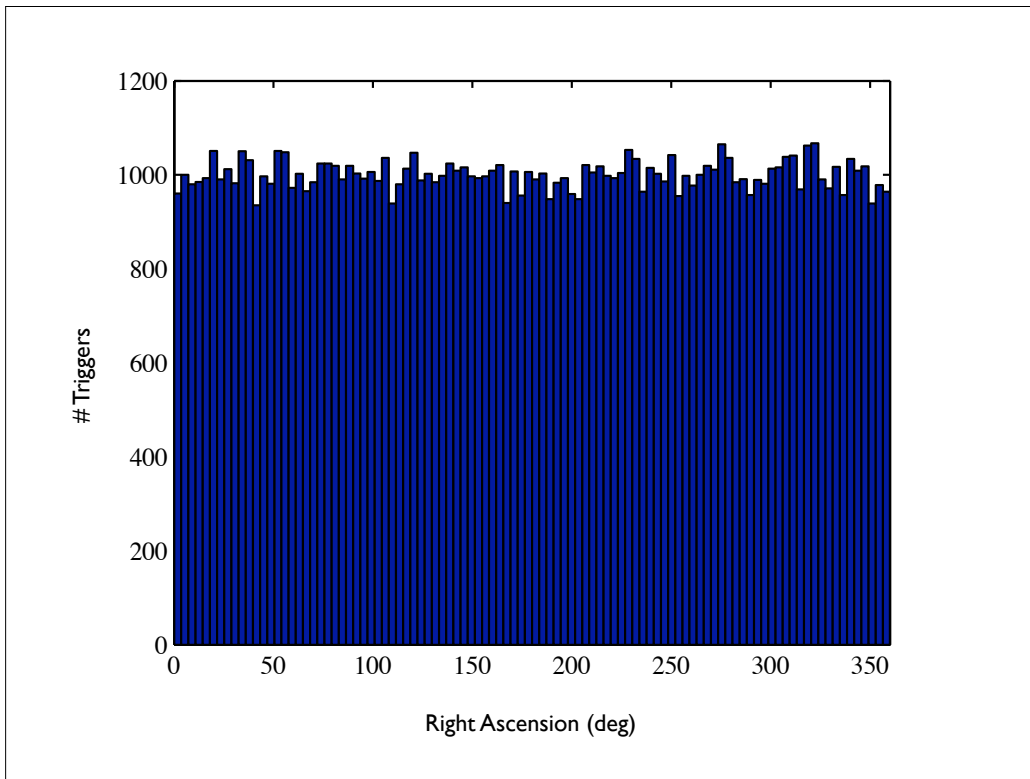
FIGURE B.2. Right ascension distribution of the 100,000 simulated triggers.
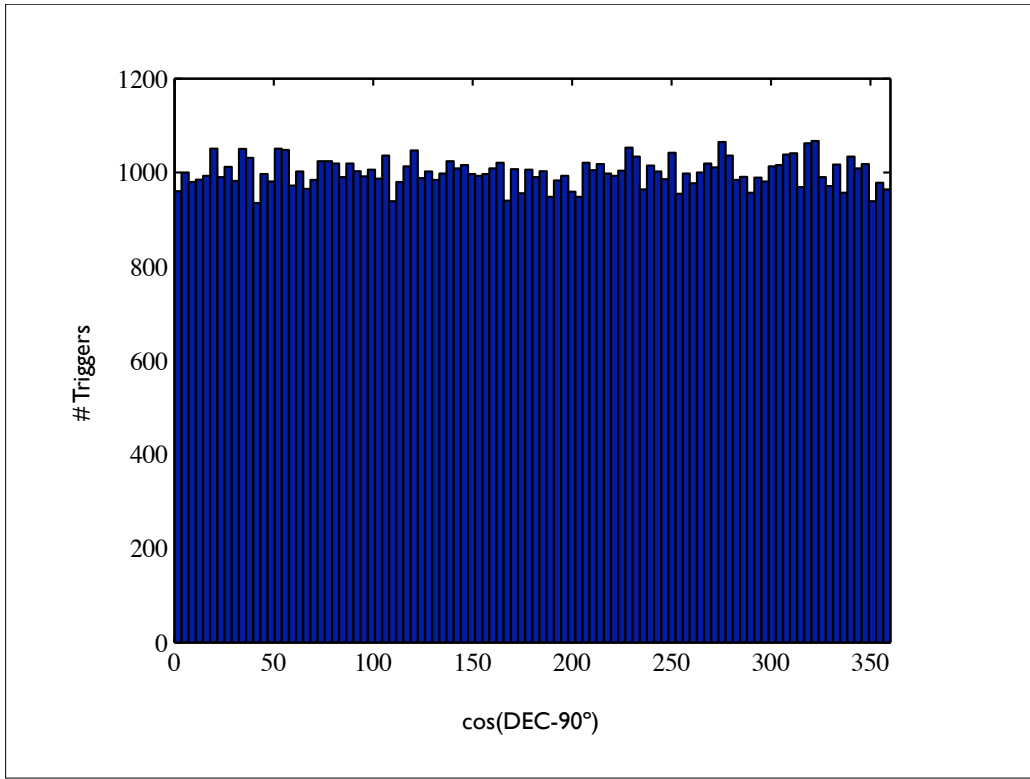
FIGURE B.3. Declination distribution of the 100,000 simulated triggers. Even sky coverage requires a flat distribution of the function $\cos(DEC - 90°)$.

DETAILED ANALYSIS RESULTS

The numerical results of the X-Pipeline analysis are displayed in Table C.1 for each individual trigger event. Data in the columns are formatted as follows: The GPS time of each trigger is given in seconds and is the truncated start time of the Swift imaging interval used in detecting the image peak. The UTC date and time are given in 'YYMMDD' and 'hh:mm:ss' formats. The antenna factors for each interferometer are given by

$$F = \sqrt{F_p^2 + F_c^2}, \tag{C.1}$$

where F_p and F_c are the plus and cross antenna factors, respectively. An entry of '-' indicates that the particular interferometer was not taking good science quality data at the time of the trigger, and was not used in the analysis.

The analysis window is the start and stop time of the on-source window for that GRB trigger given as an offset (in seconds) from the trigger start time. p is the local probability of the loudest surviving on-source event, and 'Num Trials' is the number of trials used in estimating the background distribution of local probabilities.

Finally, the 90% exclusion distances are given in Mpc for each waveform family. As an example, the 'NSBH (30,90)' column contains two entries corresponding to the exclusion distances for the NSBH waveforms (inspirals using mass parameters 1.4 and 10 $M_\odot$) with inclination jittering on the intervals $(0°, 30°)$ and $(0°, 90°)$, respectively.

Emelie Harstad

TABLE C.1. Detailed per-GRB X-Pipeline analysis results

GPS Time (s)	UTC Time Date	UTC Time Time	Antenna Response H1	H2	L1	V1	Analysis Window (s)	p	Num Trials	90% Exclusion Distances (Mpc) NSBH (30, 90)	NSNS (30, 90)	SG150 (5, 90)	SG300 (5, 90)
816788077	052311	13:34:24	0.33	0.33	-	-	-600,124	0.00	3030	(5, 2)	(2, 1)	(4, 2)	(2, 1)
817689293	050312	23:54:40	0.32	0.32	-	-	-600,124	0.78	555	(5, 2)	(2, 1)	(5, 2)	(2, 1)
821858869	062101	06:07:35	0.65	0.65	-	-	-600,140	0.69	3620	(10, 4)	(5, 2)	(10, 5)	(4, 2)
830351932	062904	13:18:38	0.98	0.98	-	-	-600,180	0.90	2222	(19, 8)	(8, 3)	(19, 9)	(7, 3)
833212212	060106	15:49:58	0.51	0.51	-	-	-600,124	0.45	2564	(10, 5)	(5, 2)	(10, 4)	(4, 2)
833844948	060806	23:35:34	0.69	0.69	-	-	-600,132	0.72	1396	(12, 6)	(6, 3)	(13, 6)	(5, 2)
841408244	060409	12:30:30	0.26	0.26	-	-	-600,156	0.54	2213	(6, 2)	(3, 1)	(7, 3)	(2, 1)
847552356	061411	15:12:22	0.86	0.86	-	-	-600,124	0.02	2191	(16, 6)	(7, 3)	(16, 6)	(6, 2)
849328468	060512	04:34:14	0.36	0.36	-	-	-600,124	0.44	2906	(8, 3)	(4, 1)	(8, 4)	(3, 1)
854403276	070102	22:14:22	0.56	0.56	-	-	-600,124	0.72	3404	(13, 6)	(6, 2)	(13, 6)	(5, 2)
859065868	072703	21:24:14	0.95	0.95	-	-	-600,124	0.76	2744	(17, 7)	(8, 3)	(18, 8)	(8, 3)
862033540	070105	05:45:26	0.87	0.87	-	-	-600,124	0.34	3088	(18, 8)	(8, 3)	(19, 8)	(7, 3)
862636892	070805	05:21:18	0.50	0.50	-	-	-600,124	0.51	3929	(10, 4)	(5, 2)	(9, 4)	(4, 2)
816444029	051911	14:00:16	-	0.53	0.50	-	-600,124	0.88	454	(8, 3)	(3, 1)	(10, 3)	(3, 1)
818406557	051212	07:09:04	0.50	0.50	0.52	-	-600,124	1.00	2078	(12, 3)	(6, 1)	(13, 4)	(5, 1)
826509228	061603	01:53:34	0.81	0.81	0.48	-	-600,124	0.30	2772	(18, 8)	(9, 3)	(20, 8)	(6, 3)
835976828	060307	15:46:54	0.73	0.73	0.64	-	-600,124	0.32	2080	(22, 8)	(9, 3)	(25, 9)	(8, 3)
841912820	061009	08:40:06	0.45	0.45	0.46	-	-600,124	0.64	2394	(17, 5)	(7, 2)	(17, 5)	(5, 1)
842098828	061209	12:20:14	0.27	0.27	0.14	-	-600,124	0.92	2853	(7, 3)	(3, 1)	(7, 3)	(2, 1)
844577068	061110	04:44:14	0.95	-	0.74	-	-600,124	0.90	1367	(27, 12)	(12, 5)	(34, 13)	(12, 4)
846544204	060211	23:09:50	0.79	0.79	0.95	-	-600,180	1.00	838	(20, 9)	(9, 4)	(21, 8)	(7, 2)
850389844	061712	11:23:50	0.94	0.94	0.99	-	-600,140	0.44	3601	(32, 14)	(15, 6)	(35, 14)	(12, 4)
850389924	061712	11:25:10	0.94	0.94	0.76	-	-600,124	0.96	3552	(31, 13)	(13, 5)	(30, 13)	(12, 5)
851057372	062512	04:49:18	0.72	0.72	0.58	-	-600,124	1.00	2964	(16, 5)	(7, 2)	(16, 6)	(6, 2)
851953868	070401	13:50:54	0.38	0.38	0.50	-	-600,124	0.74	2496	(13, 5)	(6, 2)	(14, 6)	(5, 2)
852176148	070701	03:35:34	0.60	0.60	0.68	-	-600,124	0.64	3596	(19, 8)	(9, 3)	(21, 7)	(7, 2)
852907292	071501	14:41:18	0.35	0.35	0.40	-	-600,124	0.67	2654	(12, 3)	(5, 1)	(13, 4)	(4, 1)
853223932	071901	06:38:38	0.70	0.70	0.53	-	-600,124	0.67	3368	(19, 7)	(8, 3)	(18, 8)	(7, 3)
853856716	072601	14:25:02	0.94	0.94	0.88	-	-600,124	0.29	2751	(29, 11)	(12, 6)	(29, 12)	(12, 4)
856082012	072102	08:33:18	0.11	0.11	0.54	-	-600,124	0.29	3055	(6, 3)	(3, 1)	(7, 3)	(2, 1)
856234004	072302	02:46:30	0.84	-	0.98	-	-600,124	0.11	3687	(30, 13)	(12, 5)	(34, 14)	(11, 5)
858177484	071703	14:37:50	0.57	0.57	0.85	-	-600,124	0.59	2992	(24, 9)	(11, 4)	(24, 9)	(9, 3)
860116364	070904	01:12:30	0.49	0.49	0.55	-	-600,124	0.17	3638	(18, 5)	(8, 3)	(20, 8)	(7, 2)

Table C.1 – *Continued from previous page*

GPS Time (s)	UTC Time Date	UTC Time Time	Antenna Response H1	H2	L1	V1	Analysis Window (s)	p	Num Trials	90% Exclusion Distances (Mpc) NSBH (30, 90)	NSNS (30, 90)	SG150 (5, 90)	SG300 (5, 90)
860580388	071404	10:06:14	0.70	0.70	0.75	-	[-600,124]	0.46	2124	(26, 10)	(11, 4)	(26, 12)	(9, 3)
862466068	070605	05:54:14	0.95	0.95	0.89	-	[-600,124]	0.96	1704	(37, 15)	(17, 7)	(39, 16)	(13, 5)
865151435	070606	07:50:21	0.80	0.80	-	0.58	[-600,124]	0.05	3315	(16, 6)	(6, 3)	(16, 6)	(7, 3)
865317027	070806	05:50:13	0.80	0.80	0.59	0.56	[-600,124]	0.71	2044	(26, 11)	(12, 5)	(28, 10)	(10, 4)
870223963	070408	00:52:29	1.00	1.00	0.88	-	[-600,124]	0.87	3780	(35, 15)	(16, 6)	(37, 18)	(13, 5)
873468299	071009	14:04:45	0.51	0.51	-	0.89	[-600,124]	0.90	3647	(12, 5)	(6, 2)	(12, 4)	(5, 2)
874302531	072009	05:48:37	0.35	0.35	0.27	0.99	[-600,124]	1.00	2231	(12, 5)	(5, 2)	(13, 5)	(5, 1)
874549587	072309	02:26:13	0.68	0.68	0.37	0.50	[-600,124]	0.98	2065	(20, 8)	(9, 4)	(18, 7)	(7, 3)
874576283	072309	09:51:09	0.98	0.98	0.94	0.41	[-600,124]	0.36	2456	(40, 15)	(17, 7)	(44, 19)	(12, 4)
874824715	072609	06:51:41	0.07	0.07	0.50	-	[-600,124]	0.52	3436	(5, 2)	(2, 1)	(5, 2)	(2, 1)
821079740	061201	05:42:06	0.47	0.47	0.40	-	[-600,60]	0.19	2042	(10, 5)	(4, 2)	(9, 4)	(4, 2)
829989795	062504	08:43:01	0.55	0.55	0.70	-	[-600,60]	0.33	2699	(21, 9)	(9, 3)	(23, 9)	(8, 3)
833328678	060306	00:11:04	0.73	0.73	0.43	-	[-600,62]	0.82	3315	(20, 9)	(9, 4)	(21, 9)	(7, 3)
833372166	060306	12:15:52	0.92	0.92	0.97	-	[-600,76]	0.85	2397	(35, 16)	(16, 6)	(38, 16)	(13, 5)
833784414	060806	06:46:40	0.44	0.44	0.35	-	[-600,62]	0.64	3196	(15, 6)	(6, 2)	(15, 7)	(5, 2)
833932139	060906	23:48:45	0.45	0.45	0.78	-	[-600,60]	0.43	2018	(20, 9)	(9, 3)	(24, 9)	(9, 3)
839466268	061308	01:04:14	0.61	0.61	0.50	-	[-600,76]	0.53	2805	(20, 9)	(9, 3)	(22, 8)	(7, 3)
843006677	062309	00:31:03	0.65	0.65	0.91	-	[-600,62]	0.48	3174	(24, 12)	(11, 5)	(26, 11)	(9, 3)
846507013	060211	12:49:59	0.36	0.36	0.45	-	[-600,62]	1.00	2708	(11, 4)	(5, 2)	(13, 5)	(5, 2)
857037909	070403	10:04:55	0.58	0.58	0.47	-	[-600,68]	0.29	3381	(18, 6)	(8, 3)	(18, 6)	(7, 2)
858426396	072003	11:46:22	0.28	0.28	0.47	-	[-600,60]	0.92	3266	(8, 1)	(4, 0)	(10, 3)	(4, 1)
861589474	072604	02:24:20	0.59	0.59	0.79	-	[-600,60]	0.73	3185	(23, 7)	(11, 3)	(24, 8)	(9, 3)
865807941	071306	22:12:07	0.52	0.52	-	0.34	[-600,62]	0.00	1506	(11, 4)	(4, 2)	(11, 4)	(4, 1)
866348894	072006	04:28:00	0.96	0.96	0.75	0.30	[-600,87]	0.06	1897	(28, 13)	(13, 5)	(32, 12)	(12, 4)
815824247	051211	09:50:34	0.72	0.72	-	-	[-600,60]	0.12	2725	(10, 4)	(4, 2)	(10, 5)	(4, 1)
820185622	060101	21:20:08	0.50	0.50	-	-	[-600,77]	0.55	3868	(7, 3)	(3, 1)	(7, 3)	(3, 1)
820765571	060801	14:25:57	0.89	0.89	-	-	[-600,60]	0.84	3903	(13, 6)	(6, 2)	(13, 6)	(5, 2)
821279599	061401	13:13:05	0.58	0.58	-	-	[-600,60]	0.65	3549	(10, 5)	(5, 2)	(10, 4)	(4, 2)
823070283	060402	06:37:49	0.54	0.54	-	-	[-600,69]	0.68	3441	(8, 3)	(4, 2)	(8, 4)	(3, 2)
824493786	062002	18:02:52	0.87	0.87	-	-	[-600,60]	0.58	1169	(17, 7)	(8, 3)	(18, 7)	(6, 3)
827871479	063103	20:17:45	0.56	0.56	-	-	[-600,64]	0.63	2391	(12, 5)	(5, 2)	(11, 5)	(4, 2)
830474146	063004	23:15:32	0.72	0.72	-	-	[-600,60]	1.00	3271	(12, 5)	(6, 2)	(11, 5)	(4, 2)
831317033	061005	17:23:39	0.34	0.34	-	-	[-600,60]	0.86	2270	(7, 3)	(3, 1)	(7, 3)	(3, 1)
831557048	061305	12:03:54	0.49	0.49	-	-	[-600,60]	0.11	2377	(10, 5)	(4, 2)	(9, 5)	(4, 2)

Table C.1 – *Continued from previous page*

GPS Time (s)	UTC Time Date	Time	Antenna Response H1	H2	L1	V1	Analysis Window (s)	p	Num Trials	90% Exclusion Distances (Mpc) NSBH (30, 90)	NSNS (30, 90)	SG150 (5, 90)	SG300 (5, 90)
831857240	061605	23:27:06	0.56	0.56	-	-	-600,86	0.03	2997	(12, 5)	(5, 2)	(12, 5)	(5, 2)
838499784	060108	20:36:10	0.55	0.55	-	-	-600,61	0.22	2694	(6, 3)	(2, 1)	(8, 3)	(3, 1)
839508155	061308	12:42:21	0.74	0.74	-	-	-600,60	0.73	3096	(16, 8)	(7, 3)	(16, 6)	(6, 2)
840563576	062508	17:52:42	0.44	0.44	-	-	-600,62	0.01	3191	(8, 3)	(4, 1)	(9, 3)	(3, 1)
841116961	060109	03:35:47	0.92	0.92	-	-	-600,60	0.56	3444	(19, 8)	(8, 3)	(18, 8)	(7, 3)
841498341	060509	13:32:07	0.75	0.75	-	-	-600,69	0.34	3752	(16, 7)	(7, 3)	(16, 7)	(6, 2)
842059076	061209	01:17:42	0.82	0.82	-	-	-600,60	0.65	2196	(16, 8)	(7, 3)	(15, 7)	(6, 3)
842062199	061209	02:09:45	0.97	0.97	-	-	-600,60	0.20	3005	(18, 8)	(8, 3)	(18, 9)	(8, 3)
843236536	062509	16:22:02	0.29	0.29	-	-	-600,68	0.83	3257	(7, 3)	(3, 1)	(7, 3)	(2, 1)
843267762	062609	01:02:28	0.31	0.31	-	-	-600,87	0.54	2966	(8, 3)	(3, 1)	(7, 3)	(3, 1)
843354482	062709	01:07:48	0.40	0.40	-	-	-600,77	0.82	3585	(9, 4)	(4, 2)	(9, 4)	(4, 2)
843666389	063009	15:46:15	0.58	0.58	-	-	-600,60	0.46	2765	(14, 6)	(6, 2)	(14, 5)	(6, 2)
846526620	060211	18:16:46	0.54	0.54	-	-	-600,60	0.54	2424	(11, 5)	(5, 2)	(11, 5)	(4, 2)
848418081	062411	15:41:07	0.18	0.18	-	-	-600,62	0.61	1778	(4, 1)	(2, 1)	(3, 1)	(1, 0)
849276413	060412	14:06:39	0.86	0.86	-	-	-600,76	0.27	2990	(17, 8)	(8, 3)	(17, 7)	(7, 3)
849747438	061012	00:57:04	0.25	0.25	-	-	-600,60	0.35	2785	(5, 2)	(2, 1)	(5, 2)	(2, 1)
850648764	062012	11:19:10	0.62	0.62	-	-	-600,72	0.78	2742	(10, 5)	(5, 2)	(11, 5)	(5, 2)
851774057	070201	11:54:03	0.19	0.19	-	-	-600,60	0.32	3328	(3, 1)	(2, 1)	(3, 1)	(1, 1)
852058475	070501	18:54:21	0.83	0.83	-	-	-600,60	1.00	1831	(12, 4)	(6, 2)	(13, 6)	(5, 2)
852063930	070501	20:25:16	0.51	0.51	-	-	-600,60	0.04	1048	(8, 3)	(3, 1)	(8, 3)	(3, 1)
853585913	072301	11:11:39	0.77	0.77	-	-	-600,76	1.00	3808	(12, 5)	(6, 2)	(12, 5)	(5, 2)
857550694	071003	08:31:20	0.50	0.50	-	-	-600,87	0.00	2660	(10, 4)	(4, 2)	(9, 4)	(4, 2)
861619987	072604	10:52:53	0.75	0.75	-	-	-600,60	0.40	2638	(19, 8)	(8, 3)	(20, 9)	(8, 3)
817809804	050512	09:23:11	0.52	0.52	0.50	-	-600,60	1.00	3596	(11, 2)	(5, 1)	(12, 3)	(4, 1)
819407708	052312	21:14:55	0.90	0.90	0.93	-	-600,60	0.91	1153	(24, 11)	(11, 4)	(26, 10)	(9, 4)
824848909	062402	20:41:35	0.57	-	0.50	-	-600,61	0.64	924	(14, 6)	(6, 2)	(17, 7)	(6, 2)
827659765	062903	09:29:11	0.58	0.58	0.83	-	-600,60	0.35	3523	(18, 8)	(8, 3)	(19, 8)	(7, 3)
831604317	061405	01:11:43	0.58	0.58	0.49	-	-600,64	0.67	3448	(21, 8)	(9, 3)	(23, 9)	(7, 3)
832389447	062305	03:17:13	0.76	0.76	0.64	-	-600,61	0.69	3877	(24, 10)	(11, 4)	(26, 11)	(9, 3)
833479016	060406	17:56:42	0.79	0.79	0.97	-	-600,60	0.89	3320	(34, 14)	(16, 6)	(37, 15)	(13, 5)
836273494	060707	02:11:20	0.89	0.89	0.87	-	-600,60	0.27	3614	(24, 11)	(12, 5)	(30, 13)	(11, 4)
837519190	062107	12:12:56	0.61	0.61	0.50	-	-600,87	0.06	1443	(18, 7)	(8, 3)	(19, 8)	(7, 2)
838955625	060708	03:13:31	0.79	0.79	0.78	-	-600,61	0.40	3315	(27, 12)	(12, 5)	(32, 14)	(10, 4)
838985780	060708	11:36:06	0.48	0.48	0.51	-	-600,62	0.11	3386	(17, 6)	(8, 2)	(18, 8)	(6, 2)

119

Table C.1 – *Continued from previous page*

GPS Time (s)	UTC Time Date	UTC Time Time	Antenna Response H1	Antenna Response H2	Antenna Response L1	Antenna Response V1	Analysis Window (s)	p	Num Trials	90% Exclusion Distances (Mpc) NSBH $(30, 90)$	90% Exclusion Distances (Mpc) NSNS $(30, 90)$	90% Exclusion Distances (Mpc) SG150 $(5, 90)$	90% Exclusion Distances (Mpc) SG300 $(5, 90)$
840027606	061908	12:59:52	0.64	0.64	0.24	-	-600,61]	0.03	1854	$(16, 7)$	$(7, 3)$	$(17, 7)$	$(6, 2)$
842297485	061409	19:31:11	0.47	0.47	0.34	-	-600,60]	0.23	2304	$(13, 6)$	$(6, 2)$	$(13, 5)$	$(4, 1)$
843115976	062409	06:52:42	0.18	0.18	0.28	-	-600,68]	0.93	2445	$(7, 3)$	$(3, 1)$	$(7, 3)$	$(2, 1)$
844175313	060610	13:08:19	0.26	0.26	0.15	-	-600,60]	0.06	2908	$(8, 3)$	$(3, 1)$	$(9, 3)$	$(3, 1)$
846153122	062910	10:31:48	0.65	0.65	0.79	-	-600,61]	1.00	3503	$(20, 8)$	$(9, 4)$	$(20, 9)$	$(7, 2)$
847969536	061911	11:05:22	0.47	0.47	0.80	-	-600,60]	1.00	3251	$(16, 7)$	$(8, 3)$	$(15, 7)$	$(6, 2)$
853216748	071901	04:38:54	0.20	0.20	0.16	-	-600,60]	0.38	3363	$(5, 2)$	$(2, 1)$	$(6, 2)$	$(2, 1)$
854342827	070102	05:26:53	0.93	0.93	0.67	-	-600,61]	0.48	2915	$(29, 12)$	$(12, 5)$	$(28, 13)$	$(12, 5)$
855010885	070802	23:01:11	0.78	0.78	0.62	-	-600,60]	0.99	1812	$(25, 12)$	$(12, 4)$	$(26, 11)$	$(10, 4)$
857647220	071103	11:20:06	0.51	-	0.49	-	-600,87]	0.58	2834	$(17, 7)$	$(8, 2)$	$(19, 7)$	$(6, 2)$
857958733	071503	01:51:59	0.06	0.06	0.12	-	-600,60]	0.18	3317	$(2, 0)$	$(1, 0)$	$(2, 0)$	$(1, 0)$
858740863	072403	03:07:29	0.86	0.86	0.78	-	-600,60]	0.92	2852	$(32, 14)$	$(15, 5)$	$(35, 15)$	$(12, 4)$
861782384	072804	07:59:30	0.65	0.65	0.87	-	-600,60]	0.49	2539	$(31, 11)$	$(13, 5)$	$(34, 13)$	$(12, 4)$
862308146	070405	10:02:12	0.97	0.97	0.78	-	-600,62]	0.97	1951	$(34, 14)$	$(16, 6)$	$(38, 16)$	$(13, 4)$
862604184	070705	20:16:10	0.59	0.59	0.46	-	-600,64]	0.02	1593	$(17, 4)$	$(8, 2)$	$(18, 6)$	$(6, 1)$
863430876	071705	09:54:22	0.40	0.40	0.38	-	-600,61]	0.91	2357	$(16, 7)$	$(7, 3)$	$(16, 7)$	$(6, 2)$
863784633	072105	12:10:19	0.68	0.68	0.64	0.88	-600,76]	0.68	1772	$(23, 9)$	$(11, 4)$	$(24, 9)$	$(9, 1)$
863923625	072305	02:46:51	0.48	0.48	0.36	0.92	-600,63]	0.06	652	$(14, 4)$	$(6, 2)$	$(15, 2)$	$(5, 1)$
864963955	070406	03:45:41	-	-	0.52	0.83	-600,62]	0.26	3726	$(8, 3)$	$(4, 1)$	$(9, 3)$	$(4, 2)$
867256915	073006	16:41:41	0.87	0.87	0.62	-	-600,60]	0.35	2617	$(29, 11)$	$(12, 4)$	$(29, 13)$	$(10, 4)$
867288774	070107	01:32:40	0.51	-	0.39	0.84	-600,76]	0.18	1291	$(15, 4)$	$(6, 2)$	$(14, 3)$	$(5, 1)$
868322023	071307	00:33:29	0.83	0.83	-	0.59	-600,61]	0.47	3449	$(18, 9)$	$(8, 3)$	$(19, 8)$	$(8, 3)$

REFERENCES CITED

[1] A. Einstein, Annalen der Physik **354**, 769 (1916).

[2] S. M. Carroll, *Spacetime and Geometry: An Introduction to General Relativity* (Addison Wesley, 2004).

[3] J. H. Taylor, L. A. Fowler, and P. M. McCulloch, Nature **277**, 437 (1979).

[4] M. Maggiore, *Gravitational Waves Volume 1: Theory and Experiments* (Oxford University Press, 2008).

[5] N. Gehrels and P. Mészáros, Science **337**, 932 (2012).

[6] P. Mészáros, Reports on Progress in Physics **69**, 2259 (2006).

[7] W. S. Paciesas et al., Astrophys. J. Suppl. Ser. **122**, 465 (1999).

[8] J. Heise, in *Joint European and National Astronomical Meeting*, edited by J. D. Hadjidemetrioy and J. H. Seiradakis (1997).

[9] P. Mészáros and N. Gehrels, Research in Astronomy and Astrophysics **12**, 1139 (2012).

[10] G. Vedrenne and J. L. Atteia, *Gamma-Ray Bursts* (Springer, 2009).

[11] P. Mészáros, Science **291**, 79 (2001).

[12] J. L. Racusin, E. W. Liang, D. N. Burrows, A. Falcone, T. Sakamoto, B. B. Zhang, B. Zhang, P. Evans, and J. Osborne, Astrophys. J. **698**, 43 (2009).

[13] I. Leonor, P. Sutton, R. Frey, G. Jones, S. Marka, and Z. Marka, Class.Quant.Grav. **26**, 204017 (2009).

[14] H. Beltrami and W. Y. Chau, Astrophysics and Space Science **111**, 335 (1985).

[15] P. C. Peters and J. Mathews, Physical Review **131**, 435 (1963).

[16] C. D. Ott, H. Dimmelmeier, A. Marek, H.-T. Janka, I. Hawke, B. Zink, and E. Schnetter, Phys. Rev. Lett. **98**, 261101 (2007).

[17] C. D. Ott, E. Abdikamalov, E. O'Connor, C. Reisswig, R. Haas, P. Kalmus, S. Drasco, A. Burrows, and E. Schnetter, Phys. Rev. D. **86**, 024026 (2012).

[18] M. Was, Ph.D. thesis, UNIVERSITÉ PARIS-SUD (2011).

[19] C. B. Markwardt, S. D. Barthelmy, J. C. Cummings, D. Hullinger, H. A. Krimm, and A. Parsons, *The SWIFT BAT Software Guide*, NASA/GSFC, Greenbelt, MD, v. 6.3 ed. (2007).

[20] B. P. Abbott et al., Astrophys. J. **715**, 1438 (2010).

[21] D. B. Fox et al., Nature **437**, 845 (2005).

[22] E. Rossi, D. Lazzati, and M. J. Rees, Mon. Not. R. Astron. Soc. **332**, 945 (2002).

[23] J. Granot, A. Panaitescu, P. Kumar, and S. E. Woosley, Astrophys. J. Lett. **570**, L61 (2002).

[24] R. Chapman, N. R. Tanvir, R. S. Priddey, and A. J. Levan, Mon. Not. R. Astron. Soc. **382**, L21 (2007).

[25] F. J. Virgili, E.-W. Liang, and B. Zhang, Mon. Not. R. Astron. Soc. **392**, 91 (2009).

[26] P. R. Saulson, *Fundamentals of Interferometric Gravitational Wave Detectors* (World Scientific, 1994).

[27] B. P. Abbott et al., Reports on Progress in Physics **72**, 076901 (2009).

[28] S. A. Hughes, S. Marka, P. L. Bender, and C. J. Hogan (Snowmass, 2001).

[29] N. Gehrels, in *Gamma-Ray Bursts: 30 Years of Discovery*, edited by E. Fenimore and M. Galassi (2004), vol. 727 of *American Institute of Physics Conference Series*, pp. 637–641.

[30] *Goddard space flight center: About the swift gamma-ray burst mission*, Website (Accessed: March 2013), URL `http://swift.gsfc.nasa.gov/docs/swift/about_swift/`.

[31] *Swift fact sheet: Catching gamma-ray bursts on the fly*, GSFC/NASA Web Publication, http://heasarc.nasa.gov/docs/swift/about_swift/Sci_Fact_Sheet.pdf (2004).

[32] S. D. Barthelmy et al., Space Science Reviews **120**, 143 (2005).

[33] G. K. Skinner, Appl. Opt. **47**, 2739 (2008).

[34] D. L. Band, Astrophys. J. **644**, 378 (2006).

[35] *The gamma-ray coordinates network*, Website (Accessed: March 2013), URL `http://gcn.gsfc.nasa.gov/`.

[36] *Swift data archive*, File Transfer Protocol Server (Accessed: March 2013), URL `ftp://legacy.gsfc.nasa.gov/`.

[37] *Nasa's heasarc: Software*, Website (Accessed: March 2013), URL
http://heasarc.gsfc.nasa.gov/docs/software.html.

[38] D. Palmer, *Private communication*, LANL (palmer@lanl.gov).

[39] *Goddard space flight center bat digest*, Website (Accessed: March 2013), URL
http://heasarc.gsfc.nasa.gov/docs/swift/analysis/bat_digest.html.

[40] T. Sakamoto et al., Astrophys. J. Suppl. Ser. **195**, 2 (2011).

[41] D. J. White, E. J. Daw, and V. S. Dhillon, Classical and Quantum Gravity **28**, 085016 (2011).

[42] J. Abadie et al., Astrophys. J. **755**, 2 (2012).

[43] J. Abadie et al., Astrophys. J. **760**, 12 (2012).

[44] P. J. Sutton et al., New Journal of Physics **12**, 053034 (2010).

[45] S. Chatterji, A. Lazzarini, L. Stein, P. J. Sutton, A. Searle, and M. Tinto, Phys. Rev. D. **74**, 082005 (2006).

[46] A. C. Searle, P. J. Sutton, M. Tinto, and G. Woan, Classical and Quantum Gravity **25**, 114038 (2008).

[47] S. W. Hawking and W. Israel, *300 Years of Gravitation* (Cambridge University Press, 1989).

[48] L. Blanchet, B. R. Iyer, C. M. Will, and A. G. Wiseman, Classical and Quantum Gravity **13**, 575 (1996).

[49] J. L. Houser, J. M. Centrella, and S. C. Smith, Physical Review Letters **72**, 1314 (1994).

[50] B. Abbott et al., Phys. Rev. D. **77**, 062004 (2008).

[51] S. J. Waldman, ArXiv e-prints (2011), 1103.2728.